Use of whiskers as model systems for studying surface barriers in type II superconductors

James, M. S.

Award date:
2000

Awarding institution:
University of Bath

Use of Whiskers as Model Systems for Studying Surface Barriers in Type II Superconductors

Submitted by M. S. James
For the degree of PhD
of the University of Bath
2000

ProQuest LLC
789 East Eisenhower Parkway
P.O. Box 1346
Ann Arbor, MI 48106-1346

Abstract

A range of micron-sized Hall probe arrays has been used to investigate the Bean-Livingston surface barrier in single crystal whiskers of the type II superconductor $Bi_2Sr_2CaCu_2O_{8+\delta}$. It is shown that the magnetic properties of the whiskers are dominated by surface barriers, and hysteresis loops exhibit behaviour entirely consistent with such a system, showing very small magnetisation on the return leg. Measurements of the temperature dependence of the field of first flux penetration indicate that above approximately 5mT the vortex lines decouple into stacks of two-dimensional vortex pancakes, which surmount the surface barrier through thermal activation, in agreement with recent models of giant flux creep over surface barriers. Once inside the whisker, the vortices collect in the centre to produce a dome-shaped magnetic flux profile, which is observed experimentally. Careful measurements of the initial leg of the hysteresis loop show a sawtooth structure, which is interpreted as evidence of a hierarchy of stable vortex states. Field-cooled measurements exhibit a sharp drop in the local magnetic induction, which is interpreted as a boundary between a regime dominated by surface barriers and a regime dominated by the inter-vortex repulsion. Transport measurements have also been carried out, and the results support the idea that the transport properties of the whiskers are strongly affected by surface barriers.

Acknowledgements

I would like to thank my supervisor, Dr. Simon Bending, for giving me the opportunity to carry out this research. Without his guidance and seemingly infinite patience, I would not have been able to complete this work.

I am also must grateful to the following people: Dr. M Henini from Nottingham University for providing many of the 2DEG heterostructures used to make the Hall probes, Dr. C. Binns from Leicester University for depositing the Fe clusters described in Appendix 1 and Dr. M. Konczykowski for irradiating the whiskers described in Chapter 11.

In addition to these people, I would like to thank Wendy Lambson for keeping the clean room facilities in working order, Bob Draper for all his advice on practical matters, and the University glass blower, Mike Lock, for repairing a broken nitrogen dewar.

Finally I would like to thank all the other members of the group, past and present, who have helped me through the more difficult times, particularly Siva, Gary and Sasha.

Contents

Chapter 1

Thesis Overview

1.1 Introduction

Ever since superconductivity was first discovered by Kamerlingh-Onnes in 1911 [H.K. Onnes, 1911], there has been great excitement at the potential for materials which truly have zero dc electrical resistance. The first applications were in high-field magnets, since it was thought that large currents could be used to produce large fields without the cooling problems caused by Joule heating in conventional solenoids. However, it was soon discovered that the superconducting state could be destroyed by modest magnetic fields, greatly restricting the maximum current that could be applied to a superconductor without driving it normal.

With the discovery of type II superconductivity, it was found that magnetic flux could partially penetrate the superconductor in quantized units of flux, without destroying the superconducting state. This meant that larger magnetic fields could be sustained than in type I superconductors, and this had lead to the development of high-field superconducting magnets, which can generate magnetic fields typically of the order of 10^7 Am^{-1} at liquid helium temperatures.

In developing high field magnets, the experimental maximum current densities that could be achieved without loss were found to be significantly less than values predicted from calculations of H_{c2}, and the large discrepancy can often be explained in terms of motion of flux vortices. In type II superconductors, modest magnetic fields can penetrate the superconductor in quantized units of flux, known as vortices, which are able to move around within the superconductor. If a transport current is applied, a

Lorentz acts on the vortices, causing them to move, which requires energy and leads to dissipation. To try and minimise these losses, it was clear that the vortices had to be "pinned" in one position, in a similar way that domain walls can be pinned in ferromagnetic materials. This is achieved by introducing pinning centres such as defects, non-superconducting inclusions, grain boundaries, or material impurities.

1.2 Structure of Thesis

The study of bulk pinning centres has been the subject of much research, and has lead to greatly increased values of critical current density. In much of the work, however, the effect of surfaces has been ignored, usually under the very reasonable justification that most pinning effects are dominated by bulk pinning, rather than any surface effects. Although this justification is true for many real bulk systems, there are also cases where surfaces may play an important role, particularly thin films and clean single crystals, which may have very large surface-to-volume ratios, and it is the aim of this thesis to study the effects of surface pinning on vortex motion. This has been achieved by fabricating micron-sized Hall probe arrays to study the local vortex distribution in single crystal whiskers of the type II superconductor $Bi_2Sr_2CaCu_2O_{8+\delta}$. Whiskers have the advantage that they have a very large surface-to-volume ratio, and electron microscopy studies [Kraak *et al.*, 1996] have shown that they can be free of extended defects, making them ideal model systems for investigating the effects of surface pinning.

In chapter 2, the fundamental properties of superconductivity are introduced, and the phenomenological London theory is used to explain these properties. The concept of a coherence length is introduced through the Ginzburg-Landau theory, and flux pinning is described through the Bean model of the critical state.

In chapter 3, the more unusual properties of high temperature superconductors are discussed, and the two major surface interactions – the Bean-Livingston barrier and the geometrical barrier – are introduced and described in detail. Chapter 4 describes the properties of the particular high temperature superconductor $Bi_2Sr_2CaCu_2O_{8+\delta}$, studied in this work, and chapter 5 describes the fabrication and characterisation of whiskers of $Bi_2Sr_2CaCu_2O_{8+\delta}$ carried out at Bath.

The experimental arrangement, including a description of the Hall effect and the fabrication procedures used to make the Hall probes is given in Chapter 6, and the rest of the thesis is concerned with the results. Chapter 7 deals with vortex entry into the whisker via thermal activation, and chapter 8 describes what happens to the vortices once they have entered the superconductor. Chapter 9 describes the results of transport measurements, in terms of a model proposed by Benkraouda and Clem [1998] and Chapter 10 presents some preliminary work on the effects of irradiation on the surface barrier.

In Chapter 11 the work is reviewed and suggestions for further work are made.

Chapter 2

Introduction to Superconductivity

2.1 History and Discovery

In 1908, H. Kamerlingh-Onnes succeeded in liquefying Helium at his laboratory in Leiden, opening up a range of experimental temperatures extending to below 4.2K. Three years later, whilst investigating the temperature dependence of the resistivity of a sample of mercury, he found that instead of approaching a minimum value at very low temperatures, the resistance abruptly dropped to an immeasurably small value below a temperature of 4.2K [H. K. Onnes, 1911]. This experiment marked the discovery of superconductivity and opened up a whole new branch of physics.

2.2 Properties of Ideal Superconductors

As Kamerlingh-Onnes discovered, a superconducting material can lose all traces of electrical resistivity when cooled below its transition temperature T_C. However, this only occurs in certain materials and only at low current densities. The transition to the superconducting state is very sensitive to magnetic fields, with large fields (greater than a temperature dependent critical field $\vec{H}_C(T)$) destroying superconductivity altogether.

If a superconductor is cooled through its transition temperature in the presence of a small magnetic field (smaller than $\vec{H}_C(T)$), the flux density is

completely expelled, giving superconductors the added property of being perfectly diamagnetic below $\vec{H}_C(T)$. This remarkable property, shown schematically in Figure 2.1, is achieved by inducing screening currents which flow around the perimeter of the superconductor and produce a magnetic flux density which exactly cancels that produced by the external applied field. This effect was discovered by Meissner and Oschenfeld and is hence known as the Meissner effect [W. Meissner and R. Ochsenfeld, 1933].

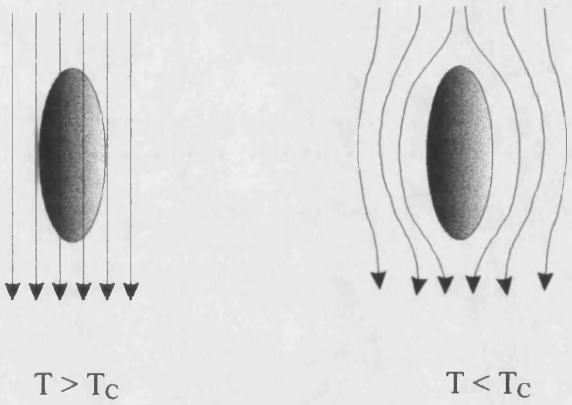

Figure 2.1. The Meissner Effect.

It is important to note that the Meissner effect is not simply a direct consequence of zero resistivity, but is a distinct property of superconductors which makes them different from a material with infinite conductivity (a perfect conductor). Indeed, the Meissner effect is often used as a defining property of superconductors, as well as the property of infinite electrical conductivity.

Further research showed that superconductors are divided into two categories. In type I materials, flux density is completely expelled by the screening currents, up to a temperature dependent critical field, $\vec{H}_C(T)$. In type II superconductors, the H-T phase diagram is separated into three regimes. In the regime where the applied field is less than a lower critical field $\vec{H}_{C1}(T)$, the flux density is completely expelled, as in type I superconductors. If the applied field is increased beyond $\vec{H}_{C1}(T)$, magnetic flux begins to penetrate along discrete lines, where the superconductor is normal. These

lines of magnetic flux are surrounded by circulating supercurrents and are known as vortices (or fluxons), and the region of the H-T phase space where they exist is known as the mixed state (or Shubnikov state). As the applied field is increased still further, the number of vortices increases until, at the upper critical field $\vec{H}_{C2}(T)$ the normal cores begin to overlap and the superconductor becomes completely normal. The phase diagrams for the two types of superconductors are shown in Figure 2.2 below.

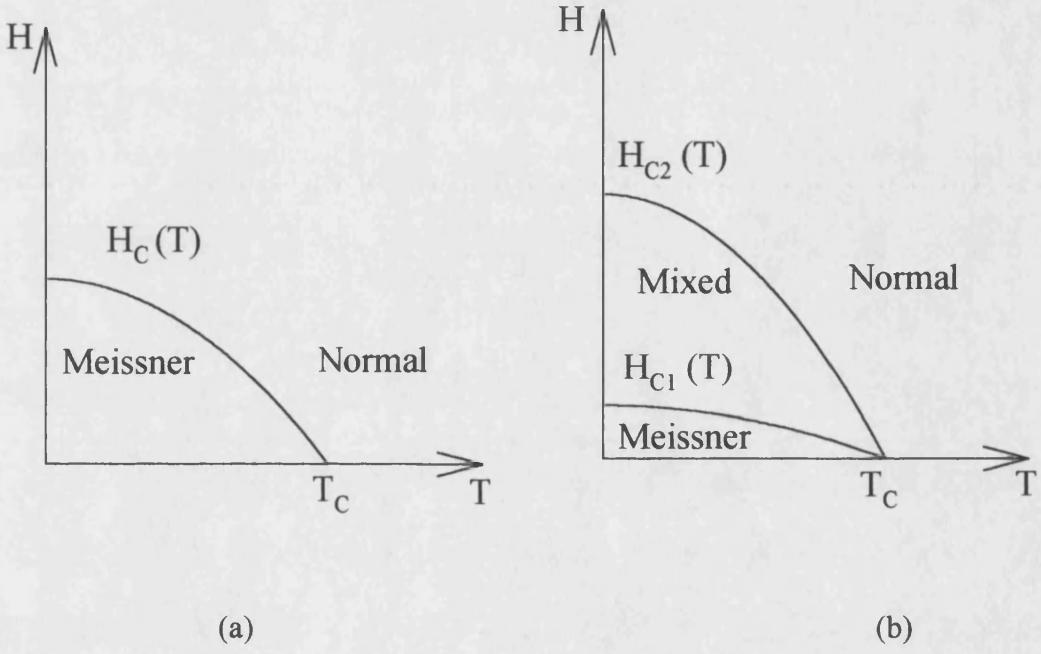

Figure 2.2. Phase diagrams for (a) type I and (b) type II superconductors.

Magnetisation curves for ideal (i.e. no pinning effects) type I and II superconductors are shown in Figure 2.3 below. For type I superconductors, the flux density is completely expelled by screening currents up to the critical field $\vec{H}_C$, at which point the superconductor becomes normal. Since $\vec{B} = 0$ in the Meissner state, the slope of the magnetisation curve, which is equal to the susceptibility of the material, has the value –1: the definition of perfect diamagnetism. In type II superconductors, the Meissner state still has the same slope of –1, but between $\vec{H}_{C1}$

and $\vec{H}_{C2}$ the number of vortices inside the superconductor increases, increasing the flux density and decreasing the magnetisation until $\vec{H}_{C2}$, when the normal cores overlap and the superconductor is driven normal.

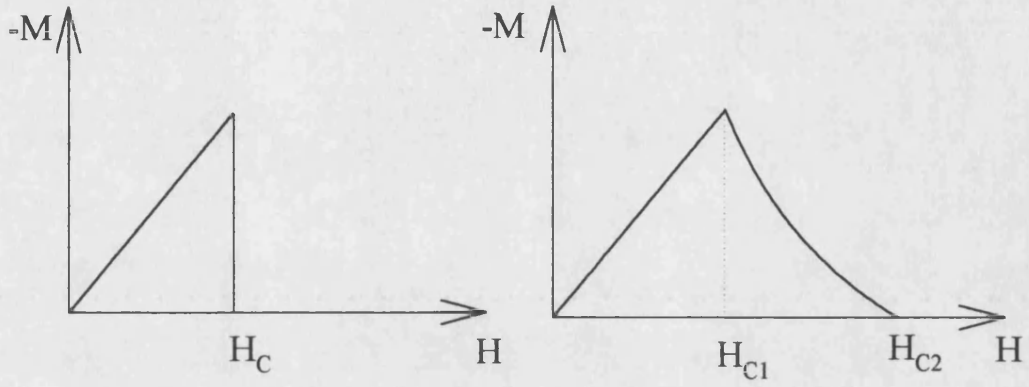

Type I Type II

Figure 2.3. Magnetisation curves for ideal type I and type II superconductors.

Although very clean superconductors exhibit this ideal behaviour, most real superconductors are not pure and may contain impurities, grain boundaries, twinning planes, defects and dislocations. These have the effect of introducing hysteretic behaviour into the magnetisation curves, as will be discussed further in later chapters. Another major variation from the ideal behaviour described above is what happens in the mixed state in so-called high temperature superconductors.

Many of these materials exhibit different vortex phases within the mixed state, such as a vortex liquid, a vortex solid, a 2 dimensional vortex glass state, or a hexagonal vortex lattice. All of these features will be described further in the next chapter.

2.3 Electrodynamics of Superconductors - the London Equations

The first attempt to describe superconductivity was made by F. and H. London [F. London and H. London, 1935]. In their model, the laws of electromagnetism are applied to a material with infinite conductivity, and then certain restrictions are employed to describe the expulsion of flux in the Meissner state. The London model is not a full microscopic theory of superconductivity, but it does quantitatively describe the magnetic properties of the superconducting state remarkably well.

The London model is based on the two-fluid model, which was first proposed to describe superfluidity in liquid helium. The two-fluid model treats the superconductor as an ordinary conductor, but with a certain fraction of its' electrons behaving as superelectrons which are able to pass through the material without resistance. At absolute zero, all the conduction electrons are superelectrons, but as the temperature is increased, the fraction of normal electrons increases until at the critical temperature all the conduction electrons behave as normal electrons. Thus, the total electron concentration is the sum of the superelectron density n_s and the normal electron density n_n, with temperature limits given by $n(T=0)=n_s$ and $n(T=T_C)=n_n$.

If the laws of electrodynamics are applied to a superconductor, treating it as a normal metal with an infinite conductivity and n_s superelectrons per unit volume, it can be shown that the time derivative of the magnetic flux density is given by

$$\nabla^2 \frac{\partial \vec{B}}{\partial t} = \frac{\mu_0 n_s e^2}{m} \frac{\partial \vec{B}}{\partial t}, \tag{2.1}$$

where e and m are the charge and mass of the electron. If the geometry is restricted to a semi-infinite half-space with a planer superconductor – normal interface, and an external magnetic field is applied parallel to this plane, the solution of (2.1) is given by

$$\frac{\partial \vec{B}}{\partial t} = \frac{\partial \vec{B}_a}{\partial t} e^{-\frac{x}{\sqrt{a}}} \tag{2.2}$$

with $\alpha = \frac{m}{\mu_0 n_s e^2}$ and $\vec{B}_a = \mu_0 \vec{H}_a$, the flux density due to the applied field. This means that any time variations in $\vec{B}$ will decay away inside the superconductor beyond a length $\sqrt{\alpha}$, so that even a time-varying applied field will become constant inside the material. This solution, however, is only true for a perfect conductor – it does not account for the Meissner effect of zero flux density inside a superconductor. F and H London suggested that (2.1) may also apply to the flux density itself, rather than just to the time-derivative. If this were true, (2.2) would become

$$\vec{B} = \vec{B}_a e^{-\frac{x}{\sqrt{\alpha}}}, \tag{2.3}$$

showing that the magnetic flux density only penetrates a distance $\sqrt{\alpha}$ into the superconductor, which is consistent with the Meissner effect since far inside the superconductor $\vec{B} = 0$. This is achieved with screening currents (often called shielding, or Meissner currents) which flow around the perimeter of the superconductor in a "skin depth" of thickness $\sqrt{\alpha}$ and generate a magnetic flux density which exactly cancels that of the applied field.

The relationships between the magnetic induction, $\vec{B}$, and the screening currents, $\vec{J}_S$, are given by the two London equations

$$\vec{B} = \frac{-m}{n_s e^2} \vec{\nabla} \wedge \vec{J}_s \tag{2.4}$$

$$\frac{d\vec{J}_S}{dt} = \frac{n_s e^2}{m} \vec{E} \tag{2.5}$$

The distance $\sqrt{\alpha}$ is known as the London penetration depth, λ_L, and is the distance at which the flux density has fallen to 1/e of its full value outside the superconductor, as shown in Figure 2.4.

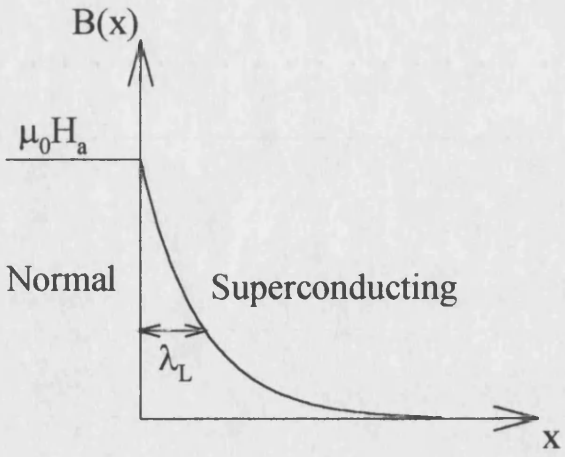

Figure 2.4. Decay of the magnetic flux density inside a superconductor.

Since the penetration depth is a function of the superelectron density, and this is a function of temperature, the penetration depth will change with temperature, rising rapidly near the critical temperature and approaching a saturation value at lower temperatures. Several different models for this temperature dependence have been suggested, with the two-fluid model predicting a dependence of

$$\lambda(T) = \frac{\lambda_0}{\sqrt{1-\left(\frac{T}{T_c}\right)^4}}, \tag{2.6}$$

and this temperature dependence is shown in Figure 2.5 below.

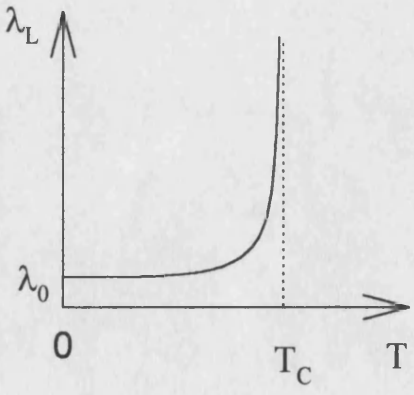

Figure 2.5. Temperature dependence of the London penetration depth, λ_L, as predicted by the two-fluid model.

The saturation value λ_0 ranges from 10-50nm for elemental superconductors (e.g. Nb, Pb or Sn) to as much as 200nm for the high temperature superconductors such as $Bi_2Sr_2CaCu_2O_{8+\delta}$ or $YBa_2Cu_3O_{7-\delta}$.

As the critical temperature is approached from below, the penetration depth increases until at T_C it diverges. This is consistent with the idea that as the temperature approaches T_C, the magnetic flux density penetrates deeper into the superconductor, until at T_C a uniform flux profile is present throughout the material and the superconductor becomes normal.

Although the London model predicts the Meissner effect and describes the electromagnetic properties of a type I superconductor very well, it requires modifications to describe situations where the supercurrent density varies in space, such as the mixed state in type II superconductivity. In this case, the conventional London equation is replaced by the modified version

$$\lambda_L^2 \nabla^2 \vec{B} - \vec{B} = \vec{\Phi}_0 \delta_2, \tag{2.7}$$

where δ_2 is a two dimensional delta function used to account for the vortex core. This equation is valid in the London limit, which is when the diameter of the vortex core is very small compared with other dimensions i.e. $\kappa >> 1$. This makes it particularly useful for the high temperature superconductors which can have κ values as high as 100 for BSCCO.

2.4 Ginzburg Landau Theory

Although remarkably successful at predicting the electrodynamic properties of superconductors, the London equations are purely empirical, and are based on a classical model of superelectron particles that propagate through the superconductor with no resistance. An alternative theory was suggested by Ginzburg and Landau [V. L. Ginzburg and L. D. Landau, 1950] who proposed a "wavefunction" $\psi(\mathbf{r})$ to represent the behaviour of the superelectrons and this was used as an order parameter

for the superconducting state, defined such that $|\Psi(r)|^2 = n_s$, the superelectron density. This was an improvement over the London theory because it could allow for situations where the superelectron density varied in space, such as the mixed state in type II superconductors.

The principle assumption of the Ginzburg Landau theory is that the free energy density of the superconducting state, f_s, can be expanded as a power series of ψ:

$$f_s = f_n + \alpha|\Psi|^2 + \tfrac{1}{2}\beta|\Psi|^4 + \frac{1}{2m^*}\left|\left(-i\hbar\nabla - e^*\vec{A}\right)\Psi\right|^2 + \tfrac{1}{2}\mu_0\left|\vec{H} - \vec{H}_i\right|^2 \qquad (2.8)$$

where f_n is the free energy of the normal state, ψ is the superelectron order parameter, with the superelectrons having mass and charge m^* and e^*. $\vec{H}$ is the applied external magnetic field, $\vec{H}_i$ is the field inside the superconductor and $\vec{A}$ is the magnetic vector potential, defined by $\vec{B} = \vec{\nabla} \wedge \vec{A}$.

When the order parameter falls to zero, equation (2.8) reduces to

$$f_s = f_n + \tfrac{1}{2}\mu_0\left|\vec{H} - \vec{H}_i\right|^2, \qquad (2.9)$$

the free energy of the normal state in the presence of a magnetic field (since when ψ=0, the superconductor is in the normal state). In the case of zero applied magnetic field and no gradients, $\vec{A}$ can be chosen to be zero and equation (2.8) reduces to

$$f_s = f_n + \alpha|\Psi|^2 + \tfrac{1}{2}\beta|\Psi|^4. \qquad (2.10)$$

The stable equilibrium energy is found by minimising (2.10) with respect to $|\Psi|^2$, and this leads to the condition

$$|\Psi|^2 = -\frac{\alpha}{\beta}. \qquad (2.11)$$

From (2.10), β must be positive, or the minimum energy would be obtained for an arbitrarily large $|\Psi|^2$, or n_s, which is not physical. For the parameter α, there are

two possible cases. Firstly, if α is positive, the minimum energy occurs at $|\Psi|^2=0$, which corresponds to the normal state. Secondly, if α is less than zero, the minimum energy occurs at $|\Psi|^2 = \left|\frac{\alpha}{\beta}\right|$ which is physical and non-zero (See Figure 2.6).

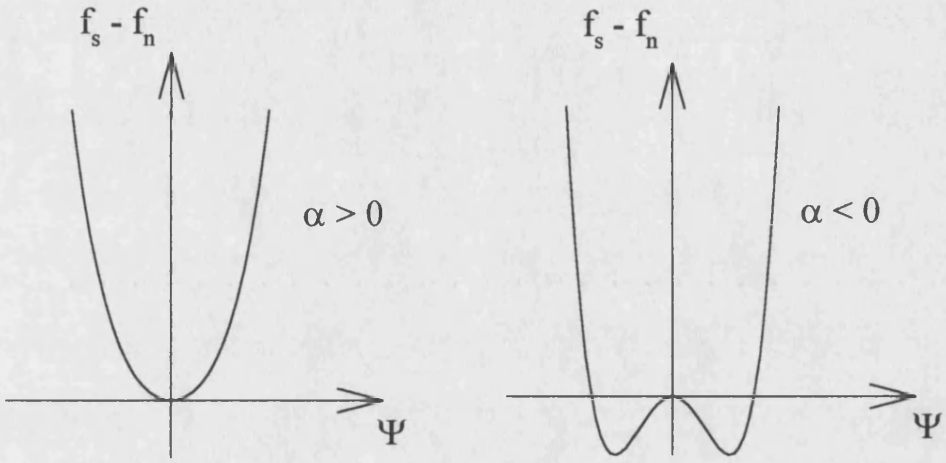

Figure 2.6. Two possible minimum energy positions for the parameter α greater than, or less than zero (corresponding to $T>T_C$ and $T<T_C$).

Substituting this value of $|\Psi|^2$ back into equation (2.10) and using the expression for the thermodynamic critical field $\vec{H}_C$ (which is the field at which the magnetic energy is equal to the superconducting condensation energy)

$$\tfrac{1}{2}\mu_0 H_C^2 = f_s - f_n, \tag{2.12}$$

explicit expressions for α and β in terms of the material parameters $\vec{H}_C$ and n_s can be obtained:

$$\alpha = -\mu_0 \frac{H_C^2}{n_s} \tag{2.13}$$

$$\beta = \mu_0 \frac{H_C^2}{n_s}. \tag{2.14}$$

When fields, currents or gradients are present, $\Psi(\vec{r})$ adjusts itself to minimise the overall free energy (equation (2.8)), and this leads to the two Ginzburg-Landau equations for Ψ in terms of $\vec{A}$, $\vec{J}$, m^* and e^* given below.

$$\alpha \Psi + \beta |\Psi|^2 \Psi + \frac{1}{2m^*}\left(-i\hbar\nabla - e^* \vec{A}\right)^2 \Psi = 0 \tag{2.15}$$

$$\vec{J} = \frac{-i\hbar e^*}{2m^*}\left(\Psi^* \nabla\Psi - \Psi \nabla\Psi^*\right) - \frac{e^{*2}}{m^*}\Psi^* \Psi \vec{A}. \tag{2.16}$$

Equations (2.15) and (2.16) cannot generally be solved analytically but need to be solved numerically. If there are no magnetic fields present, equation (2.15) can be rewritten as

$$\frac{\hbar^2}{2m^*\alpha}\frac{d^2 f}{dx^2} + f - f^3 = 0, \tag{2.17}$$

where f is given by

$$f = -\frac{\beta}{\alpha}\Psi. \tag{2.18}$$

The coefficient of the differential term is a characteristic length scale for variations in the wavefunction, and is known as the coherence length ξ. The coherence length is temperature dependent, and varies in a similar way to the London penetration depth, diverging at T_C and approaching a saturation value at lower temperatures. The

Ginzburg-Landau expression for the temperature dependence of the coherence length is given by

$$\xi(T) = \frac{\xi_0}{\sqrt{1 - \frac{T}{T_C}}}, \tag{2.19}$$

and this is shown in Figure 2.7.

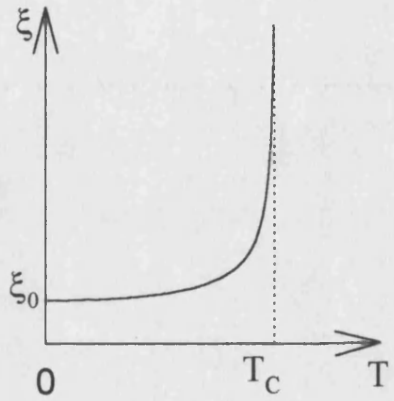

Figure 2.7. Temperature dependence of the coherence length.

The main limitations to the Ginzburg-Landau theory are that the power series expansion of the order parameter is only valid near T_C, and the expression for $\xi(T)$ is only valid in fields near $\vec{H}_{C2}(T)$. Within these restrictions, Ginzburg-Landau theory has proved to be a very useful tool for studying the mixed state of type II superconductors.

2.5 Interface Energy

The two fundamental length scales of superconductivity have now been introduced: the penetration depth λ, corresponding to the distance over which applied fields decay inside the superconductor, and the coherence length ξ, defining the smallest distance over which the superconducting order parameter ψ can change value. It is useful to calculate the ratio of these length scales and this is known as the Ginzburg-Landau parameter, κ, defined as

$$\kappa = \frac{\lambda}{\xi} . \tag{2.20}$$

The Ginzburg-Landau parameter has a very weak temperature dependence, since the temperature dependencies of λ and ξ are similar.

One consequence of the existence of a coherence length is that the boundary between a normal and superconducting region cannot be sharp, since in the superconducting region n_s will reach it's bulk value over a distance ξ, while any magnetic flux will decay over a distance λ, as shown in Figure 2.8.

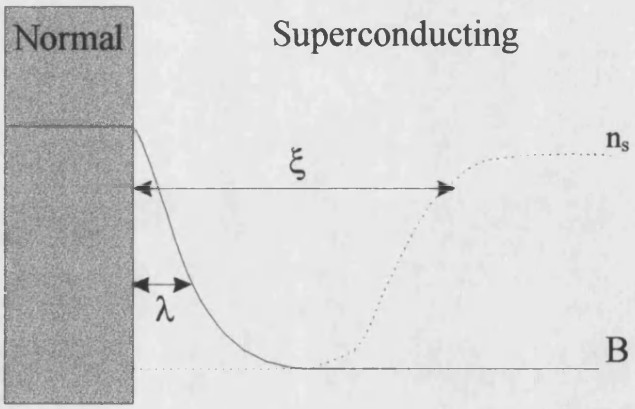

Figure 2.8. Variation of the superelectron density (n_s) and magnetic flux density (B) near a superconducting-normal boundary.

Consider the free energy density at the boundary. The normal region has a free energy density f_n, and the superconducting region has two contributions to the free energy density. First, there is a magnetic contribution, which increases the energy relative to the normal region by an amount $\frac{1}{2}\mu_0 H_C^2$, and secondly there is a contribution due to the presence of the ordered superelectrons, which lowers the energy density by an amount f_n-f_s. If the boundary is to be stable, then far from the boundary the two free energy densities must be equal so f_n-$f_s = \frac{1}{2}\mu_0 H_C^2$, as shown in Figure 2.9.

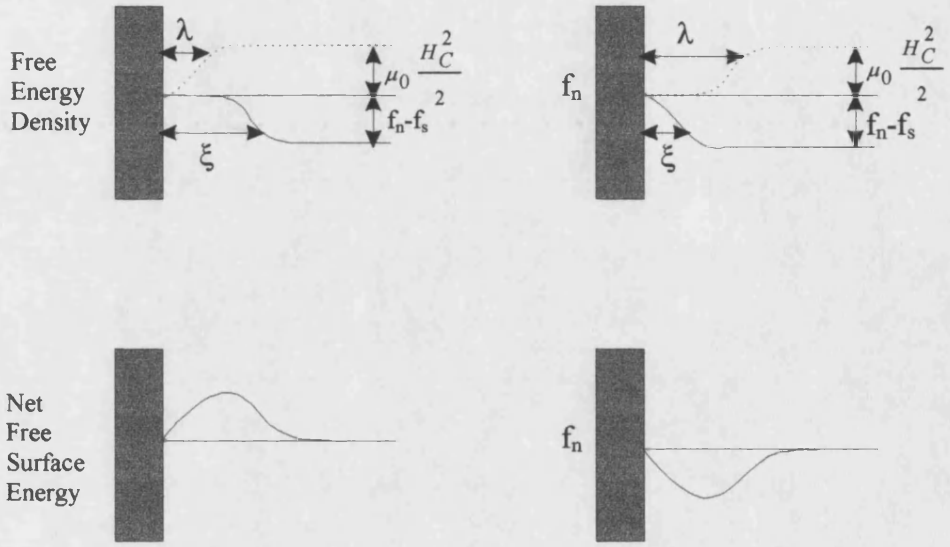

Figure 2.9. Energy contributions near a normal-superconducting boundary, for a type I (left) and type II (right) superconductor.

However, near the boundary the two contributions do not cancel and there is a net energy density of $\frac{1}{2}\mu_0 H_C^2(\xi-\lambda)$. This net energy will be positive if $\xi>\lambda$ and negative if $\xi<\lambda$. The net energy density near a superconducting-normal interface is the origin of type I and type II superconductivity. If $\lambda<\xi$ and the interface energy is positive, then the equilibrium situation is achieved by minimising the number of interfaces. On the other hand, if $\lambda>\xi$ and the interface energy is negative, then the most stable situation is achieved by having lots of normal-superconducting

boundaries, and this situation is realised in the mixed state. Hence, if a superconductor has a value of $\kappa<1$, then it is a type I material, and if $\kappa>1$ then it is type II. A more accurate consideration using the Ginzburg-Landau (G-L) theory shows that the sign of the interface energy changes when $\kappa = \frac{1}{\sqrt{2}}$.

2.6 The Mixed State

As shown with the surface energy argument, a type II superconductor ($\kappa > \frac{1}{\sqrt{2}}$) attains a minimum energy state by maximising the amount of normal-superconducting boundary. This is realised by having lots of normal field-carrying regions threading the bulk of the superconductor, with supercurrents flowing around the cores to generate a magnetic field parallel to the applied field. This mixture of normal and superconducting regions co-existing is known as the mixed state, predicted to exist theoretically by Abrikosov, who found a periodic solution to the G-L equations [A. A. Abrikosov, 1957]. In this solution, the minima in ψ correspond to the superelectron density n_s going to zero, which means that the superconductor is locally in the normal state, in agreement with a picture of maximising the amount of normal-superconducting boundary.

The structure of a normal core surrounded by a circulating supercurrent is known as a magnetic flux vortex, or fluxon, and the dimensions of these structures are intimately related to the superconductor parameters. The core is approximately circular and has a radius of ξ, the coherence length, and the flux decays over a distance λ outside the core, leading to the vortex structure shown in Figure 2.10. The flux density decays to 1/e of the value at the core centre over a distance of λ and the superelectron density decays to zero at the centre of the core over a distance of ξ. The sign change of the supercurrent density is a result of the circular motion of the supercurrents as they circulate around the core. Before a superconductor can enter the mixed state, a minimum magnetic field must be applied to overcome the screening currents and make the mixed state energetically favourable, and this is known as the lower critical field, $\vec{H}_{C1}$. If the applied field is further increased, the vortices become more closely

packed until eventually, at the upper critical field $\vec{H}_{C2}$, the normal cores begin to overlap and the superconductor is driven into the normal state.

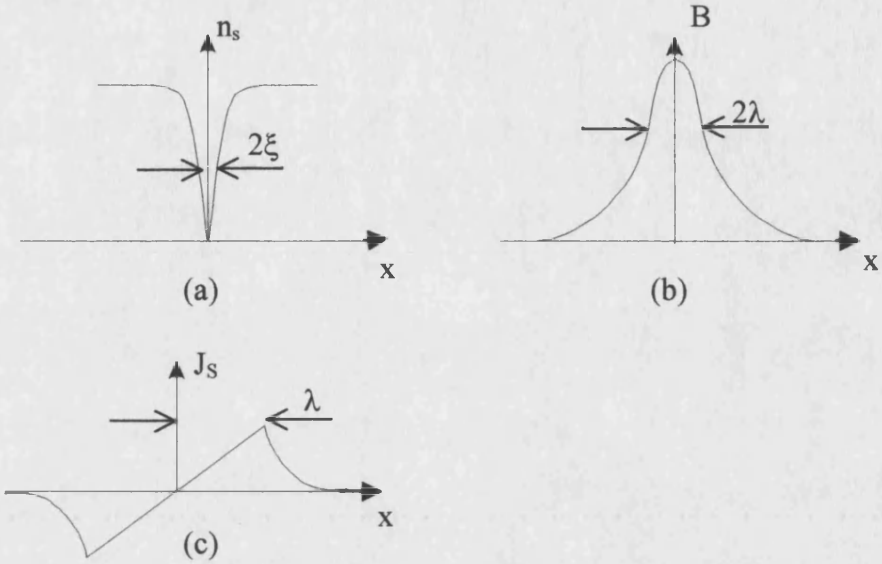

Figure 2.10. Variation in superelectron density (a), flux density (b) and supercurrent density (c) near a flux vortex.

Due to the single-valued nature of the order parameter, each vortex contains a quantized amount of magnetic flux Φ_0, equal to 2.068×10^{-15} Wb, and this can be shown as follows. The second Ginzburg Landau equation can be written as

$$\vec{J} = -\left(\frac{q^{*2}}{m^*}\vec{A} + \frac{q^*\hbar}{2m^*}\nabla\phi\right)|\Psi|^2 \tag{2.21}$$

with the complex order parameter represented by $|\Psi|e^{i\phi}$. If the current density is now integrated around a closed path enclosing an isolated vortex core, and at a distance far enough away for there to be no current, then

$$\oint \vec{J}.\vec{d\ell} = 0 = \oint\left(\frac{q^{*2}}{m^*}\vec{A} + \frac{q^*\hbar}{m^*}\nabla\phi\right).\vec{d\ell}\,. \tag{2.22}$$

For the first term, Stokes' theorem gives

$$\oint \frac{q^{*2}}{m^*}\vec{A}.\vec{d\ell} = \int \frac{q^{*2}}{m^*}\vec{\nabla}\wedge\vec{A}.\vec{ds} = \int \frac{q^{*2}}{m^*}\vec{B}.\vec{ds} = \frac{q^{*2}\Phi}{m^*}, \tag{2.23}$$

where Φ is the total enclosed flux. For the second term, the integral must be equal to an integer multiple of 2π for the order parameter to be single valued. Hence we get

$$\frac{q^{*2}\Phi}{m^*} + \frac{q^*\hbar}{m^*}2\pi n = 0, \tag{2.24}$$

and recalling that q^*=2e, this shows that the flux is quantized in units of $\frac{h}{2e}$, with the smallest allowed quantum of flux being 2.068×10^{-15} Wb.

The magnetic field due to a single, isolated vortex can be found by solving the modified London equation

$$\lambda^2\nabla^2\vec{B} - \vec{B} = \vec{\Phi}_0\delta_2(r), \tag{2.25}$$

where $\delta_2(r)$ is a 2 dimensional delta function included to account for the normal cores. This model assumes that the normal core is infinitely narrow, and has a solution

$$\vec{B}(r) = \frac{\vec{\Phi}_0}{2\pi\lambda^2}K_0\left(\frac{r}{\lambda}\right), \tag{2.26}$$

where K_0 is a Hankel function of zero order and $\vec{\Phi}_0$ is a vector of magnitude the flux quantum and direction parallel to the applied field. Since this expression diverges at the origin, the London model fails in this regime, but it is a good approximation in the region $\vec{H}_{C1} < \vec{H}_a << \vec{H}_{C2}$, where the vortices are far enough apart for the structure of the cores to be unimportant. The asymptotic approximation for K_0 in the limit $r\ll\lambda$ leads to

$$\vec{B}(r) \approx \frac{\vec{\Phi}_0}{2\pi\lambda^2} \ln\left(\frac{\lambda}{r}\right) \tag{2.27}$$

and in the limit r»λ the magnetic flux density is approximated by

$$\vec{B}(r) \approx \frac{\vec{\Phi}_0}{2\pi\lambda^2} \sqrt{\frac{\pi\lambda}{2r}} e^{\frac{-r}{\lambda}}. \tag{2.28}$$

Equation (2.26) is plotted in Figure 2.11 below, assuming a penetration depth of 250nm, but is not evaluated at the origin, since the London model is not valid in this regime.

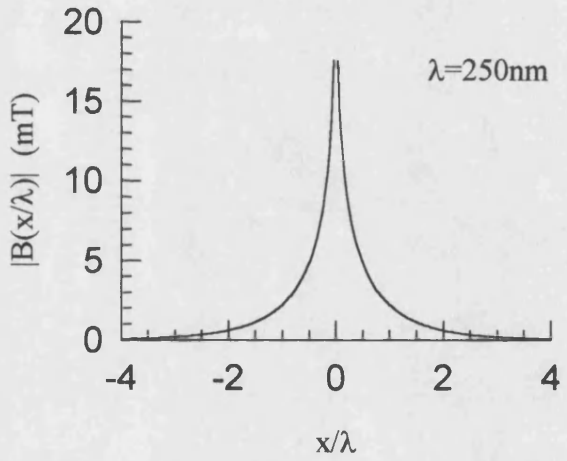

Figure 2.11. Vortex structure evaluated using the London model.

Associated with each vortex is a line energy, ε_0, (also called line tension) which is the sum of the magnetic field energy and the kinetic energy of the supercurrents, given by

$$\varepsilon_0 = \iint \left[\frac{|\vec{B}|^2}{2\mu_0} + \frac{1}{2} m v^2 n_s \right] dS. \tag{2.29}$$

Using Maxwell's equations to relate the supercurrent to the applied field (2.29) becomes

$$\varepsilon_0 = \frac{1}{2\mu_0}\iint\left[\left|\vec{B}\right|^2 + \lambda^2\left|\left(\nabla \wedge \vec{B}\right)\right|^2\right]dS, \tag{2.30}$$

and evaluating this integral (but excluding the core region) and using the approximation given in (2.28), the line energy per unit length of an isolated vortex is given approximately by

$$\varepsilon_0 \approx \frac{\Phi_0^2}{4\pi\mu_0\lambda^2}\ln(\kappa). \tag{2.31}$$

Because of the interaction between the supercurrent of one vortex with the fields of a neighbouring vortex, there will be an inter-vortex interaction. The quadratic dependence of ε_0 on Φ means that the interaction between two parallel vortices must be repulsive, since the single quantum vortex is the most energetically favourable.

The inter-vortex force can be estimated by taking the partial derivative of the vortex line interaction energy with respect to r, and this leads to a repulsive force with a magnitude given by

$$\left|\vec{f}\right| = \frac{\Phi_0^2}{2\pi\mu_0\lambda^3}\sqrt{\frac{\pi\lambda}{2r}}\,e^{-\frac{r}{\lambda}}. \tag{2.32}$$

This inter-vortex repulsion leads to the formation of a stable lattice structure of vortices in the mixed state of type II superconductors. The stable lattice configuration in a perfect superconductor (i.e. no pinning centres) is a hexagonal lattice with a vortex on each vertex of an equilateral triangle, as shown in Figure 2.12. The image of a vortex lattice in Figure 2.12(a) is taken from a crystal of BSCCO cooled in an applied field $\mu_0\vec{H}_a = 1.6$ mT to a temperature of 81 K using a Scanning Hall Probe Microscope (SHPM). Figure 2.12(b) shows the six-fold symmetry of the lattice, and the definition of the lattice constant a_o.

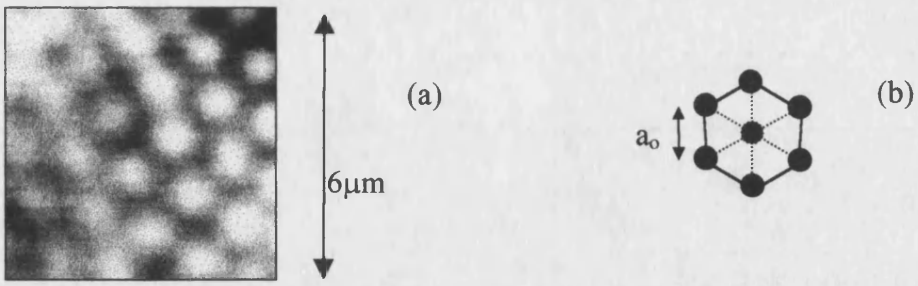

Figure 2.12. The hexagonal vortex lattice in a crystal of BSSCO (a) [After Bending *et al.*, 1999] and drawn schematically (b).

2.7 Flux Pinning and the Critical State

In the mixed state of a perfect (no pinning centres) type II superconductor, the vortex lattice is stabilised by the inter-vortex repulsion and the vortex-surface repulsion. However, if a transport current is applied, there will be a Lorentz force which acts on the vortices, causing them to move. The Lorentz force per unit length is given by

$$\vec{f}_L = \vec{J} \wedge \vec{\Phi}_0 , \tag{2.33}$$

and the resulting eddy currents, induced by the vortex motion, cause dissipation of energy and hence a potential difference in the superconductor. To counter this, most superconductors have the ability to "pin" vortices in place. Flux pinning is a result of a local depression in the Gibbs free energy for the vortices, and can be caused by material impurities, grain boundaries, local inhomogeneities or geometrical effects such as grooves, indentations, etc. These pinning mechanisms are generally active throughout the material and are known as bulk pinning effects, whereas surface pinning forces (such as geometrical barriers or Bean-Livingston barriers described later) are only important near the edges, in samples which have very little bulk pinning.

The pinning force per unit length, $\vec{f}_p$, opposes flux motion and the Lorentz force must be greater than this for vortex motion, and this leads to the critical state.

When a superconductor is in the critical state, the Lorentz force exactly matches the pinning force and the vortices are on the verge of moving. In this case, the critical condition is given by

$$\vec{J} \wedge \vec{\Phi}_0 = \vec{f}_p, \tag{2.34}$$

where $\vec{J}$ is the total current density (transport current + Meissner current) and $\vec{\Phi}_0$ is the flux quantum. Several models have been suggested to describe superconductors in the critical state, and the famous Bean model will be described here briefly [C. P. Bean, 1962]

For this model of the critical state, two assumptions are made. First, the Meissner state is ignored and secondly, for low applied fields the outer part of the superconductor is assumed to be in the critical state whilst the inner part is shielded from the currents and fields. In the critical region, the critical current (which is the maximum current that can be sustained without dissipation) is dependent on the magnetic flux density.

Using Maxwell's equation $\vec{\nabla} \wedge \vec{B} = \mu_0 \vec{J}$, the critical condition can be expressed as

$$\left(\vec{\nabla} \wedge \vec{B}\right) \wedge \frac{\vec{B}}{\mu_0} = \vec{f}_p, \tag{2.35}$$

where $\vec{f}_p$ is the volume pinning density in Nm^{-3}. This is a very difficult problem, since in general the pinning force will have a complicated dependence on $\vec{B}$, and may have components in either two, or all three dimensions. The situation can be simplified if an infinite slab geometry is used, with a field applied parallel to the plane. In this case, (2.35) reduces to

$$\frac{\partial B_z}{\partial y} B_z = \mu_0 \left| \vec{f}_p(B_z) \right|. \tag{2.36}$$

In order to find the flux profile $B_z(y)$, only the dependence of the pinning force on $\vec{B}$ is required. In the Bean model, a dependence of $f_p = J_c B_z$ and a field-independent critical current is suggested, and applying this to (2.36) gives a linear dependence of B_z on y:

$$B_z(y) = \mu_0 J_c |y| + c, \tag{2.37}$$

where the constant c is determined by the boundary condition that at the sample edges, $\vec{B} = \mu_0 \vec{H}_a$. The profiles predicted by this model are shown in Figure 2.13, where it is clear that as the applied field is increased from zero, the flux density begins to penetrate from the edges towards the centre, with a constant slope equal to $\mu_0 J_c$.

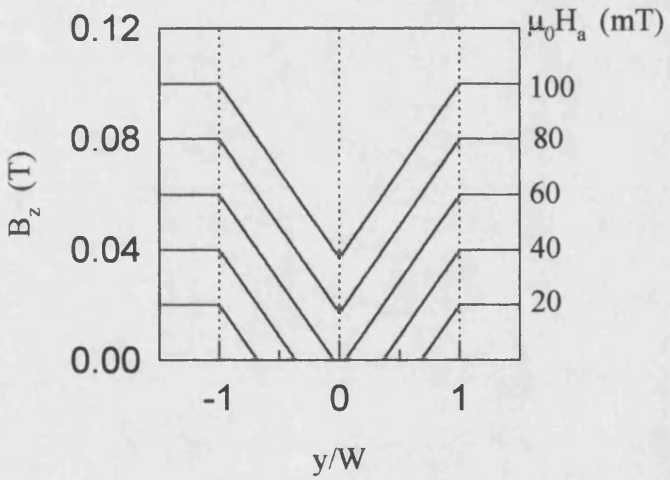

Figure 2.13. Flux profiles across an infinite slab for increasing values of applied field from an initially unmagnetised state. Calculated using the Bean model, assuming a field independent critical current density of 10^7 Am^{-2}.

Full field penetration occurs when there is no longer any vortex free region in the centre, and this occurs at a field $\vec{H}_P = J_c W$, where 2W is the thickness of the slab.

In order to model a more realistic experimental geometry, Brandt and Zeldov independently considered the case of a field applied normal to a thin film, and calculated the resulting flux profiles in the critical state both with, and without an

applied transport current [E. H. Brandt *et al.*, 1993, E. H. Brandt and M. V. Indenbom, 1993 and E. Zeldov *et al.*, 1994]. The geometry used is shown in Figure 2.14. In this geometry, demagnetisation effects become very important. The field at the edge of the superconductor, $\vec{H}_{edge}$, is given by

$$\vec{H}_{edge} = \frac{1}{1-N_D}\vec{H}_a, \tag{2.38}$$

where N_D is the demagnetising factor.

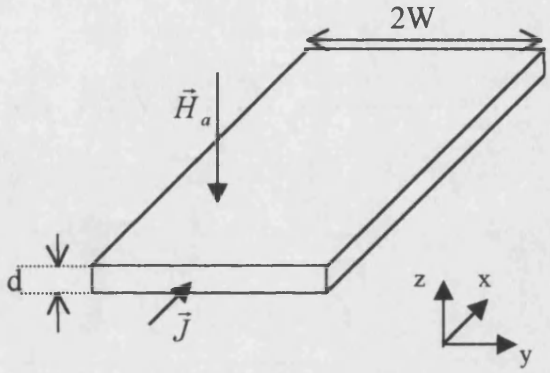

Figure 1.14. Geometry used in Brandt's thin film model.

For long ellipsoidal geometries with the field applied along the length, N_D=0, and for spheres $N_D=\frac{1}{3}$, but for the platelet geometry described above, $N_D \approx 1$. This means that flux enters the superconductor almost as soon as a field is applied (neglecting surface barriers and flux pinning). Using Ampere's law, Brandt showed that the flux profile is given by

$$B_z = 0 \qquad |y| < b \tag{2.39}$$

$$B_z = \mu_0 \left|\vec{H}_a\right| \tanh^{-1}\left(\frac{\sqrt{y^2-b^2}}{c|y|}\right) \qquad b < |y| < W, \tag{2.40}$$

where (W-b) is the distance into the superconductor that vortices have penetrated for a given applied field, and is given by

$$b = \frac{W}{\cosh\left(\frac{|\vec{H}_a|}{|\vec{H}_C|}\right)}, \tag{2.41}$$

and c is a constant given by

$$c = \tanh\left(\frac{|\vec{H}_a|}{|\vec{H}_C|}\right). \tag{2.42}$$

Figure 2.15 shows the profiles obtained from Brandt's model, for a magnetic field applied normal to an initially unmagnetised semi-infinite film.

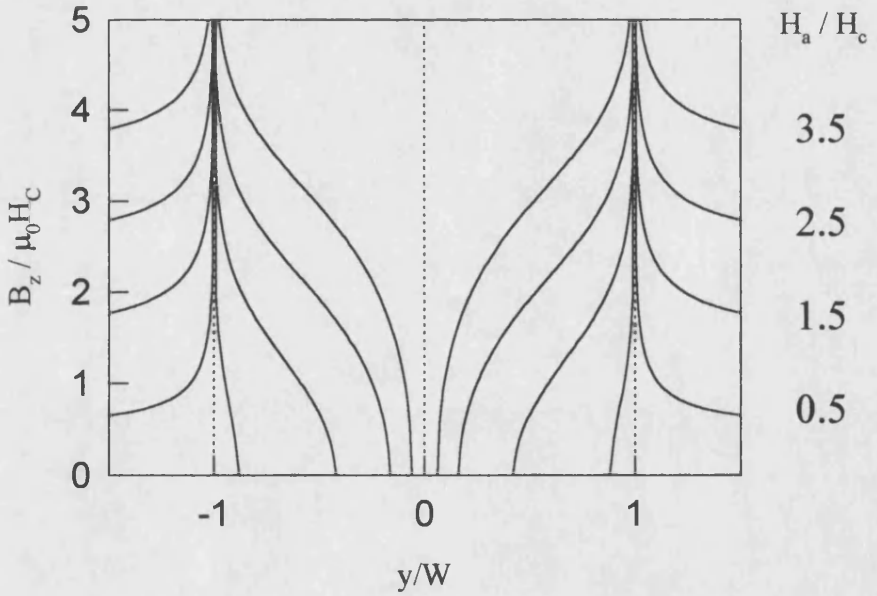

Figure 2.15. Flux profiles calculated from Brandt's model of the critical state in a thin film.

Pinning centres prevent vortices from reaching the equilibrium arrangement for the flux lattice and effectively create a "vortex glass" structure, and the only way of overcoming this is to go beyond the critical state. However, Anderson showed that at finite temperatures, and over a long enough time scale, the vortices may jump from their pinning sites via thermal activation [P. W. Anderson, 1962]. This relaxation process is particularly important in high temperature superconductors because of the relatively large thermal energies available and leads to a distinction between an *equilibrium* magnetisation curve and a *hysteretic* magnetisation curve. According to the theory of Anderson, and subsequent experiments by Kim and others [Y. B. Kim *et al.*, 1963], the magnetisation should decay logarithmically towards an equilibrium value, with vortices entering the superconductor on the increasing leg of the hysteresis loop end exiting the superconductor on the decreasing leg. This relaxation process is symmetric with respect to vortex entry or exit, although effects such as surface barriers have been shown to modify this symmetry (See chapter 3).

Chapter 3

High Temperature Superconductivity

3.1 Discovery of the HTSC's

In 1986, Bednorz and Müller discovered superconductivity in a compound of Lanthanum, Barium and Copper Oxide, which had a critical temperature of 35K [J. G. Bednorz and K. A. Müller, 1986]. This was higher than the maximum at that time of 23K, which had been reached 13 years earlier by Gavalar in Nb_3Ge [J. R. Gavalar, 1973], and it earned Bednorz and Müller a Nobel Prize in the following year. This discovery was soon followed up with other ceramic superconducting materials which had critical temperatures of 90K (YBaCuO) [M. K. Wu *et al.*, 1987], 110K (BiSrCaCuO 2223) [H. Maeda *et al.*, 1988] and 130K (TlBaCaCuO) [Z. Z. Scheng and A. M. Hermann, 1988] being discovered in a remarkably short space of time (see Figure 3.1). The fact that many of these new materials had transition temperatures greater than the boiling point of liquid nitrogen (77K) made practical applications of superconductivity a real possibility. The initial excitement has been tempered, however, with the realisation that the ceramic nature of the high temperature superconductors presents significant materials science difficulties. Despite this, superconductivity has found applications in areas such as high-field magnets, very sensitive magnetic sensors known as SQUID's (Superconducting Quantum Interference Devices) [See for example, J. Clark, 1990, or J. Gallop, 1991], and electronic components (for example, mixers [P. L. Richards and Q. Hu, 1989], filters [G. C. Lang *et al.*, 1993] or antennae [R. C. Hansen, 1990]).

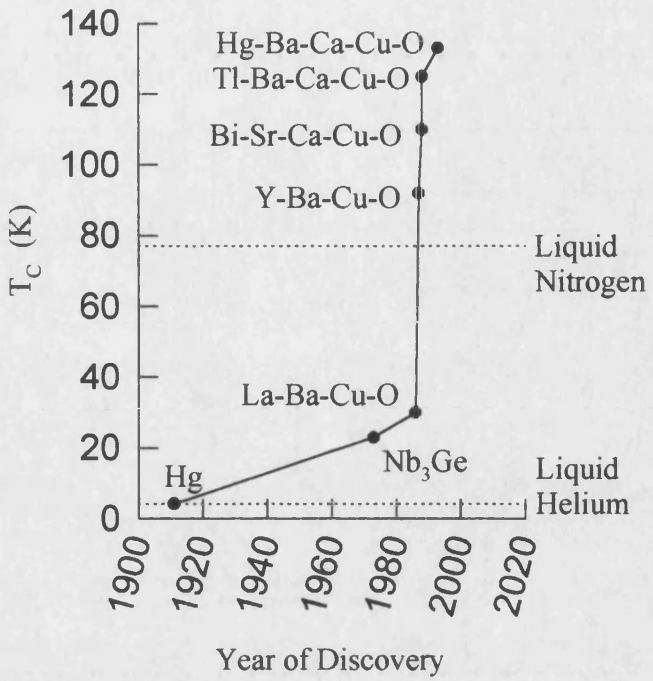

Figure 3.1. Discovery of some of the high temperature superconductors.

As well as the potential practical applications of high temperature superconductivity, there is exceptional interest from a pure science point of view. The mechanism of superconductivity in these materials is not well understood, the magnetic properties appear to be very complex (see chapter 4), and many of the parameters are extremely large, with values of the upper critical field exceeding 100T for some of the superconductors at low temperatures. Measurement of the fundamental superconducting properties λ and ξ for these materials is not trivial, but is nevertheless important, since they can yield information about the underlying mechanism of superconductivity, and define properties such as the lower and upper critical magnetic fields. Since many of the high temperature superconductors have a relatively small electron density, the penetration depth is larger than for the conventional superconductors, typically about 1500 Å, and the coherence length is typically between 10-100 Å, leading to very large G-L parameters. The large κ values mean that all these materials are type II superconductors, with the mixed state taking up a large portion of the magnetic phase diagram. However, thermal fluctuations are more important at the higher temperatures in these materials, which leads to effects such as vortex creep, and a smearing of the transition at the upper critical field, as described later.

The crystal structure of the high temperature superconductors also has an effect on the superconducting properties. All these materials are based on a perovskite structure, with varying numbers of copper-oxide (CuO) planes per unit cell. The basic perovskite structure is shown in Figure 3.2, and consists of two metallic cations (A and B), with 12 anions lying on the cube edges. The A cation is larger, and lies in the centre of the cube.

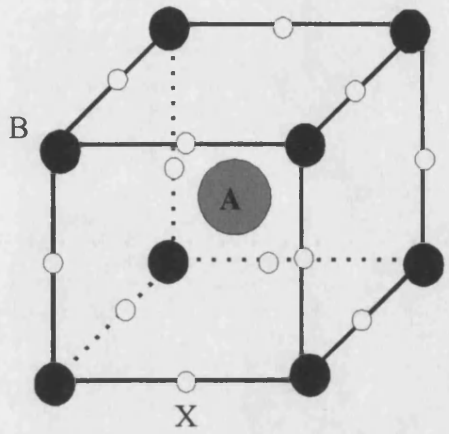

Figure 3.2. The basic perovskite structure.

This perovskite structure provides the basic building block for all the high temperature superconductors, with the X anion often oxygen. In the case of YBCO, the A sites are occupied by barium and yttrium ions, and the smaller copper ions occupy the B sites. Stacking of these structures leads to a very anisotropic crystal structure, with the copper and oxygen ions creating CuO planes, which are separated by the larger ions in the structure. A diagram of the crystal structure of BSCCO is given in chapter 4, along with some of the unit cell dimensions and the CuO plane separation, which is an important parameter. The effect of this layered structure on the superconductivity is dramatic; since the CuO planes are weakly coupled, the superconductivity is carried mainly in-plane, leading to highly anisotropic transport properties. Also, in the mixed state with a magnetic field applied perpendicular to the planes, the vortex consists of a stack of two-dimensional "pancake" vortices, which are only weakly coupled together (via the Josephson interaction and electromagnetic

coupling). In certain regimes these pancakes can become completely decoupled, leading to two-dimensional behaviour, which has implications for effects such as thermal activation and vortex creep.

3.2 Abrikosov Vortex Solid Melting

As described earlier, when an ideal type II superconductor (no bulk pinning or surface barriers) is in the mixed state, the magnetic vortices penetrate into the sample and generally form a hexagonal lattice. At T=0, if there is no transport current applied, the vortices do not move from their ordered sites. However, at finite temperatures the vortices are thermally agitated about their equilibrium positions by an amount δr (See Figure 3.3). Within the phenomenological Lindemann picture of vortex solid melting, if the rms value of this amplitude, as defined by

$$\Delta r = \sqrt{\langle \delta r^2 \rangle}, \tag{3.1}$$

exceeds a certain fraction of the mean vortex spacing a_o, the vortex solid may melt and the vortices are free to move around the superconductor at random, in analogy with an atomic liquid.

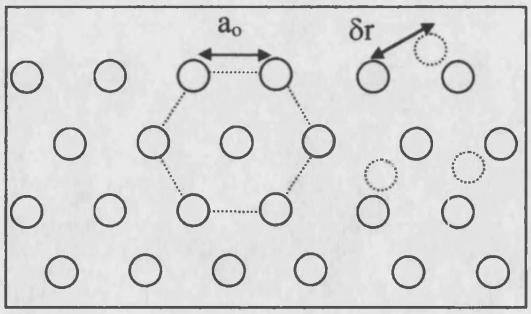

Figure 3.3. Thermal agitation of the vortex lattice.

The melting situation described above is known as Lindemann melting and the fraction $c_L=\Delta r/a_o$ (the Lindemann coefficient) is typically in the range 0.1-0.2.

Clearly, as the temperature is increased the vibrations will become larger and at some field dependent melting temperature $T_m(H)$ the ratio c_L will become greater than the critical melting ratio, at which point the lattice melts. Similarly, if the applied field is increased the vortex separation a_o will become smaller until again at some field H_m the lattice melts. It is important to note that Lindemann melting is not a microscopic theory, but simply a phenomenological picture of what is going on.

The temperature dependence of the melting field $H_m(T)$ can be found experimentally from measurements of the local magnetisation [E. Zeldov *et al.*,1995], bulk magnetisation [H. Pastoriza *et al.*,1994], neutron diffraction studies [R. Cubitt *et al.*, 1993] or muon spin relaxation (μSR) experiments [T. Blasius *et al.*, 1999]. The clearest signature is a discontinuous jump in the magnetisation, which occurs when the lattice melts, due to a change in the entropy at the transition which is related to a change in the local magnetisation through the magnetic analogue of the Clausius-Clapeyron relationship for phase transitions

$$\Delta M_t = -\frac{B}{s\mu_0\Phi_o}\frac{dT}{dH_m}\Delta S, \tag{3.2}$$

where ΔM_t is the change in local magnetisation, B is the average flux density, s the copper oxide layer separation, Φ_o the flux quantum, dT/dH_m the slope of the melting line and ΔS is the entropy change per vortex per layer on melting.

The first type of local experiment for determining the melting line is an isothermal magnetisation loop, where the phase transition is indicated by an abrupt increase in the local magnetisation as the applied field is increased. The other type of experiment is a field-cooled induction measurement, where a drop in the local induction is observed at the melting temperature as the sample is cooled. The principle difference between these experiments is that in the field-cooled experiment all barriers to vortex penetration are avoided, since the flux is already inside the sample when it becomes superconducting, whereas in the magnetisation loops surface and geometrical barriers lead to irreversibility.

The fact that the transition appears to be very sharp suggests that the melting transition is first order, and this was confirmed by Schilling *et al.*[1996] in YBCO by measuring a latent heat at the transition, which is another signature of a first order transition.

Using the Lindemann melting criterion it is possible to estimate the temperature dependence of the melting field. To simplify the theory, only a nearest neighbour approach will be used here; a more rigorous approach would require integration over an entire Fourier spectrum of fluctuations. The repulsive force between two vortices is obtained by superposing the two vortex fields:

$$h(r) = h_1(r) + h_2(r), \tag{3.3}$$

where h_1 is the field due to vortex 1 and h_2 that due to vortex 2. The field h(r) can be obtained by solving the modified London equation

$$\lambda^2 \nabla^2 h - h = \Phi_0 \, \delta_2(r) \tag{3.4}$$

to get

$$h(r) = \frac{\Phi_o}{\mu_o \lambda^2} K_o\left(\frac{r}{\lambda}\right). \tag{3.5}$$

A vortex line energy, ε_0, can be estimated in the high field limit ($\xi \ll r \ll \lambda$ and the modified Bessel function K_0 is approximated by ln(x)) and is given by

$$\varepsilon_0 = \left(\frac{\Phi_o}{\lambda\sqrt{2\mu_o}}\right)^2. \tag{3.6}$$

Now, if the vortex is displaced a distance Δr, then the change in the force between two vortices will be a restoring force δF given by

$$\delta F = \left.\frac{\partial F}{\partial r}\right|_{a_0} \delta r, \tag{3.7}$$

and the force constant $K = \left.\frac{\partial F}{\partial r}\right|_{a_0}$ can be estimated from

$$K = \left.\frac{\partial}{\partial r}\left(\frac{\partial \varepsilon_0}{\partial r}\right)\right|_{a_0} = \left(\frac{\Phi_o}{\lambda\sqrt{2\mu_o}}\right)^2 \frac{B\sqrt{3}}{2\Phi_o} \tag{3.8}$$

with a_0 the lattice constant defined by

$$a_o = \sqrt{\frac{2\Phi_o}{B\sqrt{3}}}. \tag{3.9}$$

The length of flux line displaced, L_z, is obtained by minimising the elastic displacement energy and the energy required to stretch the vortex:

$$\frac{d}{dL_z}\left(KA^2 L_z + \frac{\varepsilon_0 A^2}{L_Z}\right) = 0 \tag{3.10}$$

where A is the displacement amplitude. Hence

$$L_z = \sqrt{\frac{\varepsilon_0}{K}} = \sqrt{\frac{\Phi_o}{B}}. \tag{3.11}$$

Equating the displacement energy to the thermal energy k_BT and employing the Lindemann criterion ($A=c_La_o$ at $T=T_m$), the temperature dependence of the melting field is estimated as

$$H_m(T) \propto \left(1 - \frac{T}{T_C}\right)^2. \tag{3.12}$$

To obtain this expression, the temperature dependence of λ is required. In (3.12), the mean field approximation $\lambda^{-2}(T)=\lambda^{-2}(0)(1-T/T_C)$ was used (after Brandt [E. H. Brandt, 1995], Tinkham [M. Tinkham, 1996], and Blatter [G. Blatter *et al., 1994*]), so equation (3.12) is only valid near T_C. For a better fit, the two fluid dependence of $\lambda(T)$, given by

$$\lambda(T)=\frac{\lambda(0)}{\sqrt{1-\left(\frac{T}{T_C}\right)^4}}, \tag{3.13}$$

may be used.

The Lindemann picture of vortex solid melting assumes the vortices are three-dimensional lines, but recent work by Blatter [1996] has included the effects of electromagnetic and Josephson interactions, in the case of stacks of two-dimensional vortex pancakes. The main result of this work was the temperature dependence of the melting field, given by

$$H_m \propto \left(1-\frac{T}{T_C}\right)^{\frac{3}{2}}. \tag{3.14}$$

Both of these temperature dependencies are shown in Figure 3.4.

Alternative approaches to Lindemann melting have been suggested, with some predicting a re-entrant melting field at low fields, but this has yet to be observed experimentally. Of more experimental interest is the link between the melting field and the irreversibility line (IL), which defines the field above which magnetic hysteresis disappears. Above the IL, the vortices have enough energy to overcome all the material pinning centres and so move freely and produce a reversible B(H) loop. Below the IL, the vortices are pinned by such mechanisms as defects, crystal inhomogeneities or grain boundaries in polycrystalline materials, and so the B(H) loop exhibits strong hysteresis. It is believed that due to the finite shear modulus of the vortex solid, it is more easily pinned than a vortex liquid, so the IL is often interpreted as the melting line.

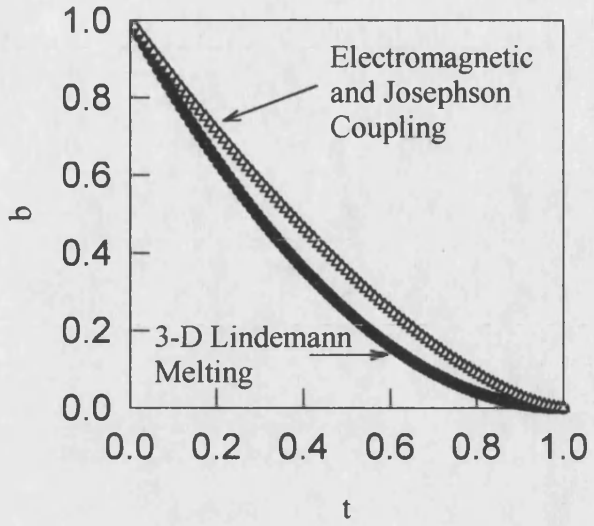

Figure 3.4. Temperature dependence of the melting field. Reduced units are $t=T/T_C$ and $b=B/(\Phi_0/\lambda^2(0))$.

This has been challenged recently, however, by Majer [D. Majer *et al.*, 1995], who showed that the IL is a result of surface pinning (Bean-Livingston barriers or Geometrical barriers) and is not related to the vortex state – indeed, they observed hysteresis in the vortex liquid regime, contrary to the simple picture described above. For this reason, the signature of melting should be taken to be ΔM, not the IL. (Also, the IL is difficult to define since it is dependent upon the sensitivity of the experiment).

3.3 Bean-Livingston Surface Barriers

An additional barrier to vortex motion across a normal-superconducting boundary was proposed by Bean and Livingston in 1964 [Bean and Livingston, 1964]. The Bean-Livingston (B-L) energy barrier is a kinetic barrier which results from the interaction between two opposing forces:

- An attractive interaction between a test vortex placed inside the superconductor and it's image vortex placed outside the superconductor (to satisfy the electromagnetic boundary conditions) which pulls vortices out.
- A repulsive force due to an interaction with the exponentially decreasing magnetic field inside the superconductor (an interaction with the Meissner screening currents) which pushes the vortices inwards.

The effect of these forces is shown schematically in Figure 3.5.

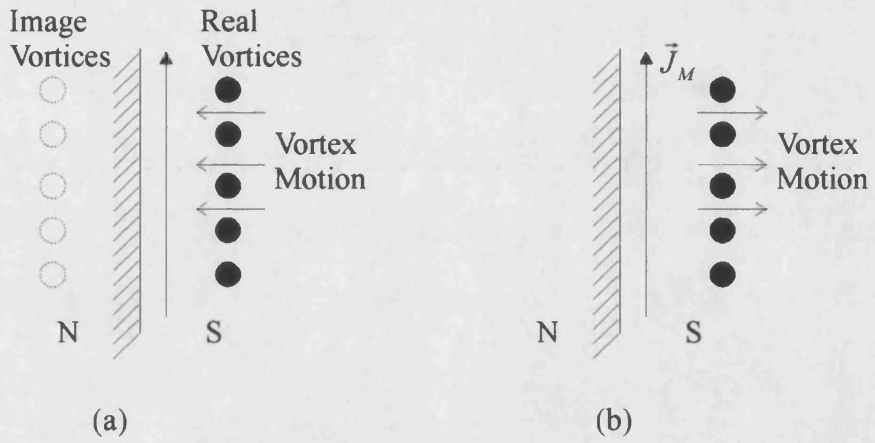

Figure 3.5. Schematic representation of the attractive interaction (a) and repulsive interaction (b) acting on a vortex near a normal (N)-superconducting (S) surface.

Although the B-L barrier is present at any normal-superconducting boundary, the effects are difficult to observe experimentally since they are frequently dominated by bulk pinning effects, or their significance is reduced through irregular surfaces. Hence B-L barriers have only been observed in very clean bulk crystals [see for example C. C. Chang and A. C Rose-Innes, 1971]. However, superconductors in the form of whiskers have very large surface-volume ratios and can be free of extended defects, making them ideal models for investigating the effects of surface pinning through B-L barriers.

Huebener [R. P. Huebener, 1979] has calculated the change in Gibbs free energy per unit length when a single test vortex is placed near a surface, due to the B-L surface barrier, and this is given by

$$\frac{\Delta G}{L} = \Phi_0 \left(H_a e^{-\frac{x}{\lambda}} - \frac{1}{\mu_0 \lambda^2} K_0 \left(\frac{2x}{\lambda} \right) - (H_a - H_{C1}) \right). \tag{3.15}$$

The first term in (3.15) is a repulsive interaction due to the Meissner screening current, the second term is an attractive interaction with the image vortices and the final term accounts for the energy of the vortex far inside the bulk of the superconductor. The variation in ΔG with distance inside the superconductor is shown in Figure 3.6, for various values of applied field, and the parameters shown.

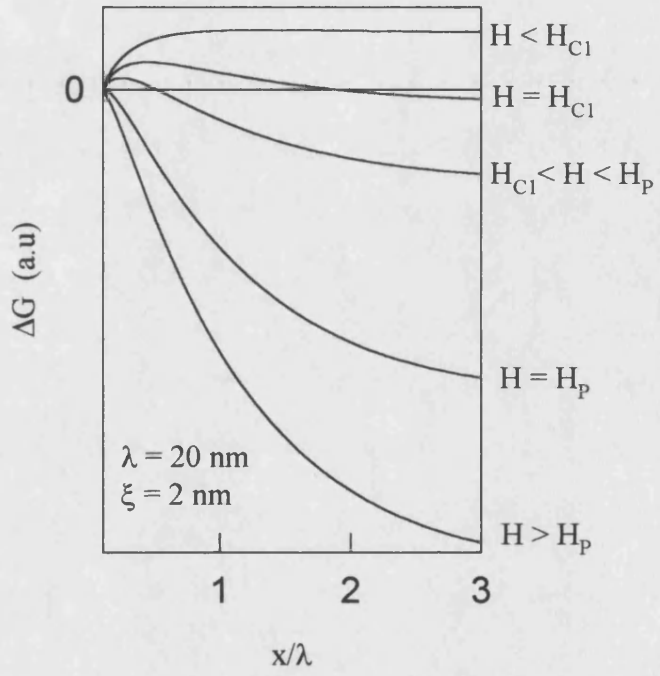

Figure 3.6. Change in Gibbs free energy for a vortex near a surface for different applied fields.

The Ginzburg-Landau expression for H_{C1}, given by

$$\vec{H}_{C1} = \frac{\Phi_0}{4\pi\mu_0\lambda^2} \ln\left(\frac{\lambda}{\xi}\right), \tag{3.16}$$

was used to determine the lower critical field.

It is clear from Figure 3.6 that for applied fields less than a critical entry field, H_P, there is a maximum in the vortex line energy somewhere inside the superconductor, which prevents vortex entry – even when the applied field has exceeded the thermodynamic lower critical field H_{C1}. The barrier does not disappear until the maximum in $\Delta G(x)$ is within a distance ξ of the superconductor surface. This allows a value for the penetration field to be determined from the condition that when $H=H_P$,

$$\left(\frac{\partial \Delta G}{\partial x}\right)_{x=\xi} = 0. \tag{3.17}$$

Using (3.15) and (3.17), the penetration field is given by

$$H_P = \frac{\Phi_0}{4\pi\mu_0\lambda\xi} \tag{3.18}$$

which is greater than the thermodynamic critical entry field by a factor of $\kappa/\ln(\kappa)$. The consequence of this barrier is that vortex penetration does not begin until the applied field exceeds H_P, which can be as much as 20 times larger than H_{C1} for the high T_C material BSCCO with $\kappa \approx 100$.

It is clear from Figure 3.6 that a vortex-free region will exist near the surface, since any entering vortex will "slide" down the energy barrier and either annihilate with it's image at the surface if $H<H_P$, or move rapidly to the centre of the superconductor if $H>H_P$ (As the vortices are pushed inwards by the Lorentz force due to the Meissner current). The main limitation of Huebener's expression is that it is based on an isotropic superconductor and assumes there are no vortices already present inside the superconductor when the test vortex is placed there.

An improvement to this model has been proposed by Clem, which takes account of vortices present inside the superconductor and allows them to relax around the test vortex [J. R. Clem, 1974]. In this model, a locally averaged magnetic flux density $\overline{b}$ is defined, which is a linear sum of the Meissner field $\mu_0 H e^{\frac{-x}{\lambda}}$, the field due to the image vortices, given by

$$\bar{b} = -\frac{B}{2} e^{-\frac{(x+x_f)}{\lambda}}, \tag{3.19}$$

and the field due the test vortex, given by

$$\bar{b} = B\left(1 - \frac{1}{2} e^{\frac{-(x-x_f)}{\lambda}}\right) \qquad x > x_f \tag{3.20a}$$

$$\bar{b} = \frac{B}{2} e^{\frac{x-x_f}{\lambda}} \qquad 0 \le x \le x_f \tag{3.20b}$$

where x_f is the width of the vortex free region. The geometry of this model assumes that a field is applied parallel to an infinite plane with a finite thickness, which has a flux density B present inside the bulk of the superconductor.

Within the vortex-free region, the local field is given approximately by

$$\bar{b} \approx B\cosh\left(\frac{x_f - x}{\lambda}\right) \tag{3.21}$$

and in the interior, $\bar{b} = B$. The width of the vortex free region, x_f, is determined by the boundary condition $\bar{b}(0) = \mu_0 H$, i.e at the superconductor boundary the local field is equal to the applied field. Using this boundary condition, x_f is given by

$$x_f = \lambda \cosh^{-1}\left(\frac{\mu_0 H}{B}\right) \tag{3.22}$$

Using these definitions, and assuming a constant B inside the interior of the superconductor, $\bar{b}(x)$ varies as shown in Figure 3.7.

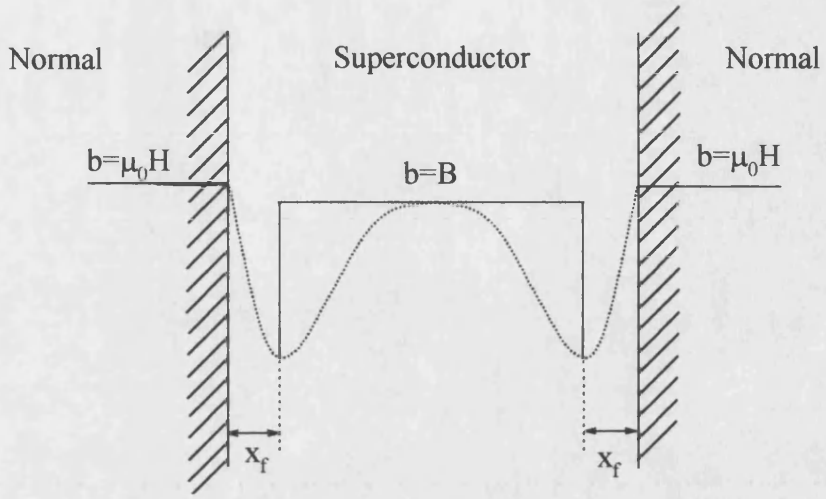

Figure 3.7. Variation in locally averaged magnetic flux density across a superconductor.

In Figure 3.7, the dotted line represents the local flux density distribution, but for the model described above the flux density is assumed to be constant in space and equal to B inside the dome region (represented by the solid line). The change in free energy of a test vortex when it enters the superconductor is given by

$$\Delta G = \Delta G_M + \Delta G_I \tag{3.23}$$

where ΔG_M describes the interaction with the Meissner current, which is given by

$$\Delta G_M = -\Phi_0 \left(H - \frac{B}{\mu_0} \cosh\left(\frac{x_f - x}{\lambda} \right) \right) \tag{3.24}$$

and ΔG_I describes the interaction with the image vortex, given by

$$\Delta G_I = \left(\frac{\Phi_0}{\sqrt{4\pi\mu_0}\lambda}\right)^2 \left[K_0\left(\frac{\xi}{\lambda}\right) - K_0\left(\frac{2x}{\lambda}\right) - 2K_0\left(\frac{x_f}{\lambda}\right) - 2K_0\left(\frac{x_f + x}{\lambda}\right)\right]. \qquad (3.25)$$

The variation of ΔG with distance from the surface is shown in Figure 3.7, for different applied fields.

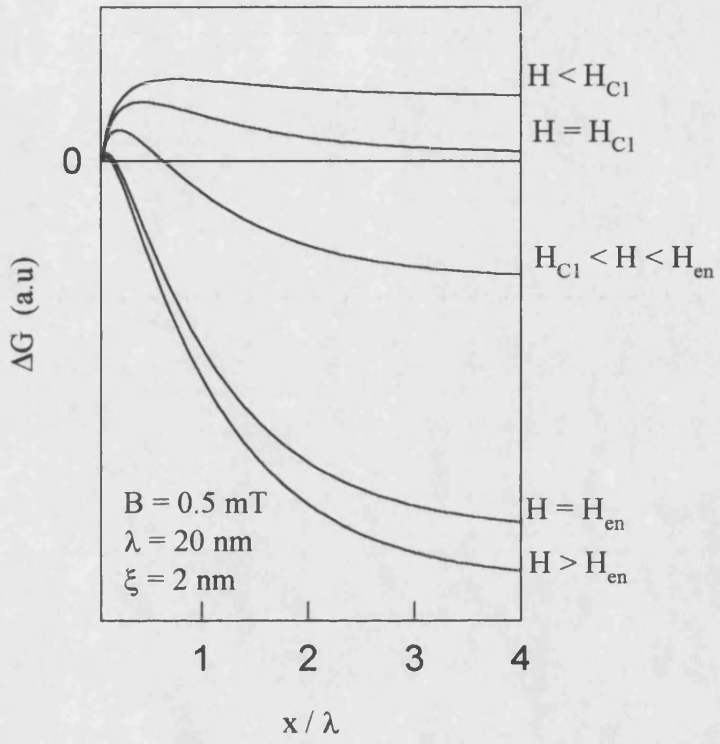

Figure 3.8. Change in Gibbs free energy for a vortex near a surface, accounting for interior vortices.

For a given interior flux density B, the maximum in ΔG reduces and occurs nearer the surface as the external field is increased from zero. When the width of the vortex free region (x_f) is large (compared with ξ), any vortices entering at the surface slide down the energy barrier and are annihilated with their image, exactly as in Huebener's model. When the maximum in ΔG occurs within a vortex core width of the surface, a vortex may enter the vortex-free region and slide down the energy barrier into the bulk of the superconductor, since the Meissner force is now

dominating the attractive image term. This first occurs when the applied field is equal to the penetration field H_{en}, which can be determined as follows.

The location of the maximum in ΔG, denoted by x_m, is determined by minimizing (3.23) and equating to zero, as in (3.26):

$$\left(\frac{\partial \Delta G}{\partial x}\right)_{x=x_m} = \frac{\Phi_0^2}{2\pi\mu_0\lambda^3}\left(K_1\left(\frac{2x_m}{\lambda}\right) - K_1\left(\frac{x_f + x_m}{\lambda}\right)\right) - \frac{\Phi_0}{\mu_0\lambda} B\sinh\left(\frac{x_f - x_m}{\lambda}\right) = 0. \tag{3.26}$$

As in Huebener's model, vortices begin to enter the superconductor when $x_m=\xi$, at the field $H=H_{en}$, but Clem's model allows for a flux density dependence, i.e. $H_{en} = H_{en}(B)$. In this situation, the vortex free region is denoted as x_{en}, and if the small argument approximation of K_1 is used and $\xi << x_{en}$, then (3.26) reduces to

$$\frac{\Phi_0^2}{2\pi\mu_0\lambda^3}\left(\frac{\lambda}{2\xi} - \frac{\lambda}{x_{en}}\right) = \frac{\Phi_0}{\mu_0\lambda} B\sinh\left(\frac{x_{en}}{\lambda}\right) \tag{3.27}$$

Using the result from Huebeners model for the penetration field when there is no flux density present (equation 3.18), and assuming that $x_{en} >> \xi$, (3.27) may be re-written as

$$B\sinh\left(\frac{x_{en}}{\lambda}\right) \cong \mu_0 H_P. \tag{3.28}$$

Finally, using the definition of x_{en} given in (3.22), we get

$$H_{en}(B) = \left(H_P^2 + \left(\frac{B}{\mu_0}\right)^2\right)^{\frac{1}{2}} \tag{3.29}$$

which describes the initial leg of the hysteresis cycle, assuming H_{en} is the applied field:

$$M = \frac{B}{\mu_0} - H = \sqrt{H^2 - H_P^2} - H \approx \frac{H_P^2}{2H} \tag{3.30}$$

As the applied field is increased above H_P, vortices enter at the surface, slide down the potential energy hill, doing work on a viscous drag force and dissipating energy. The vortices are then pushed towards the centre of the superconductor by the dominating Meissner force and accumulate at the centre, producing a dome-like flux profile. If the applied field is now reduced, the vortex-free region also reduces since vortices are prevented from leaving by the large potential barrier (See Figure 3.8 for $H>H_{en}$). However, when the applied field is equal to a critical exit field, the maximum of ΔG occurs at the edge of the vortex-free region (i.e. $x_{ex} = x_f = x_m$). The vortices are now pulled towards the surface by the image force, eventually annihilating with their image at the surface. Using the limits that $x_f = x_m$ at $H=H_{ex}$, and using (3.26), the following expression is found:

$$B = -\frac{\Phi_0}{2\pi\lambda^2} K_1'\left(\frac{2x_{ex}}{\lambda}\right) \tag{3.31}$$

and using the small argument approximation for K_1 and the definition of x_{ex} given by (2.22), the critical exit field is found to be

$$\mu_0 H_{ex}(B) \approx B + \frac{\Phi_0}{16\pi\lambda^2} \approx B, \tag{3.32}$$

leading to $B=\mu_0 H$, or $M=0$ on the return leg of the hysteresis loop.

Thus, Clem's model of pinning by a surface barrier allows a characteristic hysteresis loop to be derived for a system dominated entirely by surface barriers, and this is shown in Figure 3.9 below. Below the penetration field H_P (defined by (3.18)), there are no vortices inside the superconductor and $B=0$. Above H_P, vortices begin to enter and the curve is given by equation (3.29). If the field is now reduced, no vortices may leave the superconductor (So B remains constant at the value given by $B(H_{max})$ in

equation (3.29)) until the applied field is equal to the critical exit field, given by (3.32). At this point, vortices leave the superconductor and $B=\mu_0 H$.

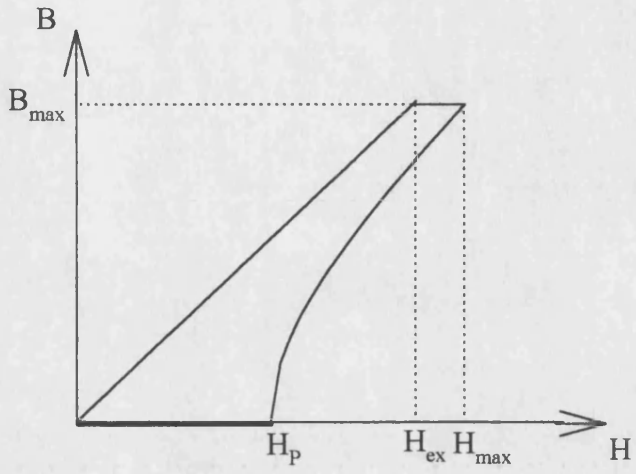

Figure 3.9. The hysteresis loop produced using Clem's model of surface pinning.

Burlachkov has used this model of vortex activation over a surface barrier to derive expressions for the temperature dependence of the penetration field in two cases [L. Burlachkov, 1994]. At low fields and high temperatures the model assumes three dimensional vortex lines are being thermally activated over the surface barrier, whereas at lower temperatures and higher fields the vortex lines are assumed to decouple into stacks of two-dimensional pancake vortices which move quasi-independently of one-another. Since the penetration field can be directly determined experimentally from hysteresis loops, Burlachkov's model may be compared with real experimental data.

The starting point for this derivation is an expression for the energy of interaction between a 2D vortex pancake, its mirror image and the Meissner current, which is given by

$$U(x) = \varepsilon_0 d \ln\left(\frac{2.94x}{\xi}\right) - \Phi_0 d\, j\, x \qquad (3.33)$$

where ε_0 is the vortex line energy per unit length, d is the inter-layer spacing (15Å in BSCCO), ξ is the coherence length, x is the distance between a vortex and it's image ($x \ll \lambda$), and j is the Meissner current density, given by the expression

$$j = \frac{H}{\lambda}. \tag{3.34}$$

As with Clem's model, the superconductor occupies a half space x>0. The maximum value of U(x), U_0 is given by

$$U_0 = \varepsilon_0 d \ln\left(\frac{1.08}{\xi} r_0\right) \tag{3.35}$$

with r_0 given by

$$r_0 = \frac{\varepsilon_0}{\Phi_0 j}. \tag{3.36}$$

Using the G-L expression for the thermodynamic critical field, (3.36) can be re-written as

$$U_0 = \varepsilon_0 d \ln\left(0.76 \frac{H_C}{H}\right). \tag{3.37}$$

Typical values of the product $\varepsilon_0 d$ for BSCCO ($\lambda_0 \approx 200$ nm and d=15 Å) give barrier heights of about 700K, which are small enough to expect magnetic relaxation, or vortex creep, over the barrier.

During a time t, thermal activation allows pancake vortices to overcome barriers of size $U(t) = k_B T \ln \frac{t}{t_0}$, where t_0 is a microscopic time scale analogous to an attempt frequency, and using (3.37) one obtains

$$H_P(T) = H_C \, e^{-\frac{T}{T_0}}, \tag{3.38}$$

where T_0 is given by

$$T_0 = \frac{\varepsilon_0 d}{k_B \ln\left(\frac{t}{t_0}\right)}. \tag{3.39}$$

Using the same values for BSCCO given above, and $\ln\frac{t}{t_0} \approx 30$, a typical value of T_0 is 23K. In this model, the weak temperature dependence of H_C and ε_0 is neglected, as are bulk pinning effects, and the exponential temperature dependence is derived in the limit of weakly coupled two-dimensional pancake vortices. In the case of strongly coupled pancakes (i.e. three-dimensional vortex lines) a temperature dependence of the form

$$H_p(T) \propto \frac{(T_C - T)^{\frac{3}{2}}}{T} \tag{3.40}$$

is predicted for vortex creep over a surface barrier. Using this model, a crossover field should be observed in $H_P(T)$, with high fields exhibiting an exponential dependence and low fields showing the dependence in (3.40), as shown in Figure 3.10 below.

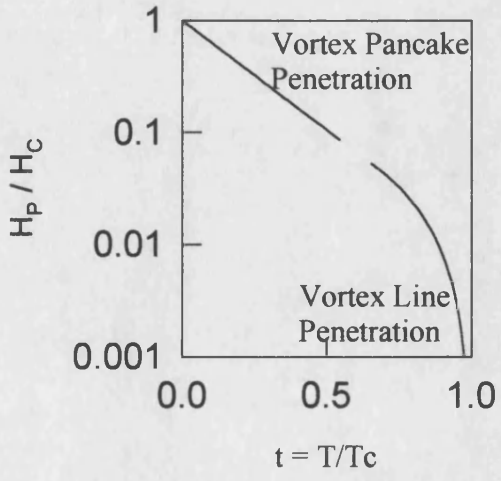

Figure 3.10. The two regimes of vortex penetration: 2-D pancakes at high fields and 3-D lines at low fields.

Since thermal activation of vortices over a surface barrier is a statistical process, significant relaxation effects are expected, particularly at temperatures near T_C. This leads to an equilibrium magnetization curve, which is reversible in the absence of any other pinning mechanisms. In a normal hysteresis loop, when the applied field is swept to a value and then held constant, the superconductor is in a metastable magnetic state, with the magnetization slowly relaxing towards the equilibrium value.

On the increasing leg of a hysteresis cycle above H_P, relaxation occurs by vortices "hopping" over the vortex free region (via thermal activation) and entering the superconductor, thereby reducing the magnetization (See figure 3.11). On the decreasing leg, the magnetization is increased by vortices leaving the superconductor, but vortex exit is opposed by a viscous drag force which acts on the vortex core as it slides down the free energy hill (See Figure 3.8). The equilibrium magnetization curve is shown in Figure 3.11, together with the metastable states obtained on the increasing (M_{en}) and decreasing (M_{ex}) hysteresis legs.

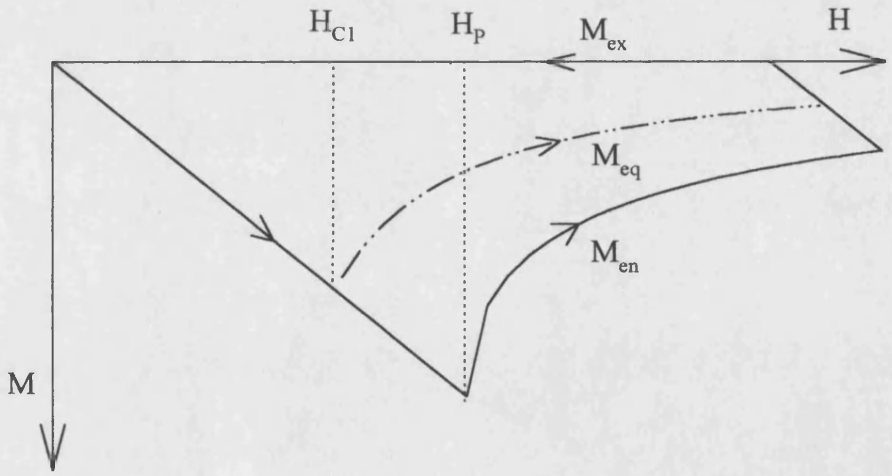

Figure 3.11. Hysteresis loop showing vortex entry (M_{en}) and exit (M_{ex}), and the equilibrium magnetization curve (M_{eq}).

A consequence of magnetic relaxation is that both the penetration field H_P and the hysteresis width ΔM (defined by $\Delta M = M_{ex} - M_{en}$) will depend on the rate at which

the external field is swept. For very slow sweep rates, the hysteresis width will be small, since the system will relax towards M_{eq}, and the penetration field will approach the thermodynamic lower critical field H_{C1}.

For vortex entry (the M_{en} leg), Burlachkov [1993] has shown that the barrier height is given by

$$U_{en} \approx \frac{\Phi_0 m_{eq} \lambda}{2\pi} \sqrt{\frac{\mu_0 H_{C1} m_{eq}}{\gamma B}} \frac{1}{\sqrt{m}}, \tag{3.41}$$

and the corresponding barrier for vortex exit is given by

$$U_{ex} \approx \frac{\Phi_0 \lambda}{2\pi} \sqrt{\frac{H_{C1}}{\gamma \mu_0 B}} m \tag{3.42}$$

where γ is the anisotropy parameter and B the internal flux density. In (3.41) and the following derivation, we have taken m=-M.

Note that the expressions for U_{en} and U_{ex} both reduce to the same barrier height when $m=m_{eq}$, thereby showing that the equilibrium curve is not hysteretic.
The relaxation curves (given by $m_{en}(t)$ and $m_{ex}(t)$) can be obtained in the following way. Vortices may be thermally activated over the barrier in a time t according to

$$\frac{1}{t} = \frac{1}{t_0} e^{-\frac{U}{kT}} \tag{3.43}$$

where $1/t_0$ is an attempt frequency. Substituting this into (3.41) and (3.42) yields the following expressions for vortex relaxation in and out respectively:

$$\ln\left(\frac{t}{t_0}\right) \approx \frac{\Phi_0 m_{eq} \lambda}{2\pi kT} \sqrt{\frac{H_{C1} m_{eq}}{\gamma \mu_0 B}} \frac{1}{\sqrt{m_{en}}} \tag{3.44}$$

$$\ln\left(\frac{t}{t_0}\right) \approx \frac{\Phi_0 \lambda}{2\pi kT} \sqrt{\frac{H_{C1}}{\gamma \mu_0 B}} m_{ex}. \tag{3.45}$$

Equations (3.44) and (3.45) give very asymmetric relaxation curves, as shown in Figure 3.12, with vortex exit proportional to the magnetization and vortex entry a non-linear function of magnetization.

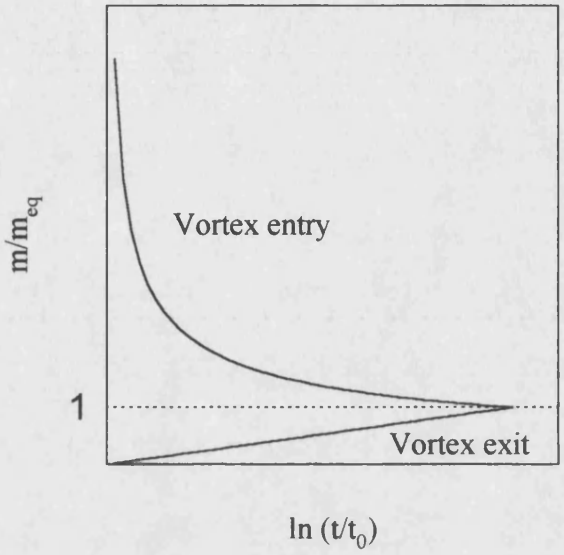

Figure 3.12. Asymmetric relaxation curves predicted for relaxation over a B-L surface barrier.

The rate of vortex exit is given by

$$R_{ex} = \frac{d\,m}{d\ln(t)} = \frac{2}{\Phi_0\sqrt{\pi}\lambda}\sqrt{\frac{\gamma B(0)}{H_{C1}}}kT\,, \tag{3.46}$$

and is dependent on both the temperature, and the initial flux density, but is independent of the magnetization. The temperature dependence is a result of the fact that higher temperatures lead to greater thermal energies and hence faster vortex motion. The dependence on B, however, means that R_{ex} will depend on the location within the superconductor: assuming the dome-shaped profile described earlier, the vortex exit rate will be larger near the centre and smaller near the edge.

For vortex entry, the rate is given by

$$R_{en} = \frac{dm}{d\ln(t)} = -\frac{2\sqrt{\pi}}{\Phi_0 \lambda}\sqrt{\frac{\gamma B(0)}{H_{c1}}}\left(\frac{m_{en}}{m_{eq}}\right)^{\frac{3}{2}} k_B T \qquad (3.47)$$

The linear temperature dependence is still present, but the vortex entry rate is proportional to $m^{3/2}$, as opposed to vortex exit, which is independent of m.

3.4 Geometrical Barriers

The Bean-Livingston barriers described earlier were constructed for a field applied parallel to the surface of a semi-infinite sample, which is a rather contrived geometry. Real HTSC samples tend to have a platelet geometry with the field usually applied normal to the larger surface, which is a much more complicated geometry. Clearly, there is still an image vortex outside the superconductor (as in the B-L barriers), but now the finite sample thickness must be taken into account.

To set the magnetic induction to zero inside the superconductor, Meissner screening currents are induced, which flow around the perimeter of the sample. The direction and magnitude of these currents is such that if a vortex enters near the edge, the Lorentz force pushes it towards the centre. A force due to the line tension of the vortex, which tries to prevent vortex entry, balances this effect. As the applied field is increased from zero, the vortex begins to penetrate at the corners of the sample, where the *local* field is greater than the penetration field, H_P (the field at which the vortices overcome the geometrical barrier). As the field is increased, the vortex penetrates further into the sample until the two vortex segments meet at the sample equator, the line tension is at a maximum and the Lorentz force is unopposed so the vortex moves rapidly to the sample centre. Figure 3.13 shows the two extremes of this situation. In figure 3.13 (a) the line tension is small and the vortex has only just started to penetrate at the corners of the sample, where the average field is enhanced by geometrical effects. The situation in Figure 3.13 (b) is very different; the line tension is at a maximum and the vortex has penetrated as far as possible without complete penetration. In this case the applied field is almost equal to the penetration field H_P. When the field is increased further, the vortex will penetrate into the sample and be swept to the centre by the Lorentz force due to the Meissner screening currents.

An estimate of the height of the geometrical barrier can be obtained by taking the difference between the maximum and minimum line energies. The situation with maximum line energy is shown in Figure 3.13 (b).

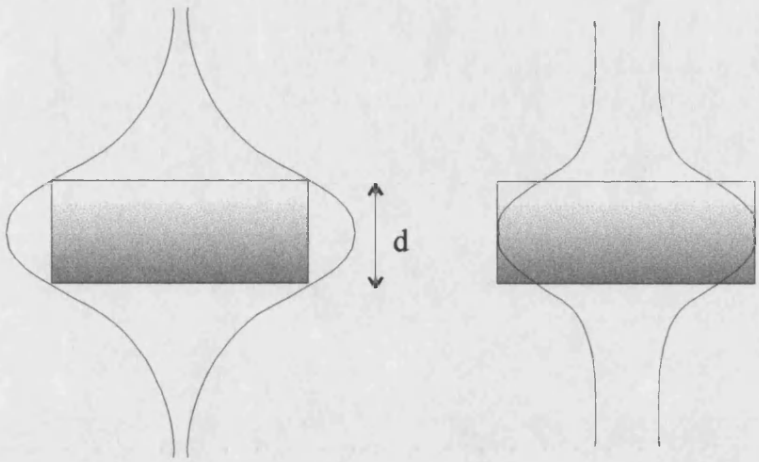

(a) (b)

Figure 3.13. The two extremes of vortex penetration.

The minimum line energy configuration is when the vortex has penetrated and goes straight through the superconductor with no bends. The vortex line tension per unit length (ε_o) is given by

$$\varepsilon_0 = \left(\frac{\Phi_0}{\sqrt{4\pi\mu_0}\lambda} \right)^2 \tag{3.48}$$

where, for the minimum energy, the relevant length is the sample thickness d. For the maximum energy situation the relevant length is an arc of a circle of diameter d, as shown by Kuznetsov [Kuznetsov *et al.*, 1997]. So the total height of the geometrical barrier E_g is estimated as

$$E_g = \varepsilon_o \pi \frac{d}{2} - \varepsilon_o d = \varepsilon_o d\left(\frac{\pi}{2} - 1 \right). \tag{3.49}$$

Using typical values for BSCCO of $\lambda=10^{-7}$ m and $d=10^{-4}$ m, and substituting in the flux quantum $\Phi_o=2.08\times10^{-15}$ Wb, the barrier has a height of 2×10^{8} K, which is extremely large. The height of this barrier precludes any significant thermal activation over the geometrical barrier or any relaxation effects, in stark contrast to the strong relaxation effects predicted for Bean-Livingston surface barriers.

Zeldov [1994b] has calculated both the local induction profile and the current distribution due to the Meissner screening currents. The flux profile, shown in Figure 3.14 (a) confirms that the sample is in a true Meissner state with zero induction inside the sample and decays to the applied field far outside it.

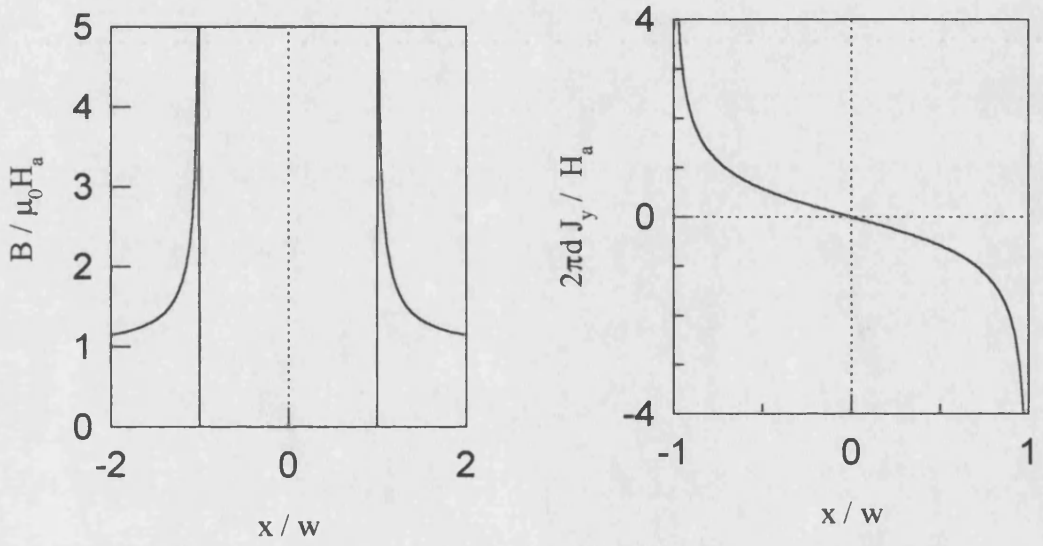

(a) (b)

Figure 3.14. The magnetic flux profile (a) and current density distribution (b) in a sample of width 2W in an applied field H_a, calculated from equations given by Zeldov *et al.*, [1994b].

The current distribution shown in Figure 3.14 (b) shows that the screening currents flow mainly at the superconductor edges. Far from the sample edges, the position dependence of the vortex line energy can be approximated by

$$\varepsilon(x) \approx \varepsilon_o - \frac{2\Phi_o H_a}{d}\sqrt{w^2 - x^2}\,, \tag{3.50}$$

which leads to the bowl-shaped profile shown in Figure 3.15 with a minimum at the sample centre, arising from the Lorentz force pushing the vortices inwards, as described above.

When the applied field exceeds the penetration field, it becomes energetically favourable for vortices to nucleate at the edges (the maximum line tension can be achieved and the geometrical barrier is effectively overcome) and then rapidly move inwards. This leads to an accumulation of flux at the centre of the superconductor and a dome-shaped profile, as calculated by Zeldov [1994b].

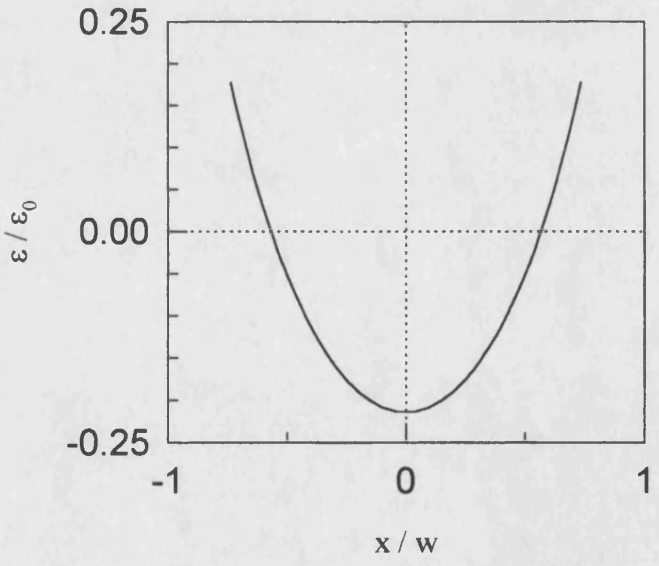

Figure 3.15. Spatial dependence of the vortex line energy, showing the bowl-shaped profile.

3.5 Interaction Between Surface Barriers and Vortex-Vortex Repulsion

In a superconductor with one very small dimension (on the order of λ), vortex motion will be dominated by surface barriers, which push them towards the centre of the sample. This force is balanced by the inter-vortex repulsion, which is trying to keep the vortices far apart and therefore spread evenly around the sample. Hence, as both the surface barrier and the vortex-vortex interactions are field dependent, the vortex lattice structure should change considerably as a function of applied field.

Mawatari *et al.*[1994] investigated the possible flux structures in a thin film with a field applied parallel to it and an applied transport current. In this geometry, surface barriers should be very strong and their work predicted discrete minima in the field dependence of the critical current of the film. The fields at which these minima occurred were termed matching fields, B_N, and were shown to originate from changes in the vortex structure inside the film. Above the penetration field, the vortices arrange into one parallel row, due to the influence of the surface barriers pushing them inwards. As the field is increased further the row becomes more densely packed as more vortices enter, and thus the row becomes less stable as the repulsive vortex interaction becomes stronger and eventually the row becomes energetically unstable and splits into two less densely packed parallel rows. The field at which this occurs is termed the first matching field, B_1, and as the applied field is increased further the above process is repeated and the two rows split into 3 rows at the second matching field B_2. This process is repeated until the vortex cores overlap at H_{C2} and the sample becomes normal.

The flux structures shown in Figure 3.16 were obtained by minimising the change in Gibbs free energy associated with the presence of the vortices (after Mawatari, 1994) and finding the equilibrium positions of the vortices. This method will now be reviewed. The geometry is shown in Figure 3.17, and consists of a thin film of an isotropic superconductor (e.g. Nb) of thickness d and infinite dimensions in the y-z plane. A magnetic field is applied in the z-direction, and a transport current flows in the positive y direction. The other limitations to the theory are that the film is thinner than the penetration depth λ and much larger than the coherence length ξ so

that the Ginzburg-Landau parameter is very large and the London limit can be applied. It is also assumed that there is no pinning other than that due to the surface barriers.

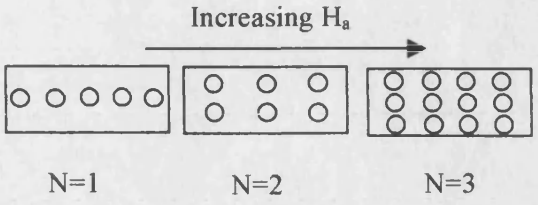

Figure 3.16. The first three matching fields in a system with no bulk pinning

In these limits, the London equation can be used to determine the spatial dependence of the magnetic field B(x,y) in the x-y plane:

$$\lambda^2 \nabla^2 B - B = \Phi_o \sum_i \delta(x - x_i)\delta(y - y_i) \tag{3.51}$$

here (x_i,y_i) is the position of the i^{th} vortex core and δ is a delta function. λ and Φ_o are the usual penetration depth and flux quantum.

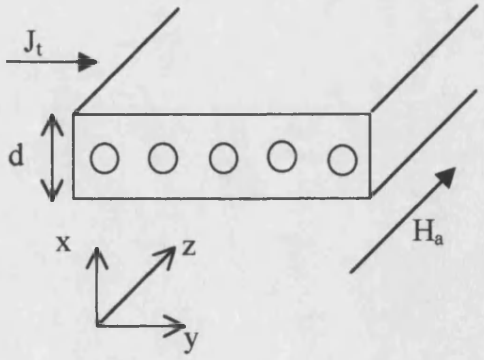

Figure 3.17. Geometry used in the matching field model.

The London equation is solved subject to the boundary conditions that the field at the top and bottom of the film is equal to the applied field B_a plus the field due to the transport current:

$$B = B_a + \mu_o J_t \frac{d}{2} \qquad x = 0 \tag{3.52 a}$$

$$B = B_a - \mu_o J_t \frac{d}{2} \qquad x = d \tag{3.52 b}$$

The solution of the London equation subject to these boundary conditions is given by

$$B(x,y) = B_m(x) + B_v(x,y), \tag{3.53}$$

where B_m is the field due to the Meissner screening current, given by

$$B_m(x) = B_C\left[1 - \frac{dx}{2\lambda^2}\left(1 - \frac{x}{d}\right)\right] - \mu_o d J_t\left(\frac{x}{d} - \frac{1}{2}\right), \tag{3.54}$$

and B_V is the field due to the vortex currents, and is given by

$$B_V(x,y) = \frac{\Phi_o}{2\pi\lambda^2}\frac{2\pi d}{a_r}\left[\frac{x + x_i}{2d} - \frac{|x - x_i|}{2d} - \frac{x \cdot x_i}{d^2}\right]. \tag{3.55}$$

B_C is the thermodynamic critical field and a_r the vortex spacing. The positions of the vortices are found by minimising the Gibbs free energy, given by

$$\Delta G = \frac{\Phi_o}{\mu_o}\sum_i [B_m(x_i) - B_a + B_V(x_i, y_i)]. \tag{3.56}$$

For N parallel rows of vortices, the minimisation of (3.56), together with the expressions for B_M and B_V lead to three equations in three unknowns:

$$B_a a_x a_y = \Phi_o \tag{3.57}$$

$$J_t = \frac{B_a d}{2\mu_o \lambda^2}\left(1-\frac{N a_x}{d}\right)\left(\frac{2\bar{x}}{d}-1\right) \tag{3.58}$$

$$\left(\frac{2\bar{x}}{d}-1\right)^2 = \left(\frac{a_x}{2}\right)^2 - \left(1-\frac{N a_x}{d}\right)^2 - \frac{8\pi a_x}{a_y}\left[1+\ln\left(\frac{\sqrt{2}\pi\xi}{a_y}\right)\right] \tag{3.59}$$

Equations (3.57)-(3.59) are solved for a_x, a_y (as shown in Figure 3.18) and $\bar{x}$ - the x spacing, y spacing and averaged position of the vortex row, respectively.

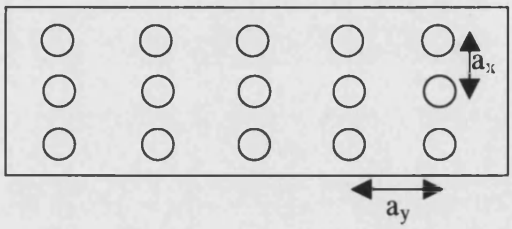

Figure 3.18. The x and y spacing of the vortex structure.

These parameters are then used to calculate the increase in Gibbs free energy due to the flux structure, given by

$$\Delta G = \frac{N\Phi_o^2}{4\pi\lambda^2 d a_y}\left[1-2\pi N\frac{\bar{x}(d-\bar{x})}{d a_y}+\frac{\pi}{3}(N^2-1)\frac{a_x}{a_y}\right] \tag{3.60}$$

Figure 3.19 shows the change in Gibbs free energy for values of N from 1 to 6. At each crossover point, there will be a change from a state with N rows to a state with N+1 rows, indicated by a matching field. The system will always try to be in the state with the lowest energy.

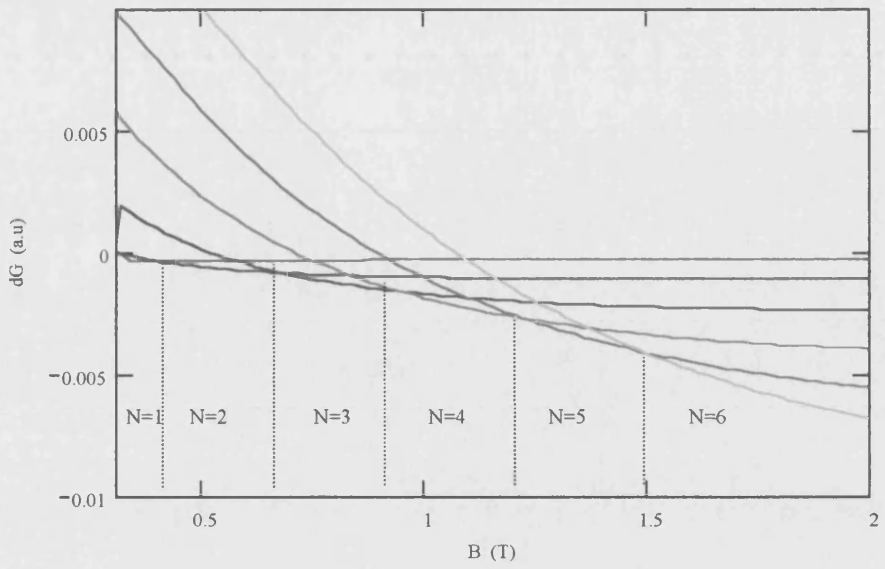

Figure 3.19. Change in the Gibbs free energy for a system with N rows of vortices (N= 1 to 6) as a function of applied field, plotted from equations derived by Mawatari [1994].

This matching field structure has been observed experimentally by Zeise *et al.* [1996] in thin films of Bi (2212), and YBCO (123), where they are indicated by distinct dissipation maxima in vibrating reed experiments. The matching fields should also be observed in local magnetic measurements, such as miniature Hall probe sensors, where they should cause jumps in the local magnetic induction when an N row system switches to an N+1 row system as the applied field is increased. The jumps described above are localised effects, and would not be observed in a bulk magnetisation measurement, since $B\, a_x\, a_y = \Phi_0$ is independent of N.

Chapter 4

The BSCCO High T_C Superconductors

4.1 Discovery and Structural Analysis of BSCCO

In 1988, Maeda *et al.* reported that a compound of Bismuth, Strontium, Calcium and Copper became superconducting at a temperature of 105K [Maeda, 1988]. Further work by Hazen *et al.* [Hazen *et al.*, 1988] confirmed this result, and also established that there are three superconducting phases in this compound, with very different critical temperatures, as shown in Table 4.1.

Phase	Acronym	T_C (K)
$Bi_2Sr_2Cu_2O_{6+\delta}$	Bi2202	10
$Bi_2Sr_2CaCu_2O_{8+\delta}$	Bi2212	94
$Bi_2Sr_2Ca_2Cu_3O_{10+\delta}$	Bi2223	110

Table 4.1. The three phases of BSCCO.

As with all the high T_C cuprates, BSCCO has a highly anisotropic perovskite crystal structure, with the superconductivity residing almost entirely within the copper-oxide planes. The structures of the three superconducting phases of BSCCO are shown in Figure 4.1, with the copper-oxide planes separated by sheets of BiO.

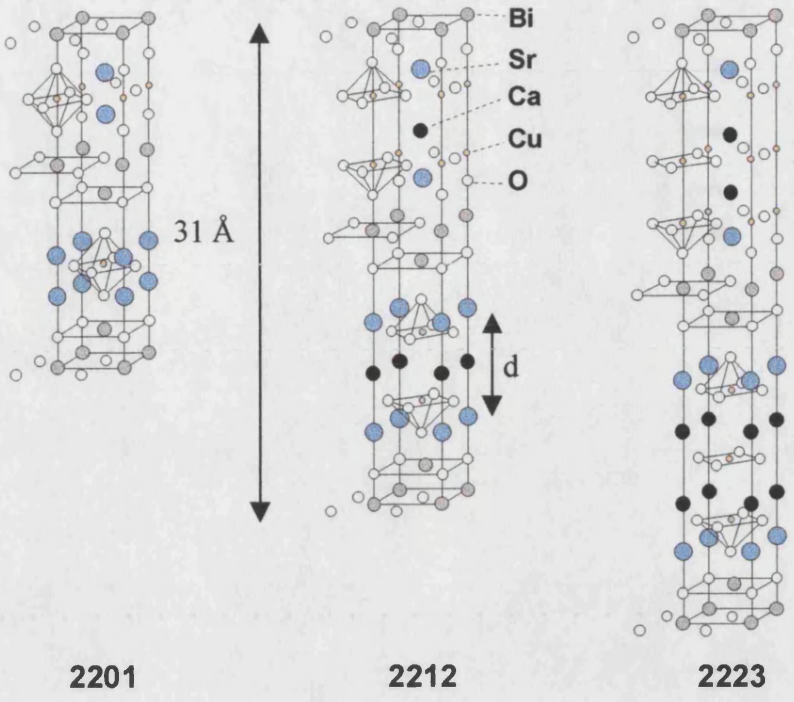

Figure 4.1. Crystal structure of the three superconducting phases of BSCCO.

Single crystal growth is a very complicated procedure and is beyond the scope of this thesis, but many papers on the subject can be found in the literature (See for example Motohira [1989], Li [1994] or Li [1994b]). Alternatives to large, bulk single crystals are BSCCO whiskers, and details on the growth of these are given in the following chapter. Whichever method is used for crystal growth, subsequent heat treatments and oxygenation procedures are required to obtain the correct oxygen stochiometry. As shown by Li *et al.*, [1994b], the exact value of the critical temperature depends strongly on the oxygen doping level, with T_C reaching a maximum value of 94K for the 2212 phase with optimum doping levels.

4.2 Determination of λ and ξ

The fundamental magnetic properties of any superconductor are the penetration depth λ and the coherence length ξ, and it is important to have an accurate measurement of these parameters before any theoretical models can be applied to real superconductors. Both λ and ξ can, in principle, be obtained indirectly from

magnetisation data through the Ginzburg-Landau expressions for the lower and upper critical fields, given by

$$\vec{H}_{C1} = \frac{\vec{\Phi}_0}{4\pi\mu_0\lambda^2}\ln\left(\kappa + \frac{1}{2}\right) \tag{4.1}$$

$$\vec{H}_{C2} = \frac{\vec{\Phi}_0}{2\pi\mu_0\xi^2}. \tag{4.2}$$

However, there are several problems with this method of determining λ and ξ. First, unless the superconductor being measured has a long, thin ellipsoidal geometry, demagnetisation effects will cause large errors in the determination of $\vec{H}_{C1}$. Secondly, when (4.1) and (4.2) are applied to the high temperature superconductors, they must be amended to account for the extreme anisotropy of these materials. The modified expressions are given by [Waldram, 1996]

$$\vec{H}_{C1}^{C} = \frac{\vec{\Phi}_0}{4\pi\mu_0\lambda_{ab}^2}\ln\kappa \tag{4.3}$$

$$\vec{H}_{C1}^{ab} = \frac{\vec{\Phi}_0}{4\pi\mu_0\lambda_{ab}\lambda_c}\ln\left(\frac{\lambda_{ab}}{d} + 1.12\right) \tag{4.4}$$

$$\vec{H}_{C2}^{C} = \frac{\vec{\Phi}_0}{2\pi\mu_0\xi_{ab}^2} \tag{4.5}$$

$$\vec{H}_{C2}^{ab} = \frac{\vec{\Phi}_0}{2\pi\mu_0\xi_{ab}\xi_c}. \tag{4.6}$$

In these expressions (4.3 to 4.6) *ab* and *c* denote directions parallel and normal to the copper-oxide planes respectively, and d is the distance between CuO planes (15Å). The third problem is a result of the large thermal energies involved with the high T_C materials, which effectively smear out the normal-superconducting transition at $\vec{H}_{C2}$

because of fluctuations in the order parameter. Coupled with the fact that $\vec{H}_{C2}(0)$ has been found to be larger than experimentally attainable magnetic fields, this is not an accurate way of determining ξ. Another problem with determining $\vec{H}_{C1}$ is the effect of surface barriers, which can significantly increase the field of first flux penetration to values larger than the thermodynamic value of $\vec{H}_{C1}$.

Techniques for the determination of λ include microwave studies [T. Jacobs *et al.*, 1995], muon spin rotation (μSR) [C. M. Aegeter *et al.*, 1996] studies, direct imaging of vortices using scanning Hall probe microscopy (SHPM) and magnetisation measurements that avoid surface barrier effects by using very slow sweep rates for the applied fields [Nideröst *et al.*, 1998]. The results from some of these experiments are shown in Table 4.2 below.

Method	$\lambda_{ab}(0)$ (nm)	$\lambda_c(0)$ (nm)
μSR	180	-
Microwave	260	4000
Magnetisation	270	1500

Table 4.2. Determination of the penetration depth at T=0K using different methods.

Determination of ξ presents a significant experimental problem in BSCCO because of fluctuations near $\vec{H}_{C2}$. However, Tinkham [1996] suggests $\xi_{ab}(0)\approx 20$Å as a representative value for most of the layered superconductors, based on measurements of $\xi_{ab}(T)$ for YBCO.

4.3 The Magnetic Phase Diagram of BSCCO

In addition to the thermodynamic transition lines $\vec{H}_{C1}(T)$ and $\vec{H}_{C2}(T)$ in the H-T phase diagram of BSCCO, several other phases have been suggested, which are delineated by additional transition lines. These include a solid melting line, $\vec{H}_m(T)$, an irreversibility line $\vec{H}_{irr}(T)$ and a crossover line $\vec{H}_{cr}(T)$ [Aegeter, 1996]. There is also some evidence for additional regimes such as a two-stage melting transition (See for example, T. Blasius [1999], or C. D. Keener [1997]) and a surface-barrier regime in the vortex liquid region [D. Fuchs, 1998]. Some of these lines are shown schematically in Figure 4.2 below with the evidence described later.

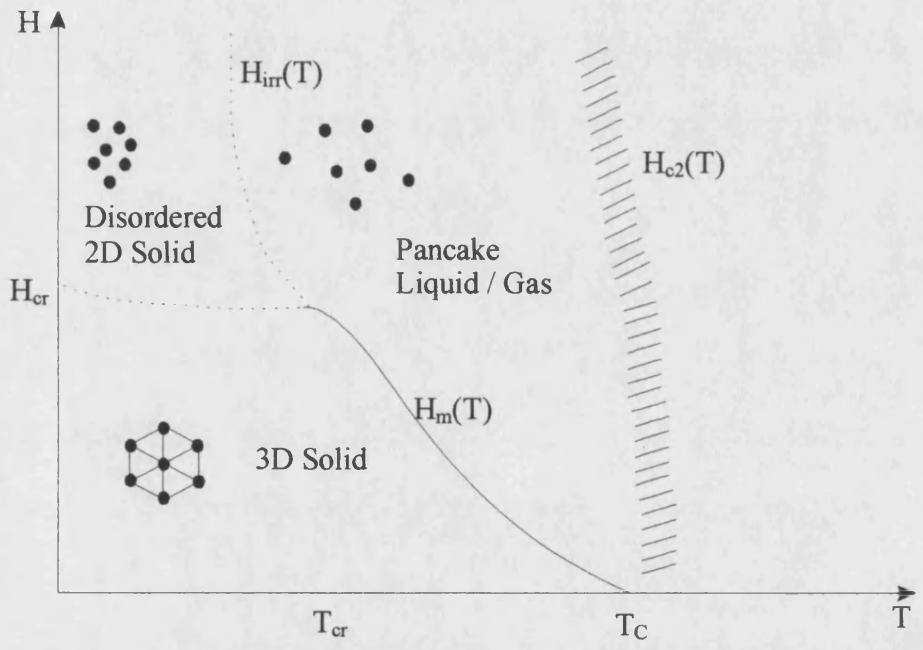

Figure 4.2. Generic phase diagram for BSCCO, showing the different possible vortex phases within the mixed state.

The first line to be added to the phase diagram was the irreversibility line, $H_{irr}(T)$, which defines the magnetic field above which the hysteresis is reversible. The standard interpretation of this line is that it marks the onset of bulk pinning, with the vortices pinned to pinning sites below the irreversibility line and free to move (and hence produce reversible magnetisation loops) at fields greater than $H_{irr}(T)$. It is now

widely believed that since a vortex solid is pinned more efficiently than a vortex liquid, the irreversibility field is coincident with the melting line $H_m(T)$. However, there are several problems with this interpretation. First, the irreversibility field is very difficult to identify experimentally since it depends on the precision of the measurement apparatus and the criterion used. Secondly, it does not account for the possibility of an unpinned lattice, which could become depinned and move as a single entity even below the melting line, leading to a reversible vortex solid. Conversely, mechanisms other than bulk pinning (such as surface barriers) may lead to vortices becoming pinned even in the liquid regime. Conclusive evidence that the irreversibility and melting lines need not coincide was given by Majer *et al.* [1995], when a step in the local magnetisation (which is associated with lattice melting) was observed deep inside the irreversible region of the hysteresis loop.

Vortex lattice melting was first reported by Gammel [1988] and Bishop [1992] using torque magnetometry measurements on single crystals of YBCO and BSCCO respectively. A sharp, discontinuous step was observed when either the applied field or temperature was swept across the transition line. Vortex lattice melting is analogous to melting in an atomic crystal, with the liquid regime exhibiting no long-range order and zero shear modulus, and the solid regime exhibiting a finite shear modulus and long-range order – in the case of the vortex solid a six-fold symmetry is obtained. Subsequent experiments with other techniques (such as μSR [Lee, 1995] or SANS [Cubitt, 1993]) have confirmed the melting interpretation, including the existence of a critical point at about 40K, below which no first order transition is observed [Zeldov, 1995].

Below the critical point it was found that the end of the melting line coincides with the beginning of a second peak line (T_{cr} in Figure 4.2) [Khaykovich, 1996]. This line is interpreted as a decoupling line above which the vortex lines decouple into a stack of weakly correlated 2D pancake vortices. Evidence of the second peak has been obtained with local Hall probe [Khaykovich, 1996] and bulk magnetisation measurements [Yang, 1993], which exhibit an increase in the magnetisation at the peak field followed by decreasing magnetisation. The peak effect is interpreted as vortex decoupling because 2D pancakes can accommodate better to the pinning landscape than 3D lines, leading to an enhanced hysteresis width at the crossover field. The peak field is almost independent of temperature and is often called the

crossover field H_{cr}, and this interpretation has been confirmed by μSR studies [Blasius, 1999].

By using different oxygen doping levels, Kaykovitch *et al.* [1996] demonstrated that the melting line shifts in the H-T plane by the same amount as the crossover field. This indicates that the second peak line may well be a continuation of the melting line below a depinning temperature T_{dp}, which is the temperature at which the critical point occurs. Kaykovitch *et al.* further suggest that the melting line is also a decoupling line, with vortex pancakes in the upper field regime and vortex lines in the lower field regime. There is also evidence of a depinning line at high fields, which terminates at the critical point and may coincide with the irreversibility line at high fields.

In the absence of surface barrier effects, the transition lines described above show the existence of at least three vortex regimes within the mixed state of BSCCO. At low fields and temperatures, a reasonably ordered 3D solid is obtained, exhibiting six-fold symmetry, long range order and a finite shear modulus. As the applied field is increased, the 3D lines decouple into 2D pancakes at the crossover field H_{cr}. Since the pancakes are more easily pinned than the lines, a disordered vortex pancake state is achieved, which has no long-range order but still retains a finite shear modulus. Above the melting line, the vortex lines melt and may simultaneously decouple into pancakes, leading to a pancake liquid/gas regime which has zero shear modulus and no long-range order or symmetry.

As mentioned earlier, surface barriers create an additional source of hysteresis not connected with bulk pinning, and in a very clean (i.e. few pinning centres) crystal can lead to a separation of the melting and irreversibility lines. Also, very strong pinning centres introduced by heavy ion irradiation can alter the phase diagram, producing a 3D, disordered solid (also known as a Bragg glass) in the low field and temperature region [Khaykovich, 1997, Ryu *et al.*, 1996].

It should be noted that the phase diagram described here is still the subject of much research and is by no means definitive. For example, a recent paper by Blasius *et al.* [1999] suggests a two-stage melting transition, with the vortex solid first melting, and then decoupling, as the temperature is increased. There has also been much theoretical work on possible re-entrant melting fields near $\vec{H}_{C1}$, but these have not yet been observed experimentally in BSCCO.

Chapter 5

BSCCO Whiskers

5.1 What are Whiskers?

Whiskers are long, thin pine needle shaped single crystals, which can have very few extended defects [Kraak *et al.*, 1996], smooth faces, and large aspect ratios (typically > 50:1). In the case of BSCCO whiskers the long side is parallel to the crystallographic $\vec{a}$ axis, the width parallel to the $\vec{b}$ axis and the $\vec{c}$ axis is normal to the thin whisker plane, as shown in Figure 5.1 below.

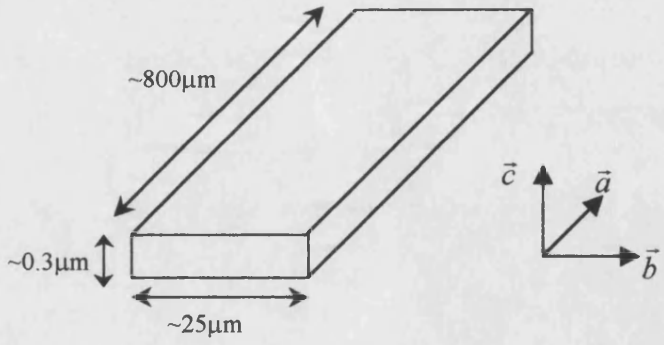

Figure 5.1. The crystallographic directions of a BSCCO whisker, together with typical dimensions.

The small dimensions and specific growth mechanism (described in the next section) are what give the whiskers greater crystalline perfection than large, bulk crystals, and make them ideal for investigating the role played by surfaces in their

superconducting properties. From an applications point of view, the single-crystal nature of whiskers leads to a much-enhanced value of critical current density due to the absence of grain boundaries, which reduce the critical current density in bulk polycrystalline materials. Also, their exceptional elastic properties give whiskers great potential.

5.2 Whisker Growth Mechanism

Several models to explain the growth of BSCCO whiskers have been proposed by different workers, and the three principle ones will be described below.

The first model was first proposed by Wagner and Ellis [1964] to explain the growth of Si whiskers, but may be applied to any crystals which grow in the same way. In this model, the whisker grows by precipitation of the growth materials in vapour form at the interface between a supersaturated liquid droplet and the surrounding solid growth plate, leading to growth from the tip of the whisker. The second model suggests a spiral growth mechanism, with whisker growth occurring along the core of a screw dislocation in the growth plate [Eshelby, 1953]. The growth material diffuses along the core to the whisker tip, again leading to a tip growth site. The final model, suggested by Matsubara *et al.*, [1996] proposes that growth takes place at the base of the whisker, with the growth material provided by a melt at the base of the whisker, and this is known as a self-top-seeding model.

Evidence for both the spiral growth mechanism and the self-top-seeding mechanism has been published. Matsubara *et al.* [1996] used in-situ observation of whisker growth to show that whiskers grow from the base. However, Jin *et al.* [1997] point to a white powder (later determined to contain Bi, Ca, Sr and Cu) deposited on the furnace tube as evidence that the constituent atoms evaporated, suggesting a vapour-growth mechanism. Also, a pointed end on the whiskers is consistent with whisker growth along a dislocation line. This also explains the large aspect ratio, since the axial direction is the fastest growth direction. The SEM image in Figure 4.2 shows the pointed tip of a whisker (and its reflection) obtained during growth studies carried out in this work, and a white deposit was also observed on the furnace tube.

The actual growth mechanism may be a combination of these models, with the whisker growth beginning along a dislocation line, but the growth material provided

by a vapour. This hypothesis is supported by Matsubara, who observed that whisker growth ceases when the oxygen flow is stopped, and resumes when the oxygen flow is resumed [Matsubara, 1996]. This suggests that oxygen flow is necessary for the transport of the vapour phase growth material. In all the models of whisker growth, experiments have shown that three components are vital. The first is a flowing oxygen atmosphere, the second is a small temperature gradient within the furnace, and the third is an amorphous, glassy growth precursor plate.

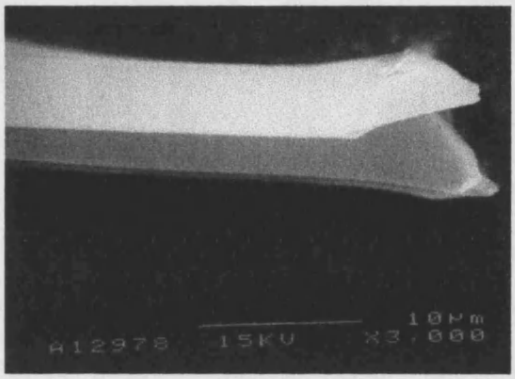

Figure 5.2. SEM image of the tip of a whisker, with the pointed shape suggesting growth along a screw dislocation.

The oxygen atmosphere is necessary for two reasons. First, the whiskers need to have the correct oxygen doping to be superconducting, and second, a flow is necessary for growth material transport. The temperature gradient allows whisker growth by diffusion: when the growth plates are heated, the atoms in the higher temperature region evaporate and are carried along by the flowing oxygen. They then condense on a growth step in the lower temperature region and begin the whisker growth. Evidence of this was observed during whisker growth carried out for this work: Firstly, long growth plates had preferential whisker growth at one end, and secondly, whisker growth was principally along the length of the axial furnace – parallel to the temperature gradient present.

Optimum growth conditions do not appear to be universal among different research groups, but a consensus seems to be a temperature gradient between 0.5 and 6.0 $^{\circ}C$ cm^{-1}, an oxygen flow rate of about 150 ml min^{-1} and annealing temperatures in the range 820 –870 $^{\circ}C$.

5.3 Whisker Growth Details

Whiskers of the 2212 phase of BSCCO have been grown at Bath, using a melt-quench technique suggested by Matsubara *et al.* [1996], and subsequently reproduced by other groups. The melt-quench technique involves two principle steps: preparation of the glassy growth plates, and growth of the whiskers using appropriate heat treatments.

The growth plates were produced in the following way. First, the powder precursors, which were Bi_2O_3, $SrCO_3$, $CaCO_3$ and CuO, were mixed in the stochiometric ratio (2:1.9:2.2:4) to produce a total of 50g of material. The mixture was then placed in a ball mill and some acetone added to produce a smooth paste, which was then ground for 2 hours. After grinding, the mixture was placed in a fume cupboard to allow the acetone to evaporate, after which the mixture was sieved through a 100μm sieve and placed in an alumina crucible. The mixture was then heated to 1150°C with a temperature ramp of 5°C min^{-1} in a box furnace in an air atmosphere, and held at this temperature for 20 minutes to release the CO_2 and allow the melt to homogenise. Finally, the crucible was removed from the furnace and the liquid poured onto a clean, copper plate and pressed quickly with another plate to form thin, amorphous growth plates.

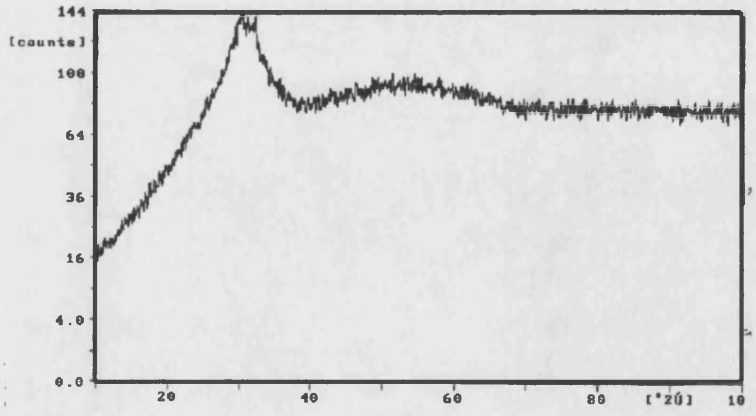

Figure 5.3. Results from an x-ray diffraction (XRD) analysis of the amorphous growth plates, showing the absence of any diffraction peaks, indicating an amorphous structure.

It is important to start from an amorphous growth material in order to obtain the correct whisker composition, so the melt-quenched material was checked for crystallinity using X-Ray Diffraction (XRD). An example scan is shown in Figure 5.3, where there are clearly no diffraction peaks, as required.

Once the growth plates have been made, the second stage is to anneal them in flowing oxygen. For this work, several different annealing temperatures in the range 780-890 °C were tried, with the best results obtained using a temperature of 860°C and an annealing time of 5-7 days. The oxygen flow rate was not found to affect whisker growth. A diagram of the axial furnace used is shown in Figure 5.4. Temperature profiles of the furnace showed that near the centre there was a gradient of about 0.6°C cm^{-1}, and the temperature was controlled to within 2°C using a NiCr-NiAl thermocouple and a Eurotherm temperature controller.

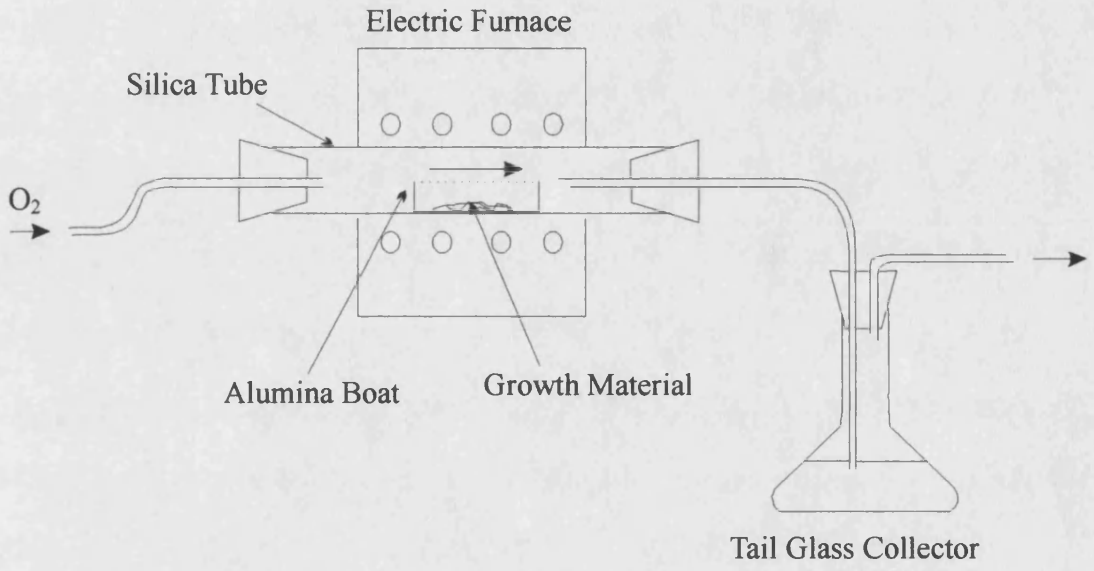

Figure 5.4. Diagram of the axial furnace used for annealing the growth plates and growing the whiskers.

At the end of the growth period, the furnace was turned off and the alumina boat quickly removed, to avoid any out-diffusion of oxygen as the furnace cooled, as this would affect the final doping levels (and hence T_C) of the whiskers. Figure 5.5 below shows many whiskers growing out of a growth plate, imaged after the alumina boat had been removed from the furnace.

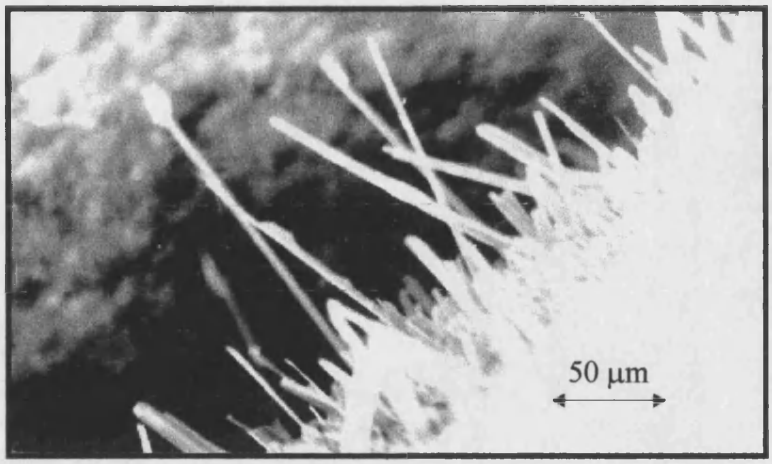

Figure 5.5. Whiskers growing out from an amorphous growth plate.

Although the whiskers in Figure 5.5 are clearly very short (sub-mm) many longer whiskers were present which had been removed for measurement, prior to the SEM image being taken.

5.4 Whisker Characterisation

Once the whiskers have been grown, the superconducting properties need to be characterised. This was achieved by two methods. Hall probe arrays were used to characterise magnetic properties, while electrical contacts were made to some of the whiskers to measure the transport properties.

To measure the magnetic properties, a suitable whisker (one which looked translucent under a microscope and showed no obvious defects or cracks) was selected and removed from the growth plate using a sharp needle. It was then transferred to a planar Hall array sensor and aligned over the active area using a hair mounted on a cocktail stick, and a micromanipulator. It was found that the whisker was held firmly in place by the Van der Waals force between the whisker and the GaAs-based Hall sensor (see Figure 5.6 below).

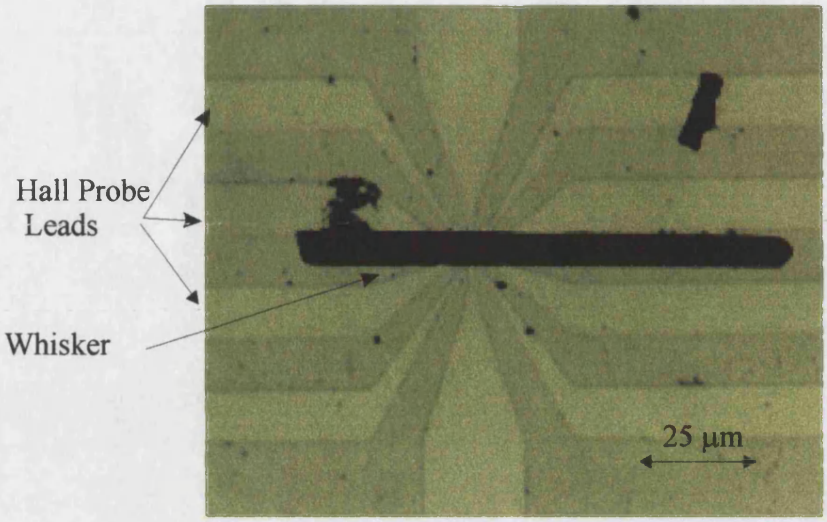

Figure 5.6. A Whisker mounted on a Hall probe array for characterisation

The lateral dimensions were deduced using the calibrated graticule on an optical microscope, and the (small) whisker thickness was measured using a Talystep surface profiler.

Figure 5.7 shows "local magnetisation" loops at various temperatures, which yielded two important pieces of information. Firstly, the absence of diamagnetism at very low fields (and any hysteresis) was used to estimate the critical temperature. Secondly the shape of the loops at $T<T_C$ showed little evidence of bulk pinning – the strong asymmetry and very small remanent magnetisation both indicate that surface pinning is dominating over any bulk pinning effects. The critical temperature was deduced from the temperature at which the field of first flux penetration became zero. Since the penetration field cannot necessarily be associated with the lower critical field (due to demagnetisation effects and the presence of surface barriers), the two-fluid temperature dependence could not be used, so the critical temperature was found by fitting a third order polynomial to the data. This procedure was used to determine T_C for the majority of the whiskers, since making electrical contacts to whiskers mounted on Hall bars proved problematic, as will be discussed later.

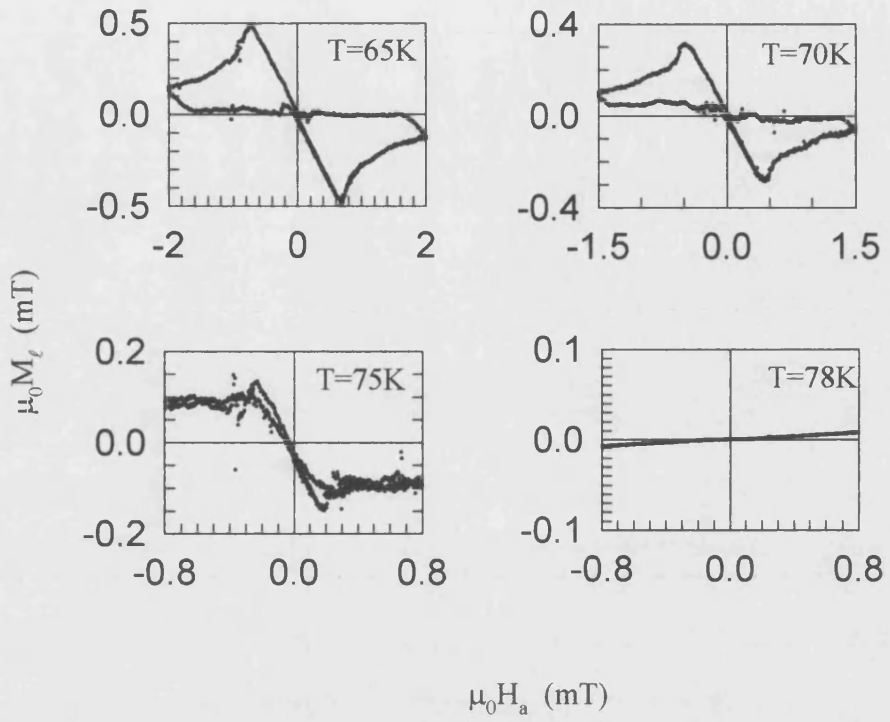

Figure 5.7. Local magnetisation loops used to determine T_C =78.4K

Figure 5.8 below shows penetration field data obtained from the hysteresis loops in Figure 5.7, and the third order polynomial fit.

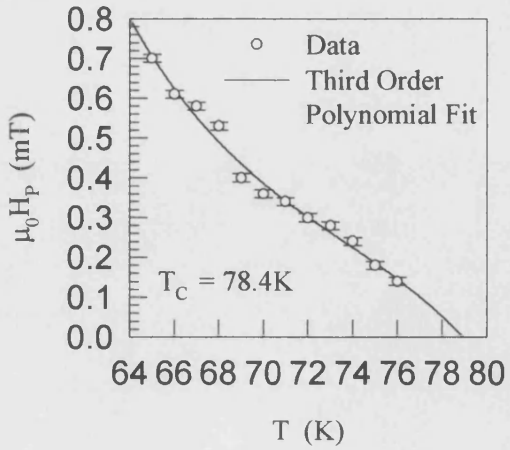

Figure 5.8. Temperature dependence of the penetration field, with the third order polynomial fit used to determine T_C.

It is clear from Figure 5.8 that the value of T_C is somewhat lower than the value of 92K obtained in optimally doped crystals, indicating that the oxygenation procedure or the stoichiometry is not quite perfect. Also, the shape of the graph, particularly the upturn of $\vec{H}_P$ at lower temperatures, is very different from that predicted by the two-fluid model of $\vec{H}_{C1}(T)$, suggesting that another mechanism is controlling vortex entry.

The second method used to characterise the whiskers involved making electrical contacts to them and measuring transport properties. Several different techniques have been suggested for making good, reliable, low resistance Ohmic contacts to BSCCO crystals. These include thermal evaporation [Lin, 1990] or laser deposition [Latyshev, 1993] of silver contacts, and silver paint [Chen, 1993]. Because of the large anisotropy of BSCCO, it is important to contact the sides of the whisker (the *ac* planes) as well as the large top face since the current flows principally along the CuO (*ab*) planes. Also, the large surface-to-volume ratio of the whiskers makes them particularly sensitive to degradation during any baking processes, and the small dimensions rule out more robust contacting methods such as pressed indium.

The technique chosen for this work was a compromise between robust contacts and ease of preparation, since no contact masks were available to utilise deposition techniques. A selected whisker was placed on an alumina substrate and four contacts were made using EPOTEK silver-loaded epoxy. The epoxy was deposited using a hair mounted on the arm of a micromanipulator, and then annealed in a flowing O_2 atmosphere at 460°C for 8 minutes, to allow the silver to diffuse into the whisker and make a good contact. The O_2 atmosphere was used to prevent too much oxygen out-diffusion during the annealing process, which would have had a detrimental effect on T_C. Finally, 12μm wide gold wires (shown in Figure 5.9) were used to make connections to a chip carrier, which was then mounted in a cryostat in order to make the measurements.

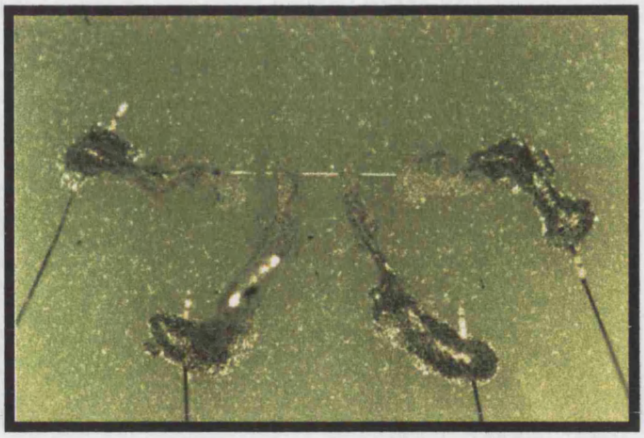

Figure 5.9. Photograph of a whisker contacted at four points using Ag-epoxy and gold bond wires.

Once mounted inside the cryostat, the whisker was connected to the measurement circuit in a four-point configuration, as shown in Figure 5.10. This procedure allowed an accurate measurement of the whisker resistance whilst excluding the effect of the lead and contact resistances.

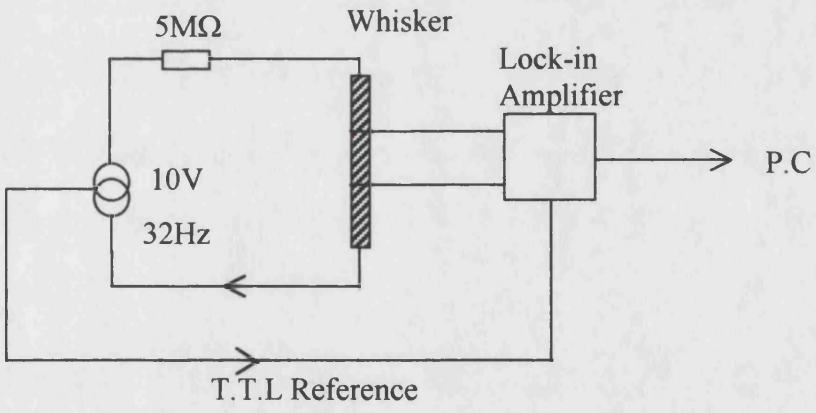

Figure 5.10. Measurement circuit used to determine the T_C with a four-point configuration.

An a.c voltage source enabled the use of very sensitive lock-in amplifier techniques. The temperature was swept downwards from about 100 K (well above the optimum T_C for BSCCO 2212) to 65 K at a rate of 0.5 K min^{-1}, and the voltage drop

across the whisker monitored. Since the measurement current is known, the resistive transition R(T) could be monitored directly. Figure 5.11 shows a typical R(T) plot obtained with a measurement current of 2 μA (peak-to-peak). The finite width of the transition leads to some ambiguity in the definition of T_C. In this work, T_C refers to the temperature at which the resistance falls below the detection limit of 0.1Ω. However, in much of the literature this is defined as T_{C0} and T_C is defined as the mid-point of the transition width ΔT_C.

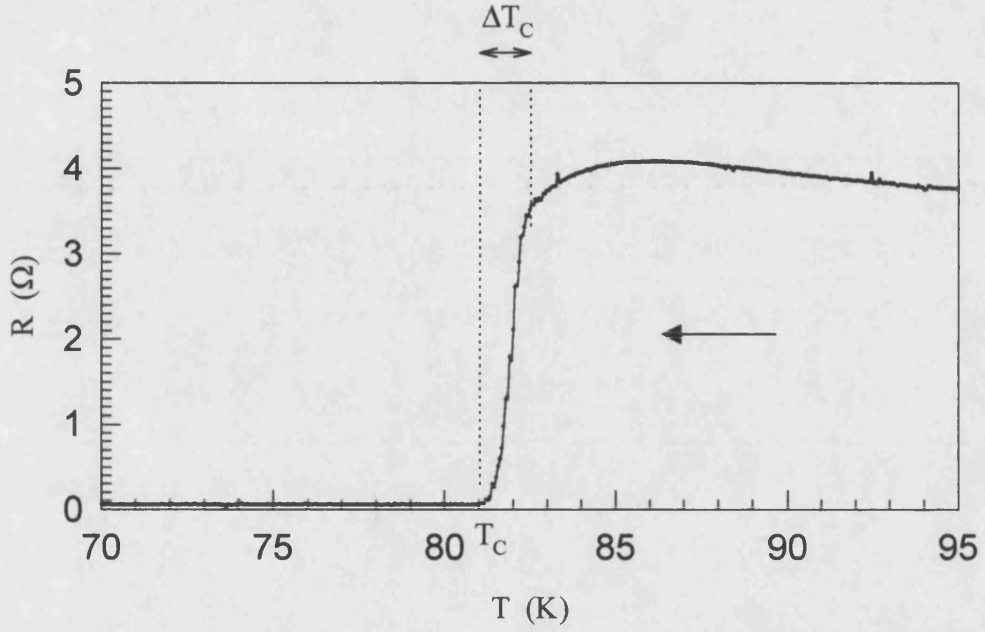

Figure 5.11. Typical resistance cooling curve for a whisker, measured using a current of 2 μA.

Chapter 6

Experimental Arrangement

6.1 The Hall Effect

The Hall effect was discovered by Edwin Hall in 1879, and has subsequently proved to be a very useful tool for investigating and measuring magnetic fields or charge carriers. The origin of the Hall effect is the interaction between charged particles and magnetic fields, and this interaction will now be reviewed.

Consider a slab of material of width d and thickness t, containing n carriers per unit volume, each having a charge q (and assume the carriers are electrons with charge –e) as shown in Figure 6.1.

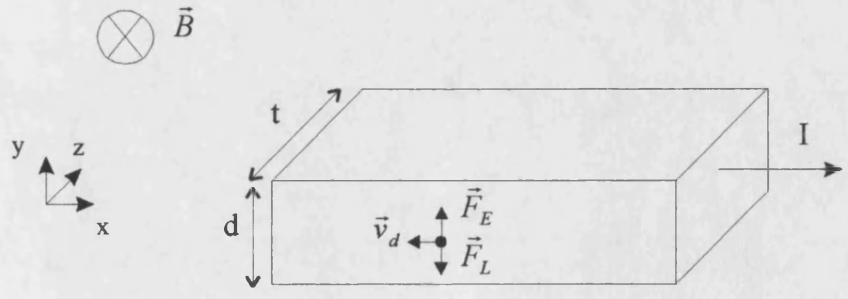

Figure 6.1. Geometry used in describing the Hall effect.

If an electric field is applied along the length of the material, the charge carriers will move parallel to the field with a drift velocity $\vec{v}_d$, producing a current I. If a magnetic field is now applied in the z direction, the carriers will experience a Lorentz force $\vec{F}_L$ in the y direction, causing a build-up of negative charge on the top surface and a net positive charge on the lower surface, as shown in Figure 6.1. This charge separation causes another electric field to be developed, which is normal to both the magnetic field and the current direction, and this is known as the Hall field, $\vec{E}_H$.

When the electrostatic force $\vec{F}_E$ due to the charge separation is balanced by the Lorentz force, an equilibrium situation is achieved and the charge carriers again move parallel to the current direction. In this equilibrium situation, the Hall field is directly proportional to the magnetic field, and expressions for the Hall voltage in terms of the material parameters can be derived. In equilibrium, the Lorentz force is equal (and opposite) to the electrostatic force,

$$q\vec{v}_d \wedge \vec{B} = q\vec{E}_H \tag{6.1}$$

However, the Hall voltage V_H is related to the Hall field by

$$\left|\vec{E}_H\right| = \frac{V_H}{d} \tag{6.2}$$

and the drift velocity can be written in terms of the applied current and the material parameters by

$$\left|\vec{v}_d\right| = \frac{I}{nAq}. \tag{6.3}$$

Combining (6.1), (6.2) and (6.3), the well-known expression for the Hall voltage is obtained

$$V_H = R_H IB, \tag{6.4}$$

where the Hall coefficient R_H is defined as $\frac{1}{nqt}$, I is the current and B the applied field.

For a sensitive magnetic field sensor based on the Hall effect, materials with a large Hall coefficient are required and, since q is fixed, the only variable is the carrier density. Hence, semiconductors are often used as Hall probe materials because of their intrinsically small carrier density compared with metals.

Another important factor to consider when choosing a material for Hall probes is the signal to noise ratio (SNR), defined as the ratio of the Hall voltage to the noise voltage. From (6.4), $V_H \propto I R_H$, and assuming the total power dissipation per unit area (given by I^2R) is constant, it follows that $I \propto \rho^{-\frac{1}{2}}$ so the Hall signal is given by

$$V_H \propto R_H \rho^{-\frac{1}{2}}. \tag{6.5}$$

If we further assume that the only source of noise is thermal Johnson noise from the probe resistance R, the noise voltage V_N is given by

$$V_N = \sqrt{4 k_B T R \Delta f} \tag{6.6}$$

where Δf is the measurement bandwidth, T the absolute temperature and k_B Boltzmanns' constant.

From (5.6), it can be seen that $V_N \propto \sqrt{\rho}$ so the signal to noise ratio is given by

$$SNR = \frac{V_H}{V_N} \propto \frac{R_H \rho^{-\frac{1}{2}}}{\rho^{\frac{1}{2}}} = \frac{R_H}{\rho}. \tag{6.7}$$

From this, good Hall probe materials therefore need to have a small resistivity for a good SNR, and a small carrier density in order to get a large Hall coefficient and consequently good field sensitivity.

Table 6.1 below shows the Hall coefficient and resistivity for several materials that have been used in the fabrication of Hall probes. The material known as a 2DEG (a two-Dimensional Electron Gas) is a material where electrons are trapped by a quantum well in a two-dimensional plane and hence the units of R_H and ρ will be reduced to ΩT^{-1} and $\Omega\ sq^{-1}$, respectively. The 2DEG will be described further in the next section.

Material	R_H ($\Omega\ m\ T^{-1}$)	ρ ($\Omega\ m$)	R_H/ρ (T^{-1})
AlGaAs/GaAs 2DEG (4.3K) [Stoddart, 1994]	4800 (ΩT^{-1})	56 ($\Omega\ sq^{-1}$)	86
AlGaAs/GaAs 2DEG (77K) [Stoddart, 1994]	4800 (ΩT^{-1})	370 ($\Omega\ sq^{-1}$)	13
GaAs (300K) [Börnstein, 1982]	8×10^{-3}	0.01	0.8
InSb (300K) [Saker, 1955]	3.5×10^{-4}	5×10^{-5}	7.0
InAs (300K) [Roshon, 1962]	7.5×10^{-5}	3.0×10^{-5}	2.5
Bi (300K) [Roshon, 1962]	1.0×10^{-6}	1.2×10^{-6}	0.8
Au (300K) [Roshon, 1962]	7.0×10^{-11}	2.2×10^{-8}	0.003

Table 6.1. Table showing the Hall coefficient and resistivity for various materials used in Hall probe fabrication.

It is clear from Table 6.1 that there is a trade-off between a low resistivity and a large Hall coefficient, and 2DEG's exhibit the best compromise at low temperatures, with a very large Hall coefficient and a reasonably small resistivity to give a good SNR.

6.2 The Two Dimensional Electron Gas

A two-dimensional electron system is formed when electrons are confined to a plane – such as electrons trapped on the surface of liquid Helium, or electrons trapped in the potential well formed at the interface of two different types of semiconductors. The latter example, hence forward known as a two-dimensional electron gas (2DEG), is used for fabrication of the Hall probes used in the work described in this thesis.

The 2DEG was grown by Molecular Beam Epitaxy (MBE) and is produced at the interface between GaAs and AlGaAs, as shown in Figure 6.2.

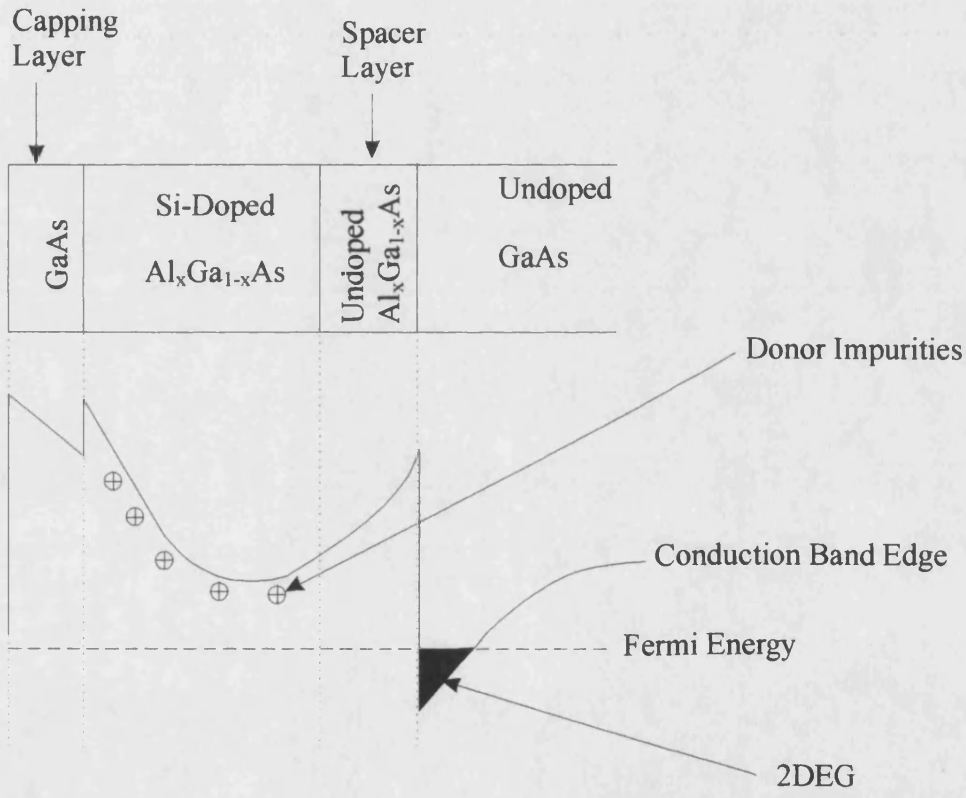

Figure 6.2. Conduction band profile across the semiconductor heterostructure (shown above). The location of the 2DEG and donor impurities are shown.

The Si-doped $Al_xGa_{1-x}As$ is used to provide the carriers, but is separated from the 2DEG by an undoped spacer layer in order to reduce the effect of ionised impurity

scattering. The positive donor impurities pull the conduction electrons in the GaAs towards the interface, where they are confined in a very narrow, triangular potential well. Since the width of the well is less than the electron mean free path, the electrons are constrained to move in two dimensions parallel to the plane of the interface. In the direction normal to the interface, the electron is confined and its energy spectrum is found by solving Schrödingers' equation

$$\left(\frac{-\hbar^2}{2m^*}\frac{d^2}{dz^2}+V(z)\right)\Psi = E\Psi \tag{6.8}$$

where m^* is the effective mass of GaAs. The solution is a set of discrete energy levels (called subbands), whose separation and number depend on the triangular well dimensions. In the 2DEG used in this work, a low electron concentration means that only the first subband is occupied, with the wavefunction peaking at about 50Å below the AlGaAs/GaAs interface [Stoddart, 1994].

The 2DEG resistivity is determined principally by the electron mobility, which is reduced by phonon scattering at elevated temperatures (around room temperature) and impurity scattering at low temperatures. To increase the mobility, and hence reduce the resistivity, the 2DEGs are used at low temperatures (to reduce phonon scattering) and the spacer layer in the heterostructure reduces ionised impurity scattering, as mentioned earlier.

6.3 Hall Probe Design

Hall probes have been used by many workers for investigating vortex structure and dynamics (although rarely with such good resolution as the probes described in this work) and their advantages are described below, together with some of the other techniques commonly used. The main techniques used for studying the magnetic properties of superconductors are Superconducting Quantum Interference Device (SQUID) magnetometry, Vibrating Sample Magnetometry (VSM), muon Spin Rotation (μSR) and Small Angle Neutron Scattering (SANS).

SQUID's provide by far the most sensitive measurements, with minimum detectable fields as low as 10^{-10} T easily attainable. The disadvantage of SQUID's is that the spatial resolution is limited by the size of the pickup loop (typically 10μm × 10μm), and the field and temperature range are limited by the properties of the superconducting components used.

VSM's are commonly used magnetometers, since they can be employed in a very large field-temperature regime. [See for example Cohen, 1997] They are based on detecting the voltage induced in pickup coils as the sample is moved through, and are very good for differential measurements because only the change in flux density is detected and any constant applied field only produces an offset. The principle disadvantage from the point of view of this work is that they only give globally-averaged values of the magnetisation, and any spatial variation in flux density is averaged out.

Small Angle Neutron Scattering (SANS) measurements are based on the interaction between the magnetic moment of the neutrons and the vortices The scattered neutrons can give information on correlations between vortices, leading to observations of lattice melting and vortex decoupling [Cubitt, 1993]. The main drawback of SANS (apart from the need for a neutron source) is the requirement for large, high quality samples.

Muon spin rotation experiments measure the distribution of precession frequencies as the spin-polarised muons precess in the local internal field of the mixed state. μSR experiments are complex, but can provide very useful information since they are extremely sensitive to structural changes in the vortex state. Hence, muons have been used to study lattice melting and vortex decoupling. [Lee, 1995, and Blasius, 1999] The main disadvantage is in the complexity of the experiment: the raw data is not a direct measurement of magnetic flux density, and is not trivial to analyse.

In contrast to these techniques, Hall probe arrays provide a direct, local measurement of the magnetic flux density throughout a large temperature range (up to about 150K, where phonon scattering significantly reduces the electron mobility) and field range and are relatively simple to fabricate. Hall probes are also practically non-invasive, with a self-field $\left|\vec{B}_{self}\right|$ due to the Hall current I_H given approximately by

$$\left|\vec{B}_{self}\right| \approx \frac{\mu_0 I_H}{2\pi a} \tag{6.9}$$

where a is the sample-sensor separation. Assuming a typical Hall current of about 2μA, and a 0.5μm sample-sensor spacing, the probe will generate a self-field of ~1.0μT, which is less than the minimum detectable flux density of ~10μT.

This versatility has lead to Hall probes being employed by many research workers. For example, vortex lattice melting has been observed by Zeldov *et al.*, [1995] using a 10μm 2DEG probe, and Majer has shown, using a similar probe, that the irreversibility line and melting line may not coincide. [Majer, 1995] The effect of disorder on the phase diagram of BSCCO has been studied by Khaykovitch, [Khaykovich, 1997] and Shung *et al.* [1997] have used 3μm Bismuth Hall probes to investigate telegraph noise in YBCO crystals. Also, Fuchs *et al.* have used an array of seven 10μm Hall probes to determine the current distribution in a BSCCO crystal under different temperature and field regimes [1998]. The "state of the art" in static Hall probe sensors is an array of 2μm Hall probes used to achieve single vortex resolution by Stoddart *et al.* [Stoddart, 1995] in a Niobium film.

To allow limited spatial resolution, the Hall probes used in this work were designed as a linear array, which was lithographically patterned into the heterostructure. Figure 6.3 shows an optical micrograph of a 2μm wire-width array, where the dimension refers to the smallest feature size of the Hall probe. Each fabricated chip contained four serially connected Hall probe arrays – two 1μm, one 2μm and one 4μm array, with the array designed to allow flux profiles across a superconductor to be investigated.

Although the 4μm probe was perfectly adequate for looking at bulk crystals, the BSCCO whiskers, with typical widths of 12μm, had to be aligned on either 2μm or 1μm arrays. Since 1μm is approaching the limit for optical lithography, it was not unusual for some of the probes on these arrays not to work, due to "pinching off" of the active area, leading to a depletion of carriers in the 2DEG and an excessively large resistivity.

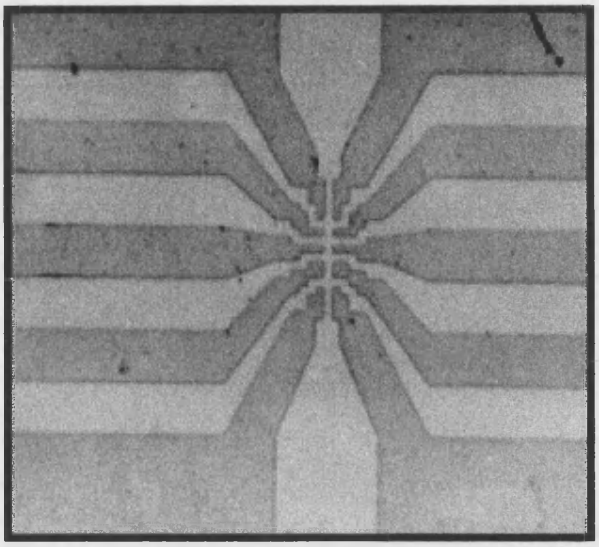

Figure 6.3. Optical micrograph of a 2μm Hall probe array.

For this reason, the 2μm wide arrays were most often used. It should be noted, however, that the larger probes are significantly less "local", and produce a more spatially averaged signal due to the large active area relative to the area of the superconductor. This was a particular problem for the whiskers, which had typical widths of about 12μm, so the 1μm probes were the only arrays small enough to be used for lateral flux profile measurements.

6.4 Hall Array Fabrication

The Hall sensor arrays were fabricated at Bath from epitaxially grown wafers of GaAs/AlGaAs 2DEG heterostructure (grown at Nottingham University), using conventional optical lithography and chemical wet etching techniques, which are described below.

1 The wafer was scribed, and then cleaved into chips 5×5 mm^2

2 Cleaning

The chips were placed in beakers of (i) 1-1-1 trichloroethane, (ii) hot acetone and (iii) propanol, and cleaned in an ultrasonic bath for 5 minutes in each solvent. They were then dried using a nitrogen jet.

3 Each chip was glued to a cover slip with photoresist and then baked at 95°C for 30 minutes, to enable easy handling.

4 Photolithography

Shipley Microposit 1813 was spun onto each chip at a speed of 4000 rpm for 25 seconds, to produce a layer approximately 1.3 μm thick, which was baked for 25 minutes at 95°C. The chips were then exposed to ultraviolet radiation through a chrome mask, to define the Ohmic contacts, and the photoresist developed in Microposit 351 developer for approximately 30 seconds to remove the unwanted areas. Any remaining developer was removed by washing the chips in distilled water and drying.

5 Ohmic contacts

Each chip was dipped in a solution of 1:1 $HCl:H_2O$ and then washed in distilled water, to remove any surface oxide. The chips were then immediately placed into a thermal evaporator and heated to 80°C under high vacuum. Before deposition, the chips were cleaned using an Ar glow discharge for 10 minutes. To make electrical contact to the 2DEG, 66 nm of Ge and then 134 nm of Au were deposited, which produce a good Ohmic contact to the 2DEG when properly annealed (See next step). Finally, 20 nm of Ti and 200 nm of Au were deposited, to produce a contact area suitable for ultrasonic bonding. After removal from the evaporator, the chips were placed in acetone and gently agitated, to "lift-off" the unwanted metal regions, leaving just the defined contact pads. This lift-off procedure could be improved if the chips were soaked in chlorobenzene for 12 minutes and then left to dry for 2 hours before developing, which produces an overhang in the photoresist.

6 Annealing

After being cleaned, each chip was placed in a flash annealer and the contacts annealed in a N_2/5% H_2 reducing atmosphere at 430°C for 2 minutes. This produces an n^+ region below the pads which makes a low resistance Ohmic contact to the 2DEG.

7 Etching

After cleaning and re-mounting the chips, photoresist was spun on at 4000 rpm for 4 seconds, 6000 rpm for 12 seconds and then baked. The higher spin speed was used to reduce the effects of edge beading (build-up of photoresist at the edges of the chip) which could cause problems during exposure because of the small dimensions of the Hall bar mask. After the Hall probe array had been exposed and developed, the chips were again baked, to reduce damage to the photoresist during etching. To remove any surface oxide, the chips were dipped in 1:1 $HCl:H_2O$ and then washed and dried, immediately before etching. They were then etched in a solution of distilled water, 30% H_2O_2 and concentrated H_2SO_4 in the ratio 160:8:1, which produced an etch rate of ~0.2 $\mu m\ min^{-1}$. An etch time of 15 seconds was sufficient to deplete the 2DEG in the unwanted areas. After etching, the chips were washed in distilled water and the remaining resist removed with acetone.

6.5 Experimental Apparatus

Once the chips containing the Hall probe array structures had been fabricated, it was necessary to mount them on chip carriers in order to be able to make measurements inside the cryostat. The chips were glued onto home-made alumina chip carriers using silver-epoxy, which was cured at 80°C for 90 minutes. An ultrasonic bonder was used to make electrical connections to the chip, employing 12.5μm diameter gold wire. This technique uses a pulse of ultrasonic energy to join the wire to the contact pads, as shown in the photograph in Figure 6.7. To connect the chip carrier to the cryostat, enamelled copper connecting wires were soldered to the chip carrier using Indium solder. Indium is preferred over the conventional Pb-Sn solder because of its reliability at low temperatures. Also, In has a superconducting transition temperature of 3.4 K, which is below the lowest working temperature of our cryostat (4.2 K). The transition temperature of Pb is 7.2 K, and this could cause problems at liquid helium temperatures.

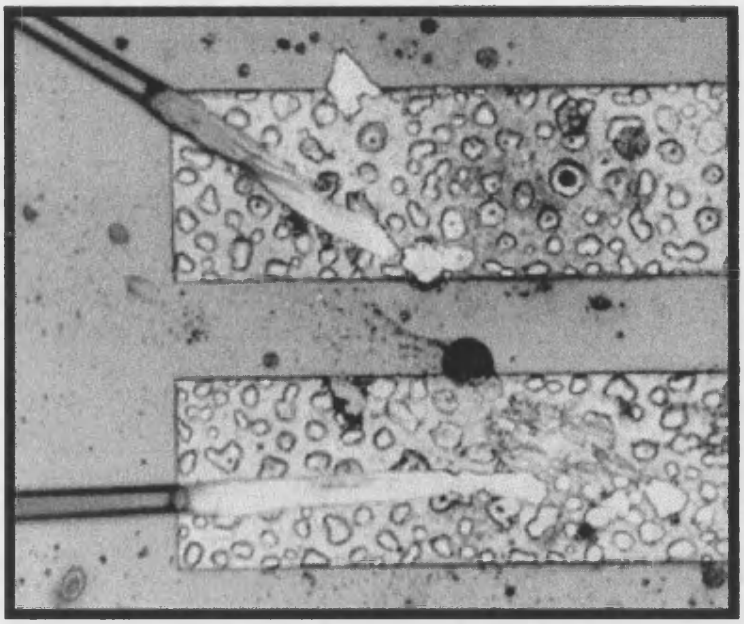

Figure 6.7. Gold wires ultrasonically bonded to contact pads on the Hall probes.

There are only enough pads on each carrier to bond one of the Hall probe arrays, so each chip was checked on a probing station to find the best array from resistance measurements. Values for lead resistances varied according to the size of the array, the properties of the original wafer, temperature, and amount of illumination (because of the persistent photoconductivity effect at low temperatures), but it was found that typical values for a 2μm array in the dark, at room temperature, were ~300KΩ. It should be noted, however, that many of the 1μm arrays appeared open circuit at room temperature but began to work at low temperatures after illumination. This effect could be somewhat dramatic, with low temperature resistances being reduced from ~ KΩ to ~ 10Ω.

Once the required array had been selected, it was bonded to the chip carrier using 12 pads: 8 voltage leads (corresponding to four probes) and four current leads, as shown in Figure 6.8.

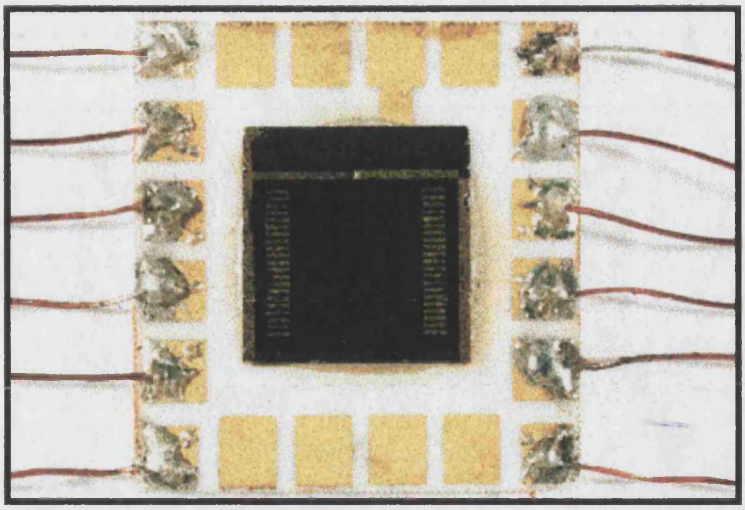

Figure 6.8. Photograph of A Hall probe chip mounted on a chip carrier, showing copper wires, Indium soldering and the gold bond wires. Each chip contains four arrays, with each array having four voltage leads and two current leads, which can be seen as the small, gold rectangles near the edge of the chip.

The Hall probe array / chip carrier structure was mounted on a sample holder using GE varnish, and the sample holder placed inside a glass cryostat, as shown in Figure 6.9. The sample holder also contained an infrared LED, which was used to illuminate probes with excessively large resistances. This had the effect of exciting electrons from deep-donor states in the AlGaAs layer into the conduction band, (the persistent photoconductivity effect) thereby reducing the probe resistance and improving the SNR at low temperatures. The 25Ω costantan wire heater, used to control the sample temperature, was bifilar wound in order to avoid generating any additional magnetic fields. The temperature was monitored with a calibrated carbon glass resistor, and controlled with a Lakeshore DRC-91CA temperature controller. Liquid nitrogen was used as the cryogen for temperatures down to 65K and liquid Helium opened up a temperature range down to 4.2K. The sample tube was filled with 100 Torr of Helium exchange gas, which acted as a heat link between the sample and the cryogen bath. Magnetic fields were provided by a calibrated NbTi superconducting solenoid, which could produce fields up to 1T when cooled in liquid

Helium, and fields up to 10mT at temperatures above 65K, when the solenoid was in its normal state.

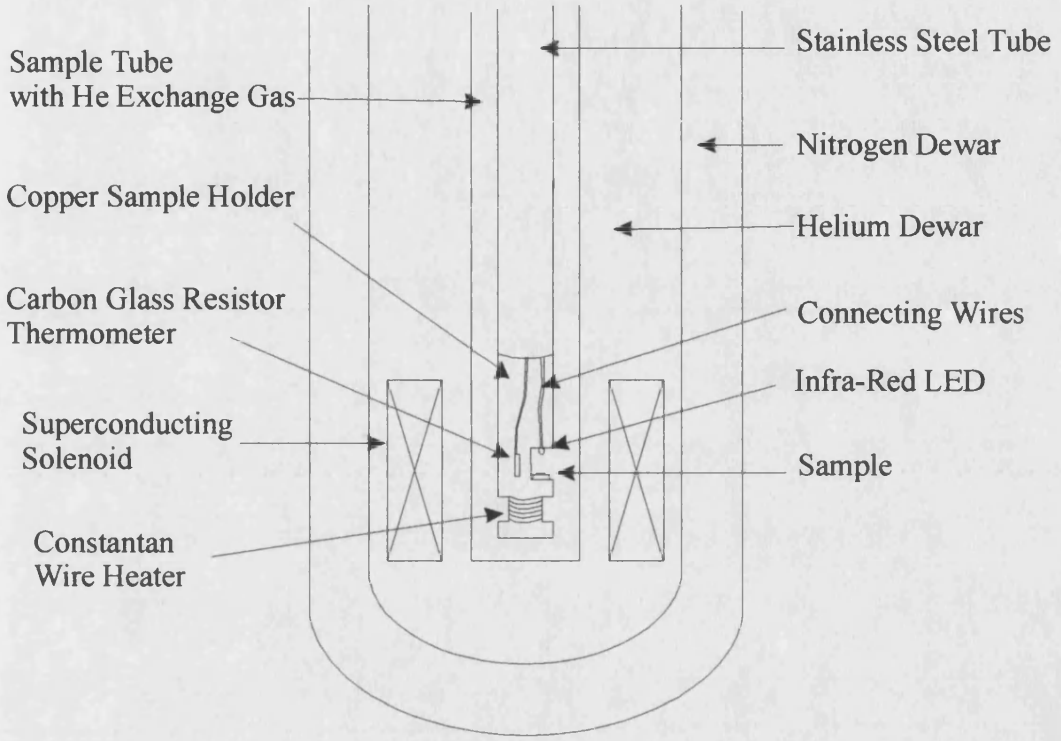

Figure 6.9. Diagram of the cryogenic apparatus, including the copper sample holder and glass dewar.

To compensate for the magnetic field of the earth, an FW Bell Gaussmeter was used to measure the magnetic field of the solenoid with no current passing through it. The measured value of the Earth's magnetic field along the axis of the cryostat was (20±2)μT, where the offset of the Gaussmeter has been taken into account. The solenoid was driven by a Keithley 220 Current Source for currents up to 100mA, and for larger currents a Kepco 400W bipolar power supply was used.

Measurements were carried out using the circuit shown in Figure 6.10. A 32Hz, 10V a.c Hall current was provided by the Philips PM5109 signal generator, with the 5MΩ resistor used to convert this to a constant current source. The Hall voltage was monitored using an EG&G 5210 lock-in amplifier, with the phase difference between the signal and the reference signal (from the signal generator)

being kept to less than 10°. The Hall current was monitored via the voltage drop across the 1KΩ series resistor.

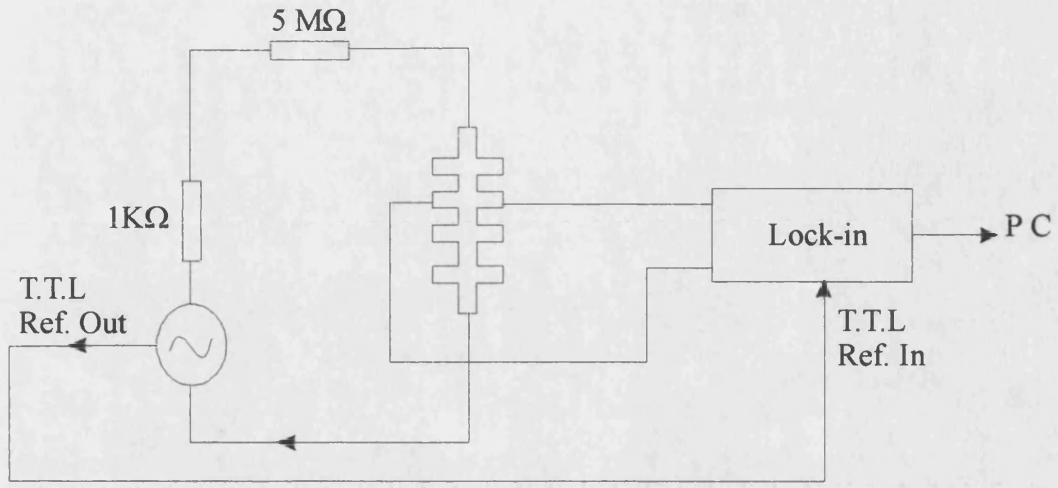

Figure 6.10. Measurement circuit for detecting the Hall voltage.

Chapter 7

Vortex Penetration Results

7.1 Local Magnetisation Results

Once the whisker was aligned on the Hall bar array, the first experiments to be carried out were isothermal local hysteresis loops. Figure 7.1 below shows a typical $B_\ell(H)$ loop obtained for a whisker, which has been zero-field cooled (ZFC) from above T_C to the required measurement temperature.

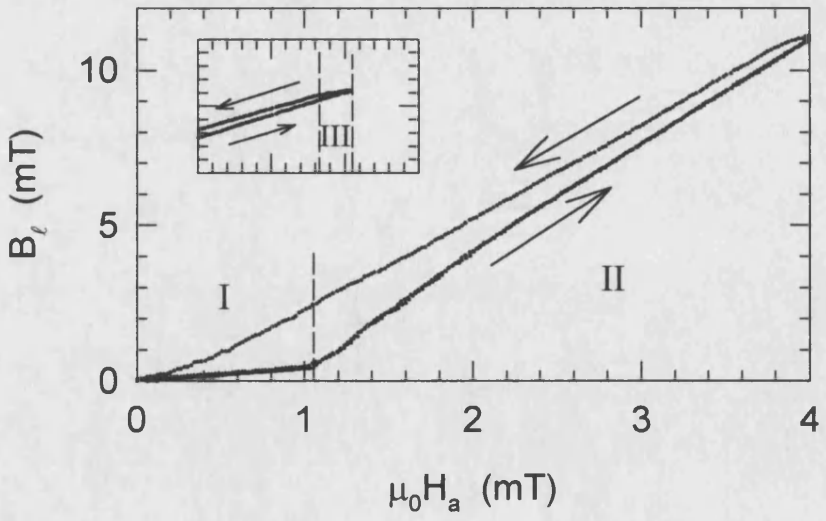

Figure 7.1. Local Magnetic Induction Loop of a BSCCO Whisker measured at 66K after being ZFC. The inset is a magnified image of the region near the end of the hysteresis loop, and regions I, II and III are referred to in the text.

As the applied magnetic field (H_a) is increased from zero (the initial magnetisation leg), the flux density is completely expelled by the Meissner screening currents up to a field H_P. This is Region I in Figure 7.1. Above the penetration field H_P, the surface barriers collapse and vortices are free to enter. Hence, the local magnetic flux density B_ℓ begins to increase (region II) as more vortices enter, creating the dome-like profile described earlier. At the extreme of the hysteresis loop (H_{max}) the applied field starts to reduce, but because of the vortex free region at the edges of the dome, vortices cannot exit and so the signal remains constant (region III). At a field H_{ex} the edges of the dome extend to the edge of the whisker and vortices are now free to exit. At lower fields, (on the downward leg) the vortices leave the whisker and $B_\ell \approx \mu_0 H_a$, i.e. there is almost no magnetisation. When H_a returns to zero, there is very little measured flux density implying that there are few vortices trapped inside the whisker. We conclude from this that this whisker has very weak bulk pinning, and the hysteresis is due almost entirely to surface barriers (either Bean-Livingston or geometrical barriers).

Closer inspection of region I reveals a small, non-zero slope in the Meissner phase (see Figure 7.2 below).

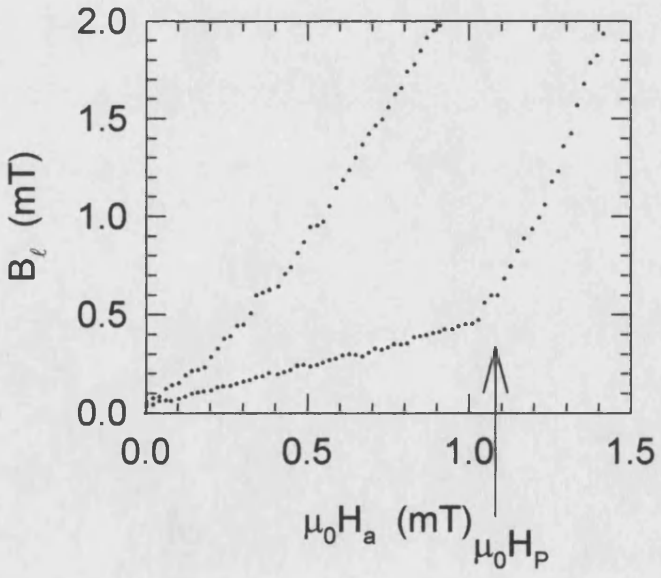

Figure 7.2. Hysteresis loop near the origin, showing the non-zero slope of the Meissner phase.

This slope is due to the small separation between the 2DEG, which is about 80nm below the surface of the Hall bar array, and the surface of the whisker. In this space, variations in the local flux distributions decay rapidly, as shown schematically in Figure 7.3 below, which illustrates a whisker in the Meissner state but with a large distance between whisker and 2DEG.

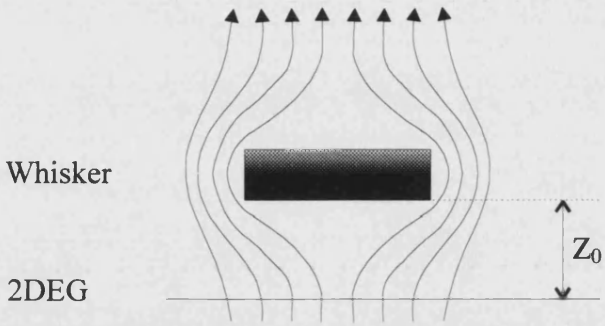

Figure 7.3. Origin of the non-zero Meissner phase slope.

The slope of the Hall voltage in the Meissner phase can be used to estimate the separation Z_0 between the whisker and the 2DEG Hall sensor. As shown by Stoddart *et al.*, [S.T.Stoddart, 1994] the magnetic field intensity at a point Z_0 above a superconductor of width 2W is approximated by

$$H(Z_0) \approx H_a \frac{Z_0}{W} \tag{7.1}$$

where H_a is the applied magnetic field intensity and $H(Z_0)$ is the measured field at a point Z_0 above the centre of the superconductor. For the data shown in Figure 7.1 (using a whisker width of 12μm), this analysis gives a superconductor-sensor separation of about 2.4μm.

To better characterise the hysteresis in the $B_\ell(H)$ loops, a quantity called the local magnetisation M_ℓ is introduced, which is defined as

$$\mu_0 M_\ell = B_\ell - \mu_0 H_a, \tag{7.2}$$

where B_ℓ is the measured local flux density and H_a is the applied magnetic field intensity. The local quantity defined above is distinct from the conventional bulk magnetisation M, which is defined as the magnetic moment per unit volume and is an average thermodynamic quantity (as opposed to the local measurement from the Hall probes). Figure 7.4 (a) below shows the local magnetisation loop as derived from (7.2).

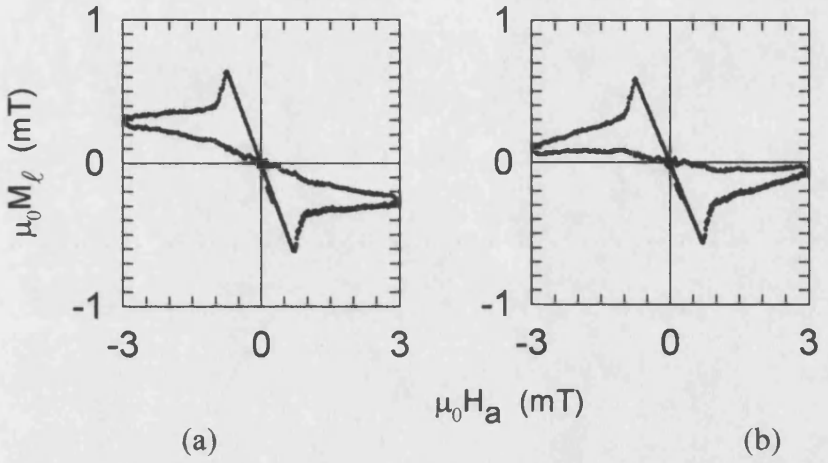

Figure 7.4. Local magnetisation loops for a whisker at 66K. (a) shows the raw data and (b) shows the corrected loop.

The background slope evident in Figure 7.4 (a) is a result of the calibration procedure used, where the calibration is carried out above T_C and then used at all subsequent temperatures, ignoring the weak temperature dependence of the Hall coefficient. To correct this, a factor c is introduced to 7.2. The magnetisation data are then fitted to the equation

$$\mu_0 M_\ell = B_\ell - c\,\mu_0 H_a, \tag{7.3}$$

The correction factor c was found to be always in the region 0.97-1.03, and the raw and corrected data are shown in Figures 7.4(a) and 7.4(b) respectively.

Figure 7.5 shows the local magnetisation loops obtained after zero-field cooling a whisker from above T_C to the measurement temperature.

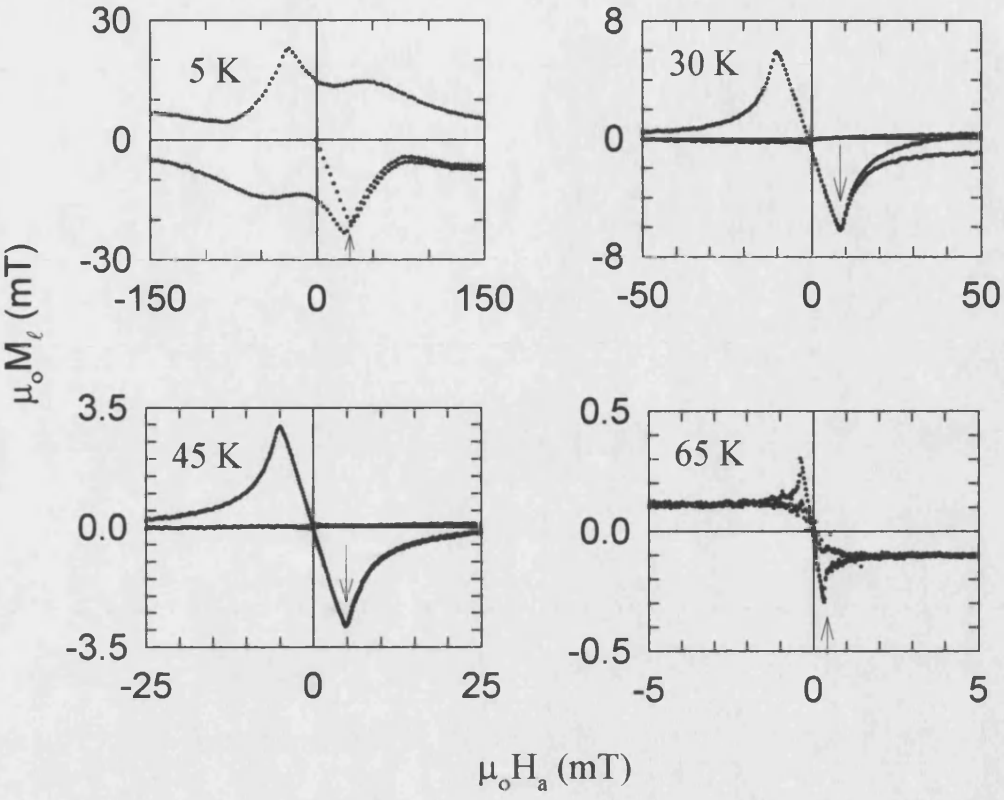

Figure 7.5. Isothermal local magnetisation loops for whisker I mounted on a 2μm Hall bar array.

The shape of the hysteresis loops at temperatures of 30K and above is entirely consistent with a system dominated by surface barriers (B-L or Geometrical), with a very small magnetisation on the downwards leg (note the changing y-axis scales) and almost no remanent magnetisation (defined as the magnetisation measured at the end of the hysteresis loop: $M_\ell(H_a=0)$). The almost field-independent constant magnetisation evident in the 65K data is probably due to some small bulk pinning effects. The temperature dependence of the remanent magnetisation is plotted in Figure 7.6, where it is clear that the M_R drops off approximately exponentially with increasing temperature. The magnitude of the remanent magnetisation at temperatures greater than about 20K suggests that bulk pinning is not important in these whiskers and that the principle vortex pinning mechanism must therefore be surface-driven i.e.

surface barriers dominate both the entry, and subsequent motion of, vortices in these whiskers.

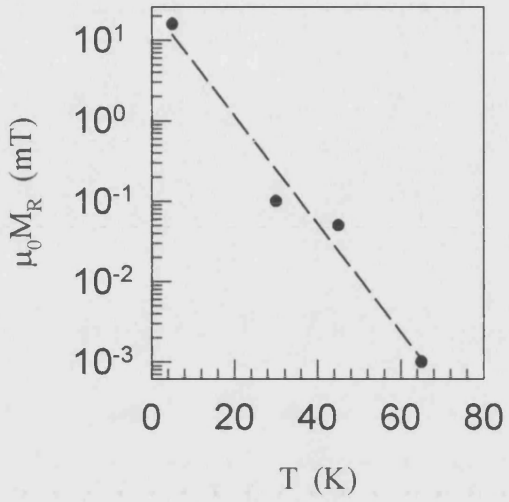

Figure 7.6. Temperature dependence of the remanent magnetisation of whisker I.

The effect of increasing the field excursion of the hysteresis loop was investigated by carrying out three different ZFC loops to increasing maximum fields. The results are shown in figure 7.7 below, and it is clear that the amount of trapped flux does not change when varying the maximum applied magnetic field.

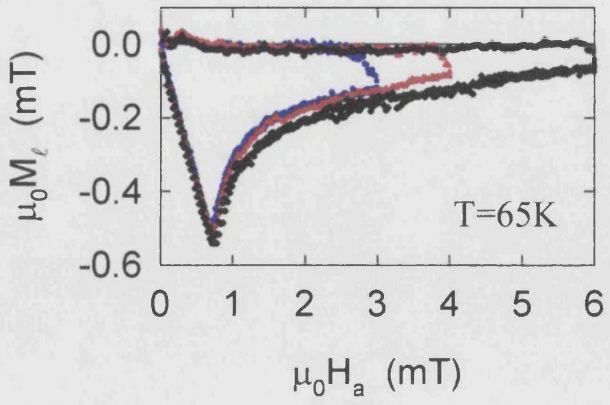

Figure 7.7. Effect of increasing the maximum field excursion on the hysteresis loop of whisker II.

This again suggests that the pinning is predominantly due to surfaces, since bulk pinning would normally be affected by the maximum field sweep.

7.2 Temperature Dependence of the Penetration Field

The magnetic field at which vortices first start to enter the superconductor, $\vec{H}_P$, is known as the penetration field, and can be significantly different from the thermodynamic lower critical field $\vec{H}_{C1}$ for two principle reasons.

First, demagnetisation effects are particularly important in the perpendicular geometry used in this work. The actual field at the superconductor, $\vec{H}_{edge}$, is related to the applied magnetic field $\vec{H}_a$ by

$$\vec{H}_{edge} = \frac{\vec{H}_a}{1 - N_D}, \tag{7.4}$$

where N_D is the demagnetising factor. For the whisker geometry $N_D \approx 0.98$, which means that vortices will begin to enter the superconductor at very small applied fields. If surface effects are neglected, demagnetisation effects will reduce $\vec{H}_P$ to $\vec{H}_{C1}/50$.

The second effect, which is more difficult to quantify, is the effect of surface barriers or geometrical barriers. As shown earlier, both types of barrier have the effect of delaying vortex entry to a field $\vec{H}_P > \vec{H}_{C1}$, and in the case of Bean-Livingston barriers the penetration field for two-dimensional vortex pancakes should have a strong temperature dependence given by [Burlachkov, 1994]

$$\vec{H}_P = \vec{H}_C e^{-\frac{T}{T_0}}, \tag{7.5}$$

where $\vec{H}_C$ is the thermodynamic critical field and T_0 is a parameter defined as

$$T_0 = \frac{\varepsilon_0 d}{k_B \ln\left(\frac{t}{t_0}\right)} \tag{7.6}$$

with ε_0 the vortex line energy per unit length, d the layer separation and t_0 a characteristic time scale. Equation (7.5) is applicable in the vortex pancake limit.

In contrast to this strong temperature dependence from Bean-Livingston barriers, geometrical barriers are only expected to exhibit a very weak temperature dependence [kuznetsov, 1997] of $\vec{H}_P$, which disappears completely in the absence of bulk pinning.

Figure 7.8 below shows the penetration field versus temperature for three different whiskers. The solid lines are fits to equation (7.5), where the two fluid model has been used for the temperature dependence of H_C, given by

$$\vec{H}_C(T) = \left(1 - \left(\frac{T}{T_C}\right)^2\right). \tag{7.7}$$

Fits of this data to equation (7.5) yield values of $\vec{H}_C(0)$, T_0 and T_C given in the table below.

Whisker	$\mu_0 H_C(0)$ (mT)	T_0 (K)	T_C (K)
I	36.9	26.2	77.1
II	56.8	22.2	73.2
III	90.2	17.1	90.0

Table 7.1. Fitted values of T_0 and $\mu_0 H_C(0)$ for three whiskers.

The values of T_0 obtained from the high-field penetration field data are in good agreement with the calculated value of 23K [Burlachkov, 1994], obtained using typical parameters for BSCCO.

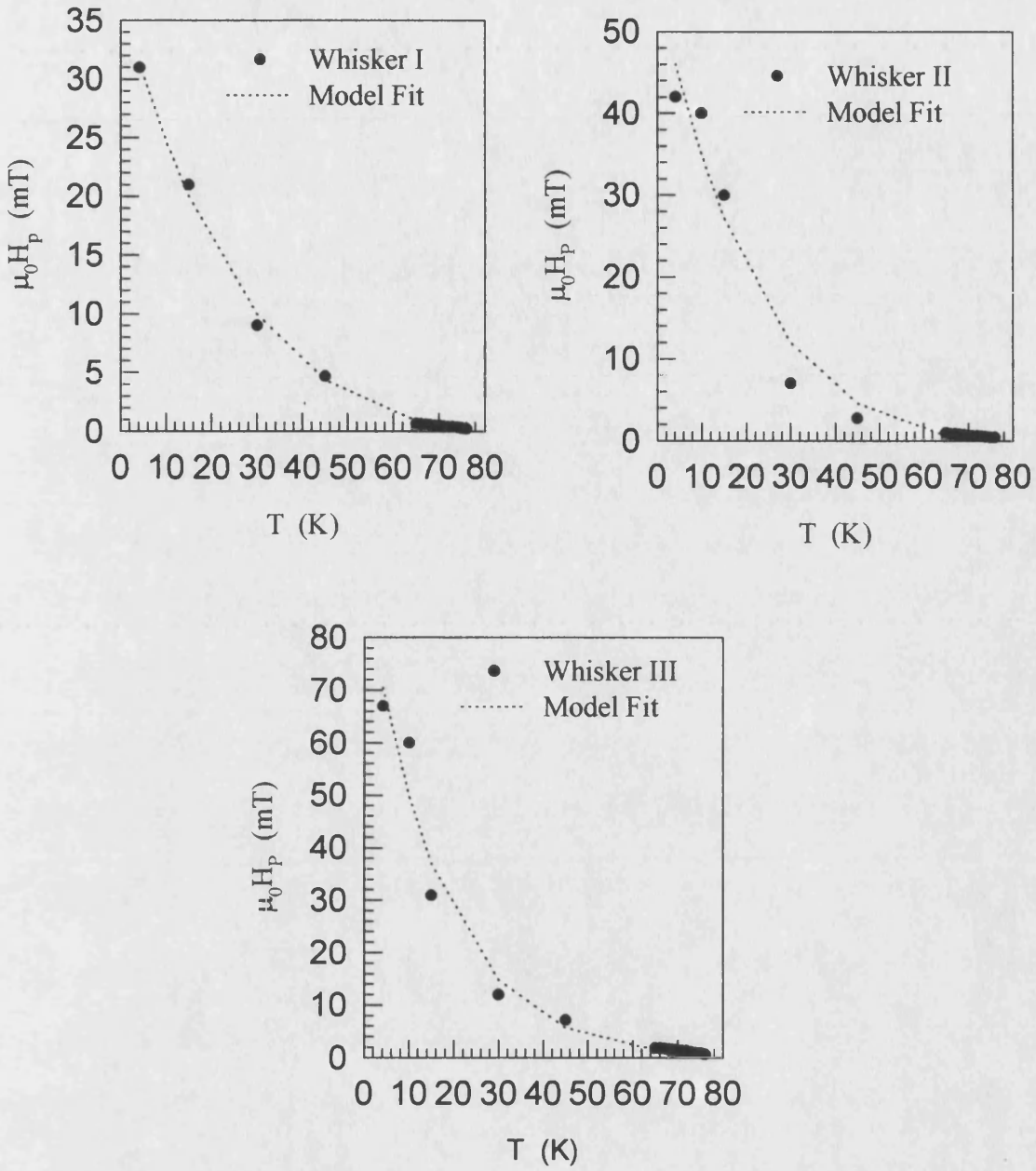

Figure 7.8. Temperature dependence of the penetration field for three different whiskers.

Assuming a Ginzburg-Landau parameter of 100, estimates of $\vec{H}_{C1}(0)$ can be obtained from

$$\vec{H}_{C1} \approx \frac{\vec{H}_C}{\sqrt{2}\kappa} \ln(\kappa), \tag{7.8}$$

assuming the correct demagnetisation effects are accounted for. As described earlier, demagnetisation effects lead to the measured value of $\vec{H}_P(T)$ being an underestimate by a factor $1/(1-N_D)$, where N_D is the demagnetisation factor. For the platelet geometry of the whiskers, N_D is very large, and can be estimated from a standard method of approximating the whisker as an elongated ellipse [Osborn, 1945]. Using this method, a value of $N_D \approx 0.98$ is found for the whiskers.

The definition of T_0 allows estimates of the vortex line energy per unit length ε_0, assuming the parameter $\ln(t/t_0)=30$, as suggested by Burlachkov [Burlachkov, 1994]. Since T_0 defines ε_0 in units of Kcm^{-1}, the derived values of ε_0 must be multiplied by k_B to convert to J m^{-1}. Table 7.2 below shows values of $\vec{H}_{C1}(T)$ and ε_0 derived from the $\vec{H}_P(T)$ fits.

Whisker	$\mu_0 H_{c1}(0)$ (mT)	ε_0 (10^{-12} J m^{-1})
I	60.1	7.2
II	89.2	6.1
III	146.9	4.7

Table 7.2. Material parameters for three whiskers, derived from equations 7.7 and 7.8, and the fitted data in Figure 7.9.

The values obtained for the vortex line energy per unit length are in good agreement with the calculated value for BSCCO of $\varepsilon_0 = 7\times10^{-12}$ J m^{-1}. The values for $\vec{H}_{C1}(0)$ are somewhat larger than those obtained by other workers for BSCCO, particularly values obtained by Niderőst *et al.*, [Niderőst, 1998] who found $\mu_0\vec{H}_{C1}(0)$ = 10.4 mT using magnetic measurements on large single crystals.

7.3 Sweep Rate Dependence of the Penetration Field

As shown earlier, the Bean-Livingston barrier is essentially a kinetic barrier and as such will be surmounted by vortex creep over a sufficiently long time. This has been observed experimentally by investigating the sweep rate dependence of the penetration field [Nederöst, 1998]. Previous work on BSCCO 2212 crystals has shown that, below a temperature-dependent sweep rate, the penetration field collapses to a lower plateau, which is interpreted as the thermodynamic lower critical field $\vec{H}_{C1}$. In contrast to this situation, geometrical barriers are not expected to exhibit any significant vortex creep, since the height of the barrier is of the order $\varepsilon_0 s$, where s is the thickness of the superconductor, which is very large for bulk crystals (typically several hundred microns). Hence, as well as providing a direct measurement of $\vec{H}_{C1}$, measurements of the sweep rate dependence of $\vec{H}_P$ should allow one to differentiate between the two major types of surface barrier: B-L or geometrical.

The measurements were carried out by zero-field cooling the whisker to the measurement temperature and then carrying out an initial sweep of the magnetisation loop. Figure 7.12 shows the results for four different sweep rates, measured at a temperature of 68K, and the penetration fields are marked with arrows. It was impractical to carry out these experiments at temperatures lower than 68K, as the glass cryostat would not stay cold for long enough to complete the measurement. The penetration field is defined as the field at which magnetic flux first starts to enter the superconductor, and is signified by a change in slope of the initial leg of the hysteresis cycle. For the whiskers used for this work, the change in slope at the penetration field was accompanied by a sharp jump in the local induction (see Figure 7.9), making the penetration field easily identifiable. The data exhibit clear evidence of fine structure, especially near the penetration field, and these jumps will be discussed further in the next chapter.

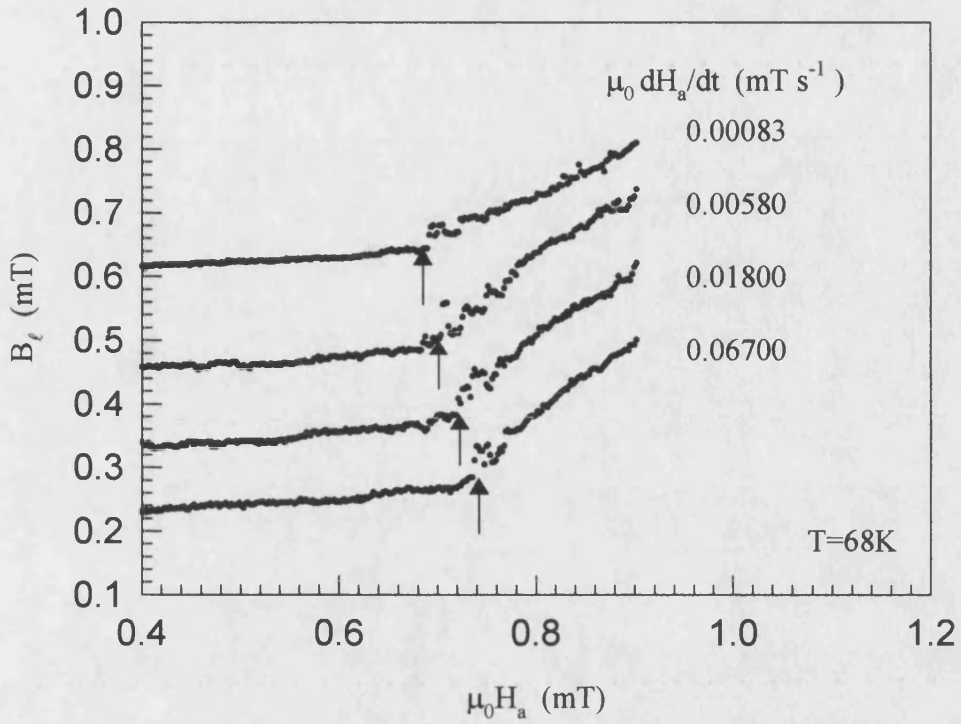

Figure 7.9. Initial magnetisation legs for different field sweep rates at T=68K.

The variation in penetration field with sweep rate for two temperatures is shown in Figure 7.10, and the low sweep rate plateaux observed by Niderőst are clearly visible.

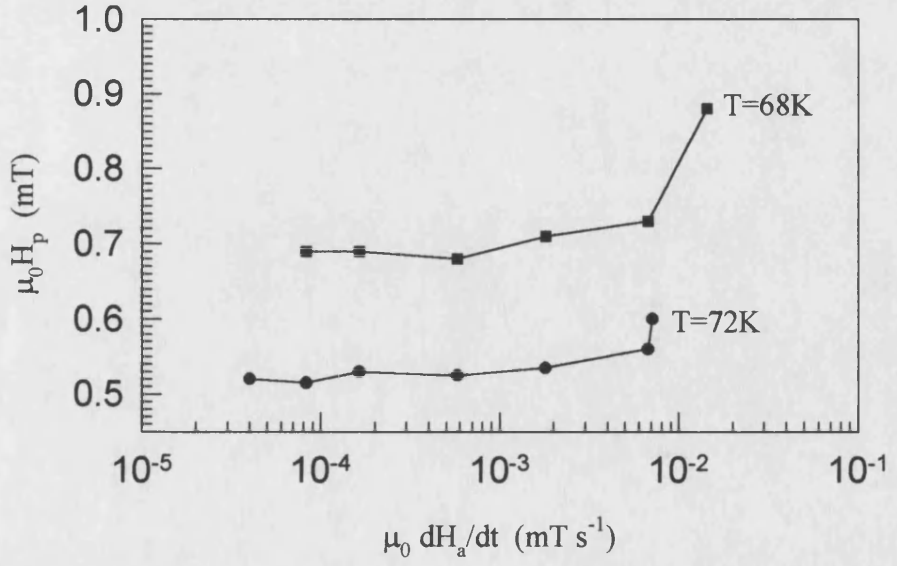

Figure 7.10. Sweep rate dependence of the penetration field, for two temperatures.

The difference between the largest and smallest values of $\vec{H}_P$ decreases as the temperature increases, since higher temperatures produce larger thermal energies which accelerate vortex creep over the B-L barrier. In the plateau region, the system is in equilibrium with respect to surface barriers, and the penetration field is equal to the thermodynamic lower critical field. At these high temperatures, $\vec{H}_P$ saturates to $\vec{H}_{C1}$ at rather fast sweep rates, and this provides a possible explanation for the discrepancy between Burlachkov's model and the high temperature penetration field data described in the previous section. If $\vec{H}_P$ has saturated and the superconductor is in equilibrium with respect to surface barriers then the model is no longer applicable since it is based on thermal activation of vortices over the B-L barrier. Another consequence of a saturated $\vec{H}_P$ is that the penetration depth can be estimated using the G-L expression for $\vec{H}_{C1}$, given by

$$\vec{H}_{C1} \approx \frac{\Phi_0}{4\pi\mu_0 \lambda^2} \ln(\kappa). \tag{7.9}$$

The values of λ_{ab} obtained are shown in Table 7.3, after demagnetisation effects have been accounted for, as described in the previous section.

T (K)	λ_{ab} (nm)
68	182±4
72	209±4

Table 7.3. Penetration depth data for two temperatures, derived from the data above.

7.4 Relaxation over the B-L Surface Barrier

Since the previous experiments have established that the whiskers are dominated by B-L surface barriers, the relaxation theory of Burlachkov described in chapter 3 can be used to investigate the relaxation of vortices over the barrier.

The two types of relaxation experiment performed (shown in Figure 7.11) were first zero-field cooled to ensure the same initial magnetic conditions were used for each measurement. The first measurement (a) is termed relaxation "in", and involves sweeping the external magnetic field up to a measurement field $\vec{H}_m$ and then monitoring the change in internal flux density over a period of time, typically 5000s.

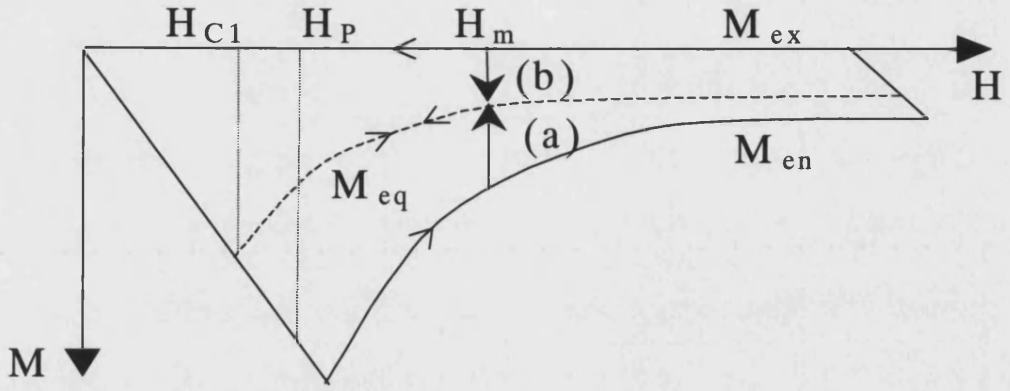

Figure 7.11. Magnetisation Loop showing the equilibrium curve (M_{eq}), and the entry and exit curves (M_{en} and M_{ex} respectively).

The second type of measurement (b), termed relaxation "out", monitors the change in magnetic flux density after the external field has been swept up to a maximum field and then back down to the measurement field.

The relaxation process is a result of the drag force that acts on the vortex core as it passes through the vortex free region at the edges of the superconductor. The origin of the vortex-free region is described in chapter 3 using Clem's model of surface pinning, and is a result of the finite width of the surface barrier where the screening currents flow.

In both the relaxation "in" and "out" case the system moves towards the equilibrium magnetisation M_{eq}, (by flux either exiting or entering the superconductor), which is obtained when the system is in equilibrium with respect to surface barriers.

In the following relaxation measurements, a temperature of 66K was chosen, which was large enough to supply sufficient thermal energy for vortex creep, and

small enough to allow relaxation effects to occur over a measurable time frame. Figure 7.12 shows the applied fields at which vortex relaxation was investigated, for both entry and exit.

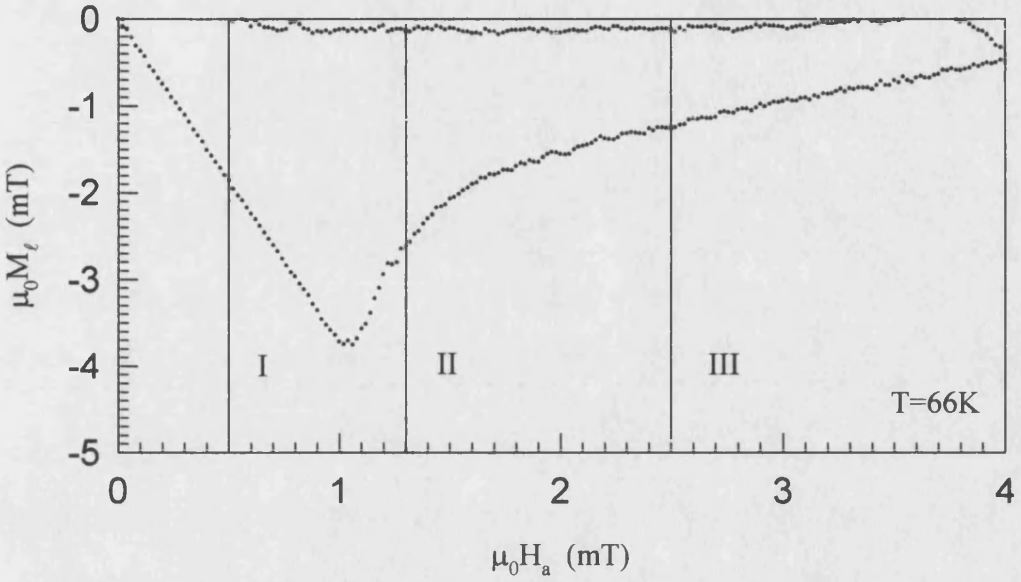

Figure 7.12. The fields at which vortex relaxation, both in and out, was monitored. Fields I to III are described in the text.

At field I, [0.5 mT] the vortices have insufficient energy to overcome the surface barrier so very little relaxation is expected. At field II [1.3 mT] the barrier has collapsed and vortices are free to relax across the vortex-free region and enter the superconductor. At this field, asymmetric relaxation curves should be observed, as described by Clem's theory in chapter 3. Finally, at field III [2.5 mT] the relaxation exit rate should be larger than at field II, since $R \propto \sqrt{B(0)}$.

Figure 7.13 shows relaxation of vortices in and out of a whisker at field I, for two different locations within the whisker – probe 1 is near the centre and probe 2 is nearer the edge.

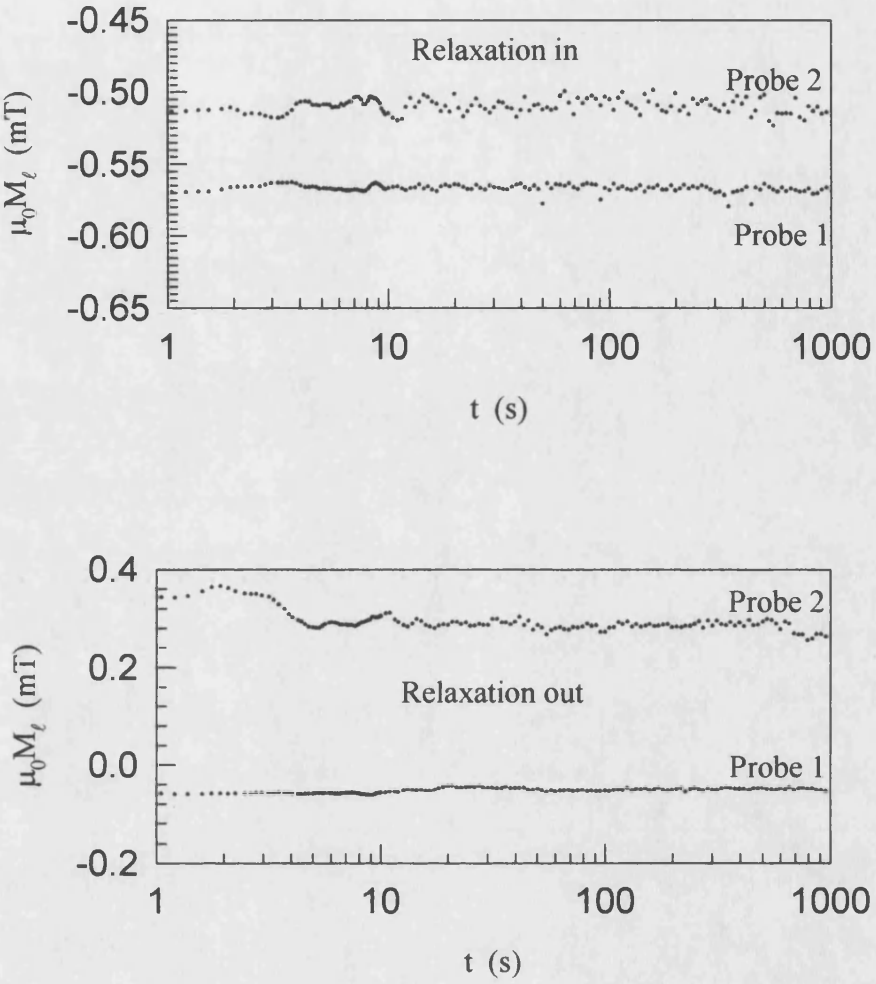

Figure 7.13. Magnetic relaxation in and out of a whisker at an applied field of 0.5mT and a temperature of 66K.

There is evidently very little relaxation into the whisker at this field, since the applied field is less than the penetration field and so the surface barriers have not collapsed. For vortex exit, there is also very little relaxation, since at these low fields the barrier has completely collapsed on the downward leg of the magnetisation loop.

Relaxation into the whisker at 1.3 mT is shown in Figure 7.14, for both probes.

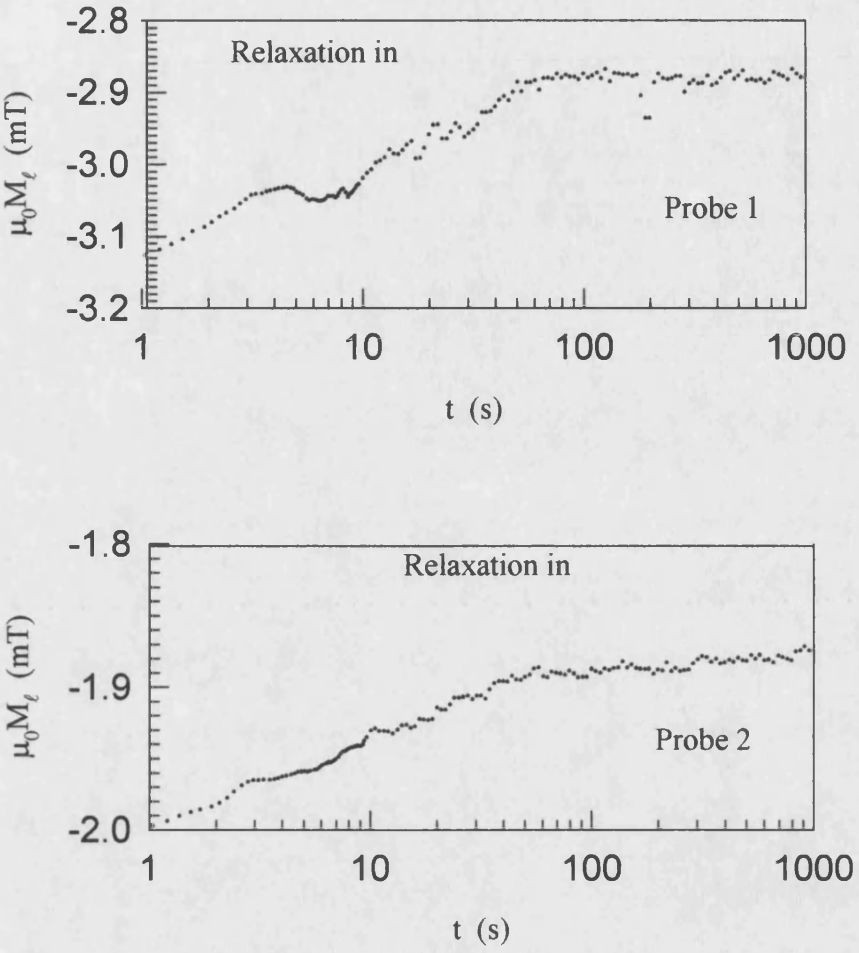

Figure 7.14. Magnetic relaxation into a whisker, at a field of 1.3 mT.

For both whisker locations, the non-linear dependence that is predicted for applied fields greater than the penetration field is clear. The different values of the initial magnetisation (i.e. M(0)) for the two probes reflect the spatial resolution of the array, and shows that the vortex distribution within the whisker is not uniform – the larger magnetisation detected by probe 1 reflects the accumulation of vortices near the centre of the whisker.

The corresponding curves for vortex exit at this field are shown in Figure 7.15 below.

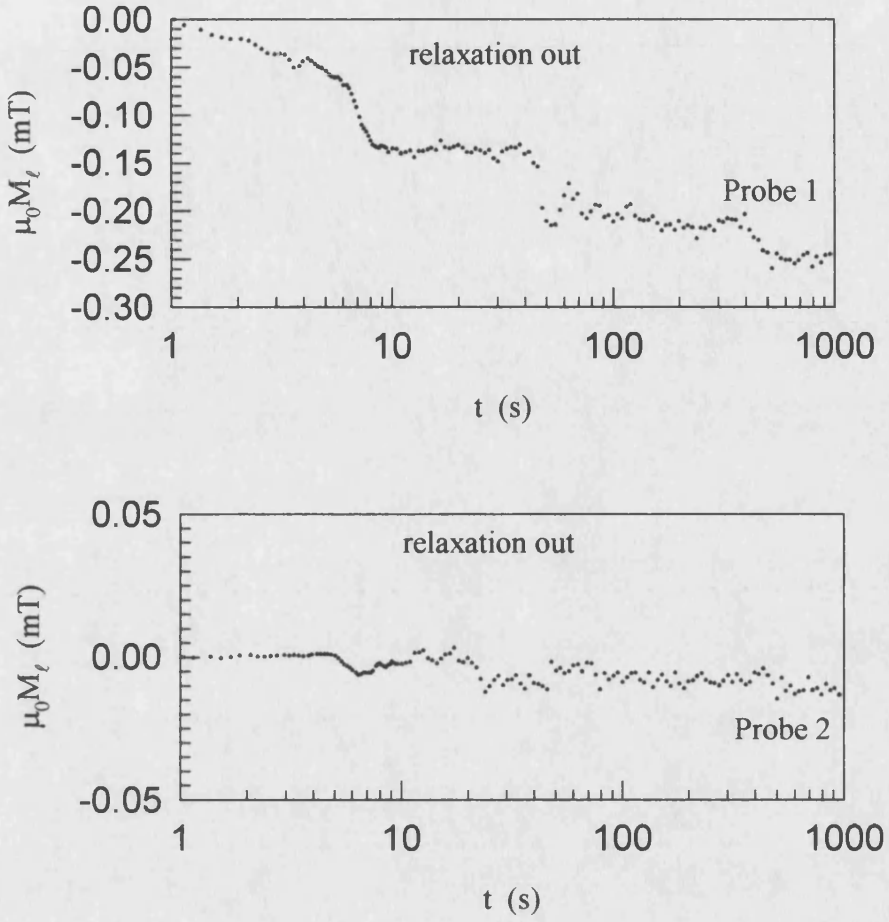

Figure 7.15. Magnetic relaxation out of a whisker at a field of 1.3 mT and temperature of 66K.

In this case, the curves exhibit an approximately logarithmic dependence on time (note the logarithmic ordinate) and the asymmetry between this case and the vortex entry situation provides strong evidence that the surface barriers are of the Bean-Livingston type, rather than geometrical. The difference between the slopes of the relaxation curves for the two probes is a result of the vortex distribution within the whisker, since the vortex exit rate is proportional to the initial value of internal flux density (B(0)) and is given by

$$R_{ex} = \frac{dm}{d\ln(t)} = \frac{2\pi}{\Phi_0 \lambda}\sqrt{\frac{\gamma B(0)}{H_{C1}}}k_B T . \qquad (7.10)$$

The larger slope of probe 1 suggests a greater initial vortex density near the centre of the whisker, in agreement with the dome-shaped flux profile predicted by Burlachkov. Figure 7.16 shows magnetic relaxation over the surface barrier at an applied field of 2.5 mT, for the two probes, with the corresponding curves for vortex exit shown in Figure 7.17.

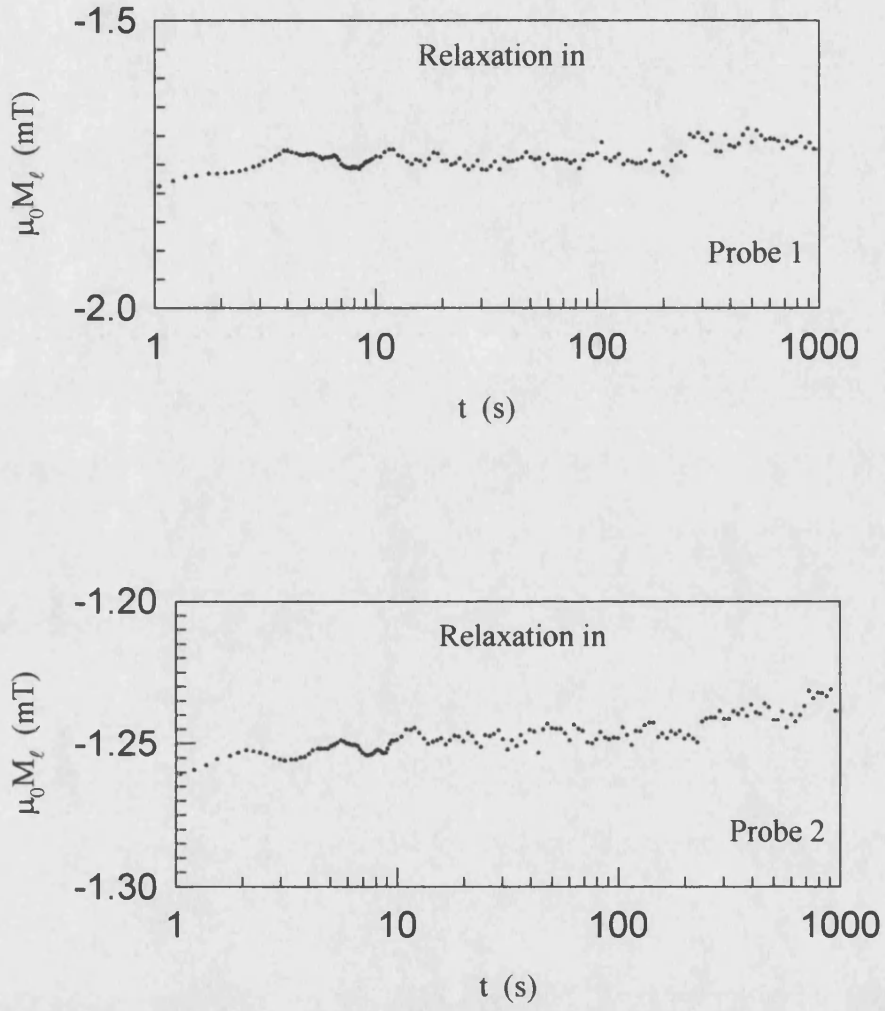

Figure 7.16. Magnetic relaxation over the surface barrier at 2.5 mT.

At the higher field of 2.5mT, the asymmetry between vortex entry and vortex exit is still evident, but not as pronounced as at 1.3 mT, because the relaxation rate is faster.

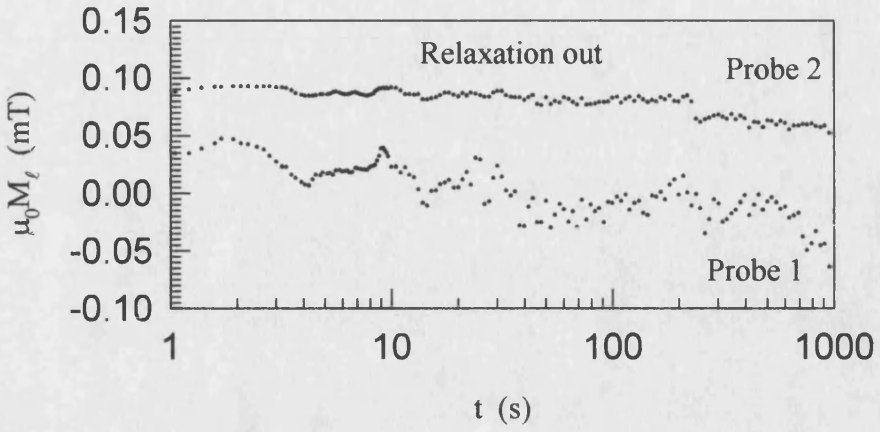

Figure 7.17. Relaxation out of a whisker, at 2.5 mT.

Chapter 8

Internal Vortex Structure

8.1 Flux Profiles

The spatial resolution of Hall arrays has been used to investigate magnetic flux profiles across the width of a whisker. The whisker was aligned normal to the long axis of the Hall bar, as shown in the optical micrograph in Figure 8.1 below,

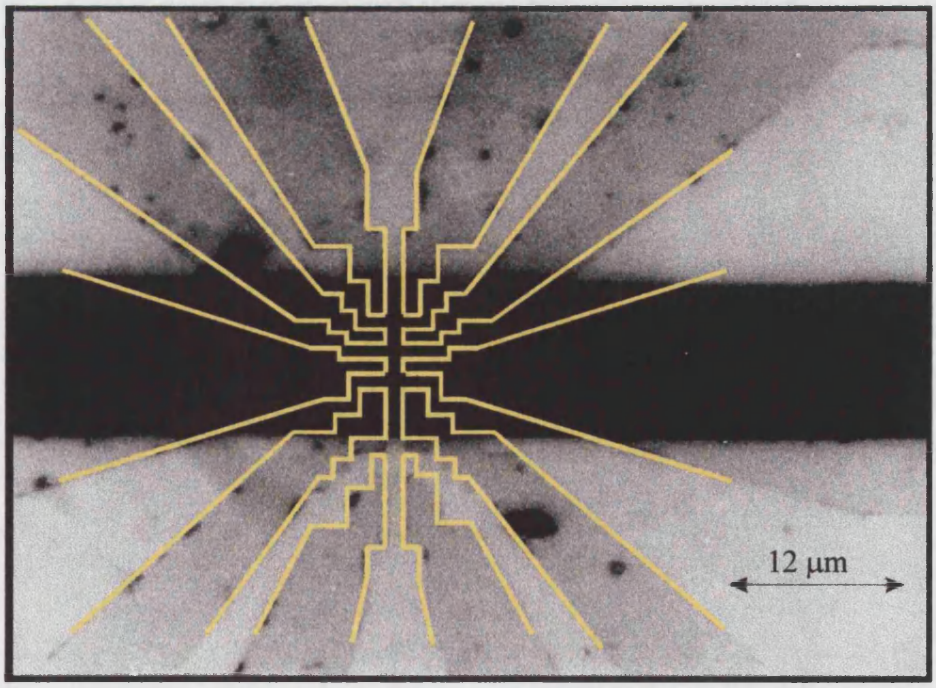

Figure 8.1. Optical micrograph showing a whisker aligned normal to a Hall bar array.

and the lateral dimensions evaluated using an optical microscope calibrated using a known feature size on the chip. This procedure allowed the spatial variation of the local flux density, $\vec{B}_\ell(x)$, to be investigated since the dimensions of both the Hall bar array and the whisker are known.

To check the location of the Hall bar with respect to the whisker, local hysteresis loops were measured at each probe in the array. The probe nearest the edge of the whisker will exhibit flux enhancement due to the Meissner effect, and since this effect is only appreciable very near the edge, its' presence will "locate" the probe with respect to the whisker. The whisker used in this work was (12±2)μm wide and mounted on a 1μm Hall bar, which had a total length (including the width of each probe plus the inter-probe separation) of (9±0.5)μm. This means that the Hall bar array covers well over half the width of the whisker. The initial legs of the zero-field cooled local induction loops are shown in Figure 8.2, with probe #1 closest to the whisker edge.

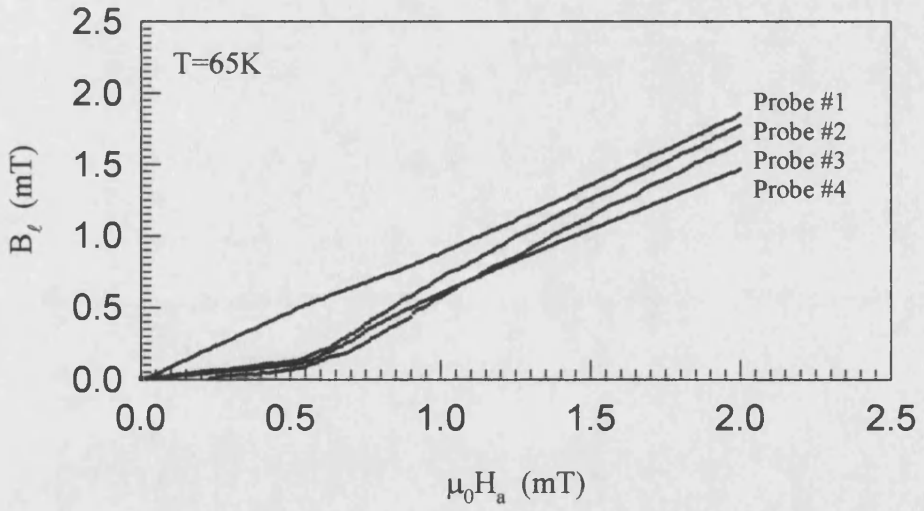

Figure 8.2. Local magnetic flux density versus applied magnetic field for the four probes in the array.

Probe 1 clearly exhibits flux enhancement below the penetration field, thereby fixing it at less than 2μm from the whisker edge. The next probe along is covered by

the whisker, as it exhibits flux expulsion below the penetration field, and the other probe locations can be fixed, assuming probe #1 is at the edge.

Using this information, plots of the vortex distribution across the whisker width can be obtained, and these are shown in Figures 8.3 and 8.4 for applied fields on both the increasing and decreasing legs of the hysteresis loop.

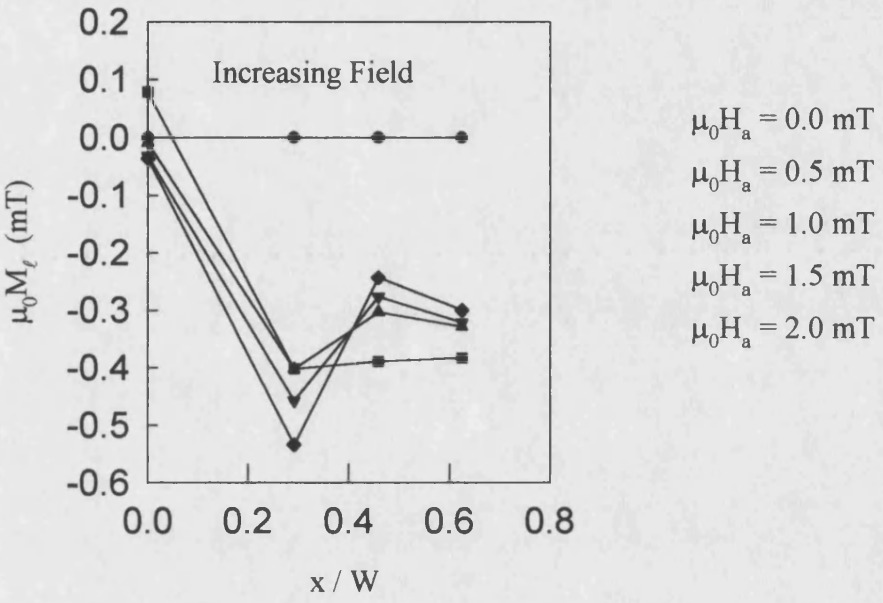

Figure 8.3. Flux profile for various fields on the increasing leg of the hysteresis loop.

The flux profiles show the vortices accumulating in the centre of the whisker, creating a dome-like distribution. This is evident on both the increasing and decreasing hysteresis legs, in contrast to the profiles predicted by either the Bean model, or Brandt's model for thin films, which both predict different profiles for the field increasing and field decreasing case (see chapter 3).

On increasing the field, the 0.5 mT data exhibit no such dome-like profile, since the vortices have only just started to overcome the penetration field. For larger fields the vortices are pushed towards the whisker centre by the Lorentz force (arising from the Meissner screening currents), increasing the height of the dome as the

applied field is increased. When the field direction is reversed, the dome begins to flatten out, with the dome edges extending towards the whisker edge as the vortex density reduces, eventually extending across the entire width of the whisker. At this point, the vortices leave the whisker unhindered and the magnetisation falls to zero.

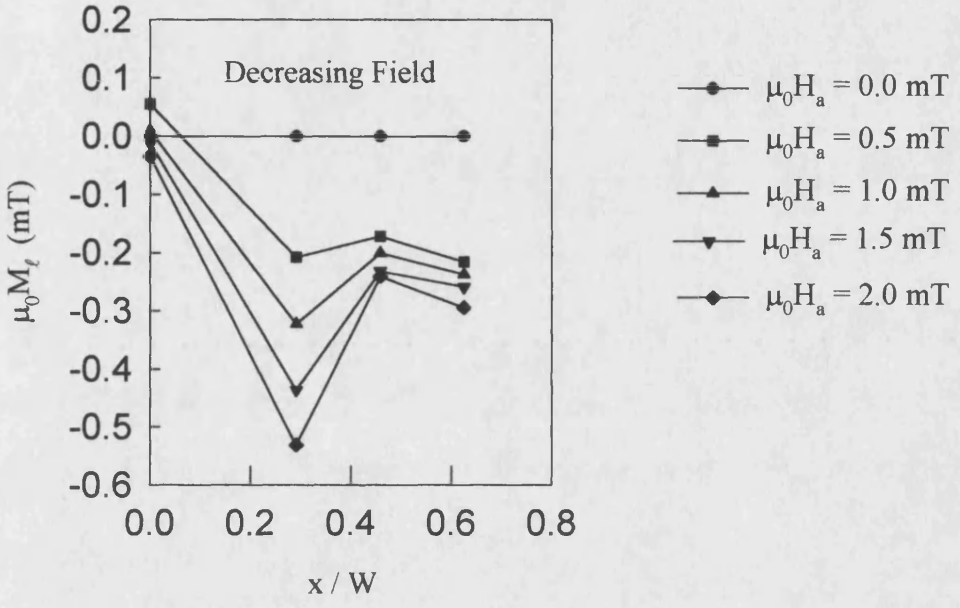

Figure 8.4. Flux profiles for various applied fields, measured on the decreasing leg of the hysteresis loop.

8.2 Field-Cooled Temperature Sweeps

In order to reach a particular point in the phase diagram of a type II superconductor, two paths are commonly used experimentally. In the first case, (path (1) in Figure 8.5) known as zero field cooled field sweeps, the superconductor is first cooled to the measurement temperature from above T_C, and then the magnetic field is swept up to the required field, as shown in Figure 8.5. The other type of experiment is known as a field cooled temperature sweep (path (2) in Figure 8.5), and in this case the required field is applied at a temperature greater than T_C and then the superconductor is cooled to the measurement temperature.

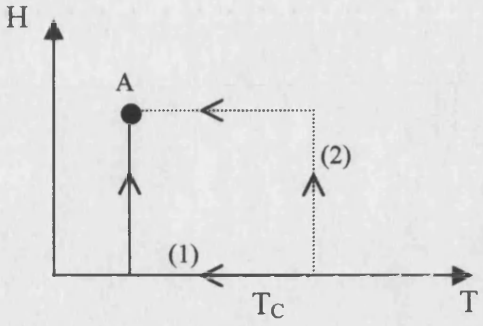

Figure 8.5. Diagram showing the two experimental paths used to reach a point "A" in the H-T plane of a type II superconductor.

In an ideal superconductor, both paths would lead to exactly the same state, whereas in a real superconductor surface barriers (and pinning) can destroy this path independence. Path (1) will be affected by surface barriers, which effectively increase the lower critical field to a penetration field $H_P(T)$, as shown in chapter 7. However, path (2) suppresses the kinetic surface barriers, since vortices are present as soon as the material becomes superconducting (assuming $H > H_{c1}$).

As described in Chapter 2, the mixed state of an ideal type II superconductor is an ordered array of vortices arranged in a hexagonal lattice, similar to an atomic solid. Extending this analogy with atomic crystals, it is plausible that the vortex lattice may melt at high temperatures to form a vortex liquid state, which has no long-range order. This melting transition has been observed in experiments using both field and temperature sweeps, with the signature of melting an abrupt jump in the flux density as the transition line is crossed. The field and temperature dependence of the transition line is in good agreement with the model of Lindemann melting described in Chapter 3, and an example of the phase diagram obtained from temperature sweeps is shown in Figure 8.6.

Temperature sweeps have been carried out on BSCCO whiskers to see if the melting transition occurs in these almost one-dimensional (in flux line terms) samples, and the results are shown in Figure 8.7. The temperature sweeps were carried out using a 2μm array, and the results display an abrupt jump in the local magnetic induction, which is superficially similar to the feature observed at the melting transition in bulk crystals. However, the jumps occur at much smaller fields and are

somewhat larger than those associated with lattice melting (even accounting for the smaller T_C of ≈80K).

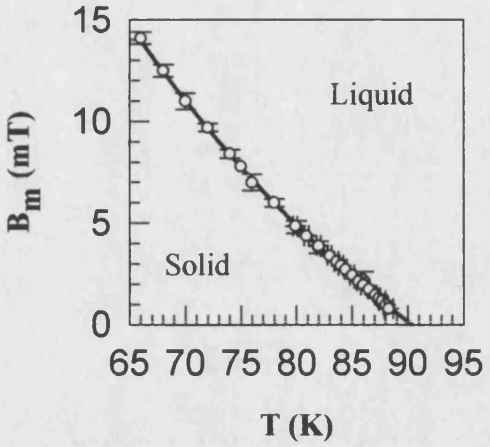

Figure 8.6. Vortex lattice melting line measured on a bulk single crystal of BSCCO, using temperature sweeps at fixed applied field [After Bending, 1998].

The induction jump, marked in Figure 8.7 with an arrow, is defined as the first major discontinuous jump, since some sweeps also exhibit several smaller jumps slightly below the transition, as shown in the 0.4 mT sweep in Figure 8.8.

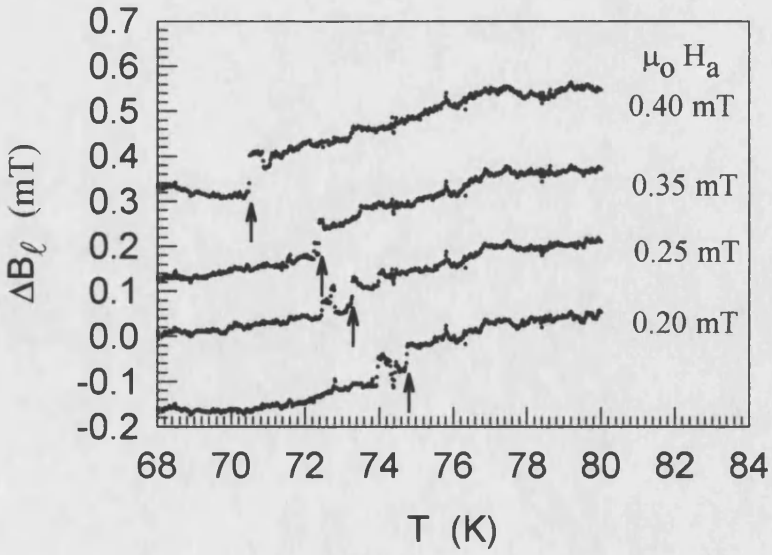

Figure 8.7. Field-cooled temperature sweeps for a BSCCO whisker.

The magnitude of the small jumps is about 20μT, whilst the major jump is 0.1mT, and these values can be converted to flux jumps by multiplying by the active area of the Hall probe, which is $4\mu m^2$. Hence the small jumps correspond to $0.04\Phi_0$ and the large jump corresponds to $0.2\Phi_0$, where Φ_0 is the magnetic flux quantum.

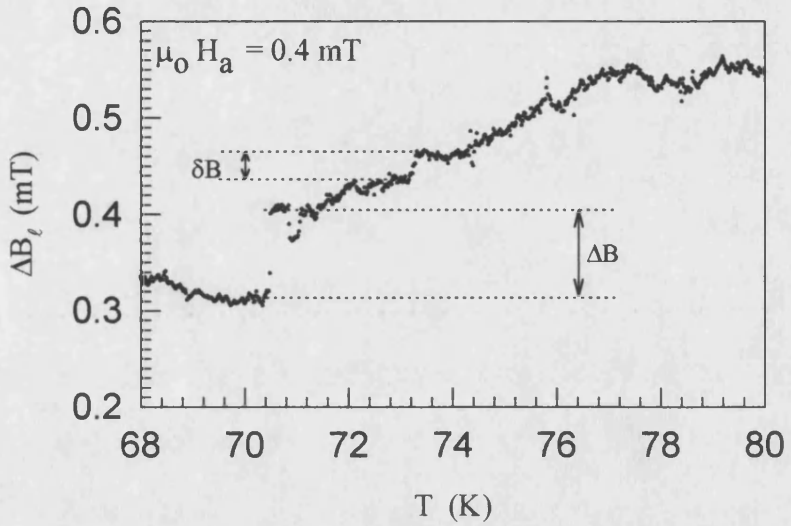

Figure 8.8. Discrete vortex motion near the PIJ for the 0.4mT sweep.

The fact that the jumps are somewhat smaller than a single flux quantum suggests they are the result of vortex motion near the active sensor area, rather than vortices entering or leaving the whisker.

Using the field and temperature dependence of the principle induction jump (PIJ) defined in Figure 8.7, a phase diagram can be constructed in the H-T plane, as shown in Figure 8.9. Although superficially similar to the melting line observed in bulk crystals, the fields at which the PIJ occurs are orders of magnitude smaller, and the curvature of the line is completely different (compare with figure 8.6). These large discrepancies between the PIJ data and the well reported melting in bulk BSCCO crystals suggest vortex solid melting is not the correct picture of what is happening (vortex decoupling also appears unlikely for the same reasons). Also, the width of the whisker is so small that at the low flux densities associated with the PIJ the vortex separation a_0 is 2.5-5.0 μm. Hence only one or two rows of vortices can be expected along the whisker and the problem is almost one-dimensional. This means that the detailed statistical mechanics will be completely different to that of bulk crystals.

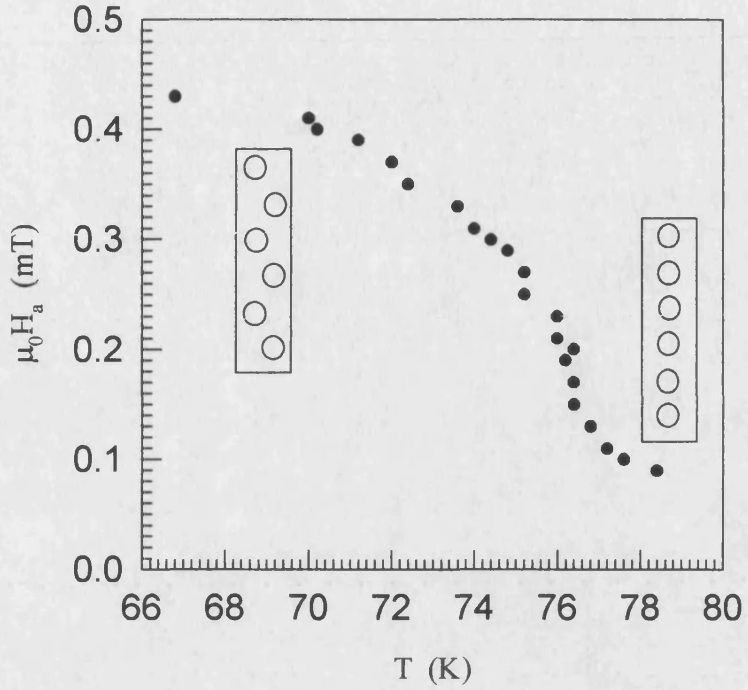

Figure 8.9. Location of the PIJ data in the H-T plane. Two possible vortex configurations are shown.

The most likely explanation for the PIJ is a transition between a high local vortex density configuration (such as a linear chain state) and a low-density configuration (Such as a zigzag state), as shown in Figure 8.9.

Figure 8.10 shows how the jump amplitude varies along the transition line.

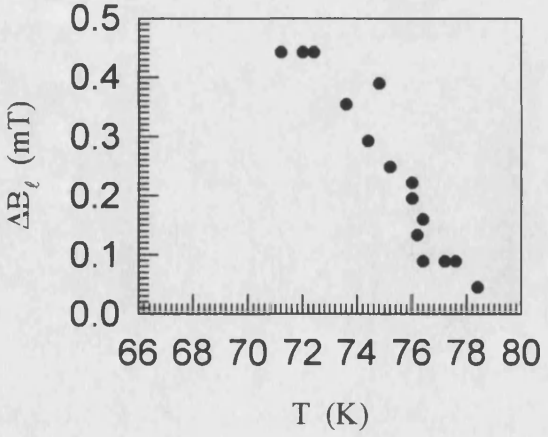

Figure 8.10. Magnitude of the PIJ as a function of temperature.

It is clear that the jumps become larger with decreasing temperature (or increasing field), approximately following the shape of the transition line and possibly reflecting the temperature dependent penetration depth. This suggests that there are slightly different vortex arrangements within each regime, with the low field, high temperature region giving the vortex chain state and the high field, low temperature region giving the zigzag state, as shown in Figure 8.9. The probable origin of the change in vortex configuration is the interplay between repulsion from surface barriers, leading to the linear chain state, and the inter-vortex repulsion, which favours the zigzag configuration. Hence, as the whisker is cooled through T_C in the presence of a magnetic field, the vortices initially accumulate at the centre under the influence of surface barriers, and then suddenly switch to the zigzag state (at the transition line) when the inter-vortex repulsion first outweighs the surface contribution. The fact that no jumps are observed above ~0.5mT suggests abrupt temperature dependent transitions between multi-row structures either do not occur or are difficult to resolve.

8.3 Matching Fields in Local Magnetisation Data

Close inspection of the initial magnetisation leg often reveals discrete, sawtooth structures, as shown in Figure 8.11.

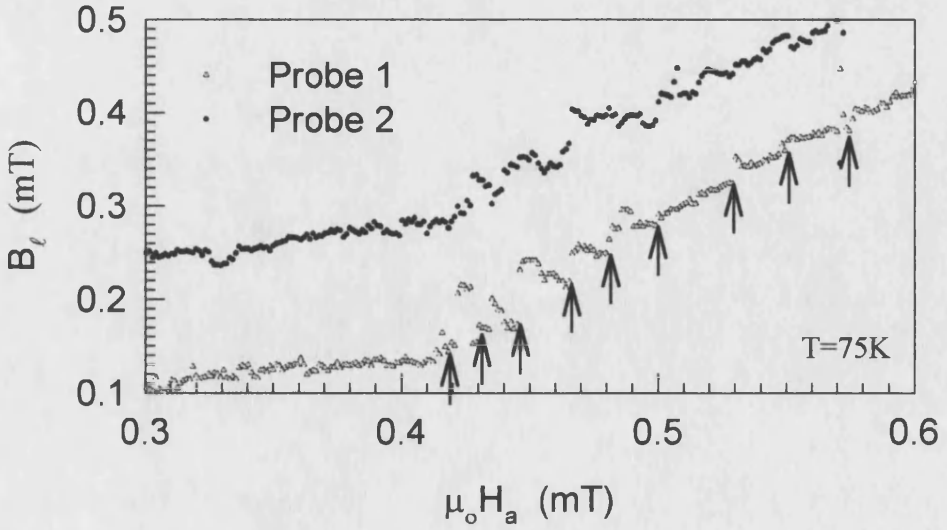

Figure 8.11. Discrete sawtooth structures evident in the initial magnetisation leg.

Probes 1 and 2 were in slightly different positions with respect to the whisker, with probe 2 near the centre and probe 1 near the edge.

The sawtooth structure is reminiscent of the "matching field" structure, observed by Zeise et al. [1996] in a thin film of BSCCO with a magnetic field applied parallel to the film. Zeise found discrete dissipation maxima in the critical current at matching fields B_N in the irreversible region of the magnetic phase diagram. These matching fields have been interpreted as changes in the vortex configuration, with each matching field corresponding to a new row of vortices entering the film.

To demonstrate that it was not simply local vortex motion that was giving rise to the jumps, a 4μm Hall bar was used to make the same measurements. Figure 8.12 below shows that although much smaller, the jumps are still evident. Since a 4μm bar is not small enough to detect single vortex motion, the jumps must be related to vortex configuration rearrangements. This is emphasised by the fact that the 2μm Hall bar measurements exhibit "up" and "down" jumps, but the 4μm Hall bar measurements only show "up" jumps. This is because the smaller Hall bars are sensitive to the exact vortex positions (the *local* vortex density can go up or down as the vortices move around the active area of the Hall bar) but the 4μm probe averages over several vortices, thereby smearing out any local effects.

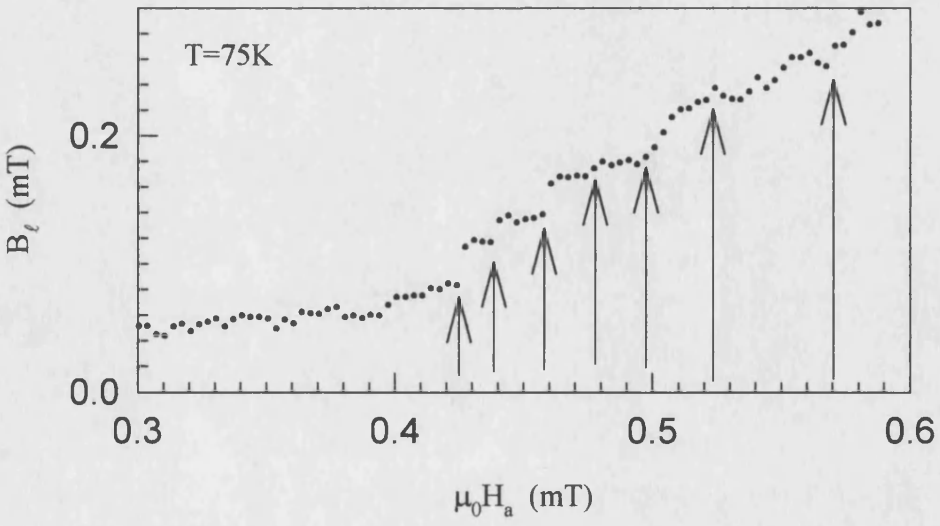

Figure 8.12. Vortex jumps measured with a 4μm Hall bar array.

We believe that the origin of the sawtooth structure is the interplay between surface barriers and the vortex-vortex repulsion. Above the penetration field, the vortices are initially forced into a single row along the length of the whisker by the surface barriers, as shown in Figure 8.13a. As the applied field is further increased, the vortices within the row become more closely spaced, increasing the inter-vortex repulsion until, at a matching field $\vec{H}_N$ the single row configuration becomes energetically unstable and the system "jumps" to two, less densely packed rows (fig 8.13b).

As the field is increased further, the two row system eventually becomes energetically unstable, and at a new matching field $\vec{H}_{N+1}$ "jumps" into three rows, as shown in Figure 8.13c.

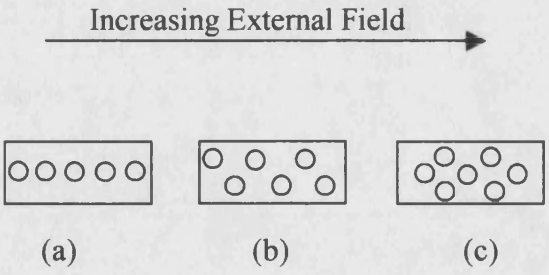

Figure 8.13. Change in vortex configuration with increasing applied field.

This cycle continues until the applied field is equal to the upper critical field when the cores begin to overlap, but in practice the jumps become indistinguishable above about 15-20 rows because the jump magnitude eventually becomes lost in the noise.

The theoretical model of this system described in Chapter 3 is not in quantitative agreement with experimental observations, primarily because the model is based on a magnetic field applied parallel to the plane of a superconducting film, which is completely different to the perpendicular geometry described here.

Chapter 9

Transport Measurements

9.1 Model of Surface Pinning

The effect of magnetic fields on critical currents in bulk superconductors has been widely studied, with the principle consequences being a broadening of the superconducting transition and a reduction of the maximum critical current. The origin of both effects is vortex motion, since energy is required to move vortices, and this leads to dissipation and hence resistance below T_C. The two principle mechanisms for vortex motion are flux creep and flux flow. During flux creep, thermal activation of the vortices causes them to "hop" from one pinning site to another. In the case of flux flow, the transport current causes a Lorentz force that is larger than the pinning force f_p, leading to transverse vortex motion.

In the ideal case of zero bulk pinning centres, vortices will enter the whisker (if $\vec{H}_a > \vec{H}_{C1}$) and be swept towards the edge by the Lorentz force, and then annihilate with their images, thus creating a steady state. The only force opposing vortex motion in this ideal case is viscous drag on the normal cores, and equating this drag force to the driving force the magnitudes are found to be related by

$$J\Phi_0 = \eta v_L, \tag{9.1}$$

where η is the coefficient of viscosity and v_L the vortex velocity.

Using the relation $\vec{E} = \vec{B} \wedge \vec{v}_L$, it can be shown [Bardeen, 1965] that the flux-flow resistivity, ρ_{ff}, is given by

$$\rho_{ff} = \frac{|\vec{E}|}{|\vec{J}|} = \frac{|\vec{B}|\Phi_0}{\eta}. \tag{9.2}$$

i.e. in the flux flow regime, the resistivity is proportional to the applied field.

The effect of surfaces is often neglected when investigating transport properties, since in bulk crystals vortex motion is dominated by bulk pinning. However, in whiskers, bulk pinning can be very small and the large surface-to-volume ratio means that surface pinning effects become important.

Benkrauda and Clem [Benkrauda *et al.*, 1998] have derived expressions for the magnetic field dependence of the critical current, $I_C(H_a)$, for a system dominated by surface pinning, and their work will be reviewed here. The geometry used in this work is shown in Figure 9.1, and the ratio $R = \sqrt{\frac{2W}{d}}$ ensures that the large demagnetisation effects are accounted for.

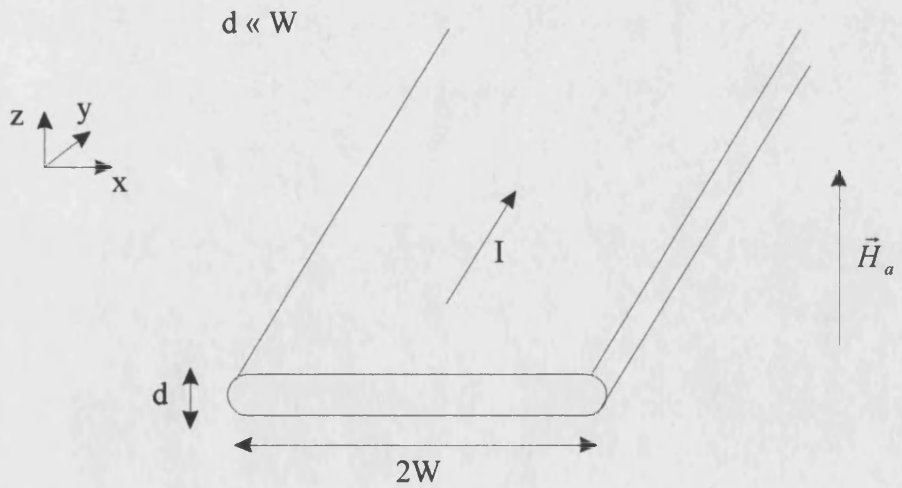

Figure 9.1. Geometry used in the model of surface pinning described below.

Benkrauda *et al.* [1998] have shown that the flux profile across a strip of superconductor which is dominated by surface barriers is given by

$$B_Z(x) = \mu_0 H_a \frac{\sqrt{(x-a)(b-x)}}{\sqrt{W^2 - x^2}}, \tag{9.3}$$

where the dome extends from x=a to x=b, and outside the dome B_Z=0. The parameters a and b are given by

$$a = W\left[\frac{I}{2\pi W H_a} - \sqrt{\left(1+\frac{I}{2\pi W H_a}\right)^2 - \left(\frac{H_S - H_a}{R H_a}\right)^2}\right] \tag{9.4a}$$

and

$$b = W\left[\frac{I}{2\pi W H_a} + \sqrt{\left(1+\frac{I}{2\pi W H_a}\right)^2 - \left(\frac{H_S - H_a}{R H_a}\right)^2}\right]. \tag{9.4b}$$

In these expressions, H_S is the penetration field, so that $H_S/(1+R)$ is the applied field at which vortices begin to enter, and R accounts for demagnetising effects in the planar geometry. Figure 9.2(a) shows the vortex distribution for different values of I at H_a = H_S / 10, with R=10.05. With no transport current applied (I=0), the dome is centred in the middle of the strip, but as I is increased the dome shifts to the right as vortices collect near the right-hand edge due to the influence of the Lorentz force. Finally, when $I=I_C$ the dome reaches the edge of the strip and the vortices are no longer pinned by the surface barriers, which allows vortex motion and gives rise to resistance. The corresponding current density distribution is given by

$$J_Y(x) = \frac{2H_a}{d}\frac{\sqrt{(b-x)(a-x)}}{\sqrt{W^2 - x^2}} \tag{9.5a}$$

in the region $-W < x < a$,

$$J_Y(x) = \frac{-2H_a}{d} \frac{\sqrt{(b-x)(a-x)}}{\sqrt{W^2 - x^2}} \qquad (9.5b)$$

in the region b < x < W, and zero everywhere else, and is shown in Figure 9.2(b) for the same parameters.

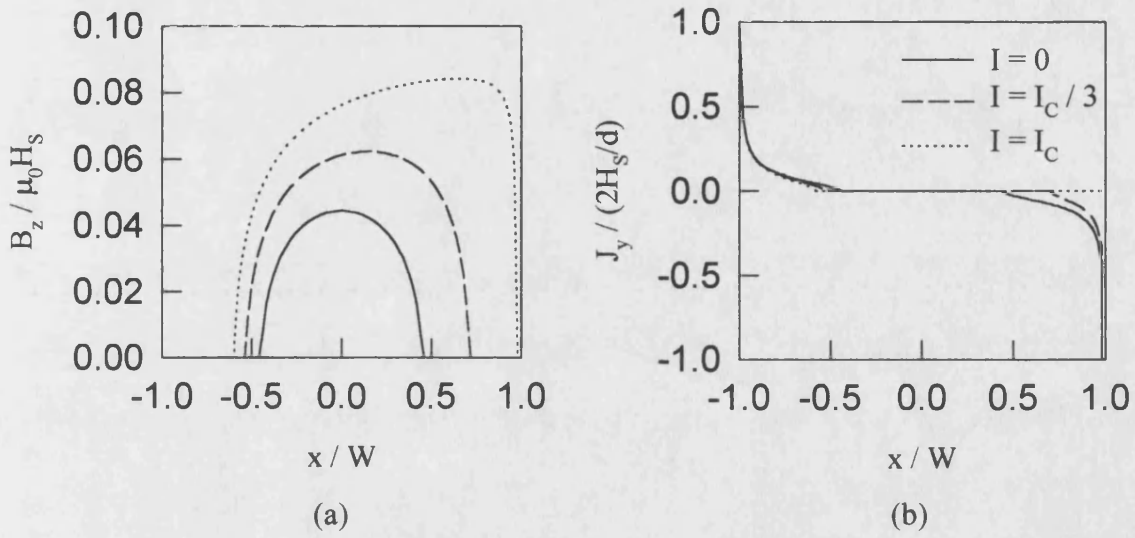

Figure 9.2. Flux profiles (a) and current density distribution (b) for various values of transport current. Parameters used were R=10.05 and H_a=H_S/10 [After Benkraouda, 1998].

As the transport current is increased, the range of fields for which the dome profile is stable becomes smaller, until at a critical current, I_{cd}, the dome disappears entirely. Similarly, as the applied field is reduced, the dome becomes unstable at a critical field H_{cd}, and these critical points are given by

$$I_{cd} = 2\pi H_S \frac{W}{2R+1} \qquad (9.6)$$

and

$$H_{cd} = \frac{H_S}{2R+1}. \tag{9.7}$$

For $I < I_{cd}$ and $H_a \geq H_{cd}$, there is a stable dome profile across the strip and a finite critical current, and the field dependence is given by

$$I_C(H_a) = \frac{\pi W H_S}{R^2}\left(\frac{H_S}{2H_a} - 1\right) \qquad H_{cd} \leq H_a \leq \frac{H_S}{2} \tag{9.8}$$

For fields greater than $H_S / 2$, the vortices overcome surface pinning and the critical current collapses to zero. For fields smaller than H_{cd}, the strip remains in the Meissner state and the critical current is then given by

$$I_C(H_a) = I_C(0) - 2\pi H_a \frac{R+1}{R}, \tag{9.9}$$

with $I_C(0)$ given by

$$I_C(0) = 2\pi \frac{W H_S}{R}. \tag{9.10}$$

The field dependence of I_C in the range $0 < H_a < H_S / 2$ is shown in Figure 9.3, with the shaded region indicating a stable dome profile.

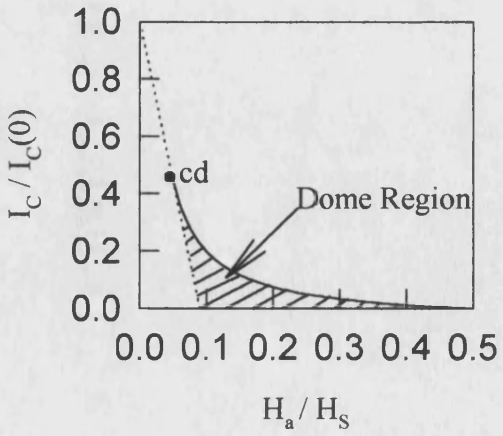

Figure 9.3. Field dependence of the critical current, showing the dome region and the critical point (cd).

Using typical values for a whisker of width 2W=25μm and thickness 0.3μm, giving a demagnetising factor R=6, the barrier field H_S can be estimated from the measurement of the penetration field in hysteresis loops. Typical values near T_C are $\mu_0 H_P \approx 0.1$ mT, which gives a value of $\mu_0 H_S = (1+R)\mu_0 H_P = 0.7$ mT. Using these estimates, the values of I_{cd} and $\mu_0 H_{cd}$ are estimated (using 8.6 and 8.7) as 1.6mA and 0.1 mT, respectively.

9.2 Current-Voltage Measurements

Current-voltage traces were measured on the contacted whiskers, to investigate the critical current I_C (the current at which resistance first appears in the superconductor) and its dependence on temperature and applied magnetic field. The curves were obtained with the circuit in figure 9.4, using a Keithley 220 current source to sweep the current, and a Keithley 182 nanovoltmeter (and a home-made 1000 gain low-noise amplifier) to monitor the voltage drop across the whisker.

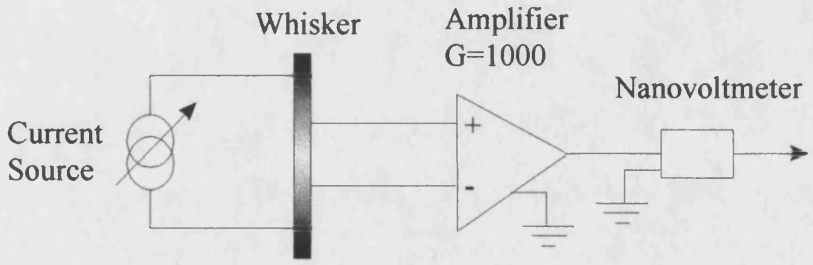

Figure 9.4. Measurement circuit for I-V characteristics, using four contacts on the whisker.

The current was swept logarithmically because I_C can change by orders of magnitude as the temperature or magnetic field is varied, so the values of I_C have a relatively large error of about ±1.0μA associated with them. In order to define a critical current, it was necessary to decide on a zero voltage criterion, and this was

chosen to be 0.05μV, which corresponds to the minimum detectable voltage of the nanovoltmeter (accounting for the very poor SNR of the system, due mainly to Johnson noise arising from the contacts, which had quite large resistances of about 150Ω.

For the magnetic field measurements, the geometry shown in the previous section was used, with the field applied parallel to the crystallographic $\vec{c}$ axis and the transport current applied along the length of the whisker. It should be noted, however, that effects such as offset contacts and the extreme anisotropy of BSCCO have been shown to lead to anomalous voltage reversals [Aukkaravittayapun, 1996] and the model of surface pinning described above assumes perfect electrical contacts.

The lateral dimensions of the whiskers were found using a calibrated graticule on an optical microscope, and the thickness was determined using a talystep surface profiler.

9.3 Results and Discussion

Figure 9.5 shows some I-V curves obtained at various temperatures with no magnetic field applied. The onset of resistance occurs when the curves first deviate from the zero slope of the superconducting phase, and this is indicated with an arrow.

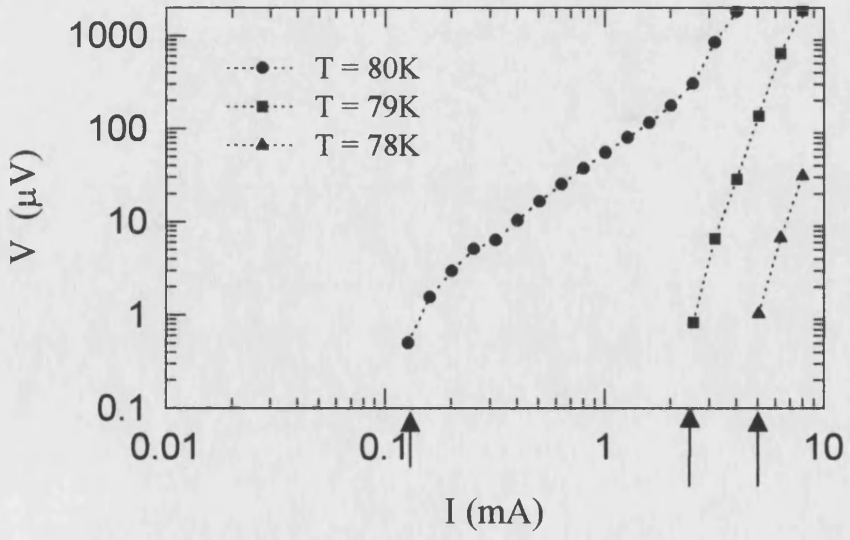

Figure 9.5. Current-Voltage curves in zero applied field, at different temperatures.

Lower temperatures were not measured because the large critical current would have destroyed the delicate contacts, which could not support currents greater than about 10 mA.

The effect of applying a magnetic field is shown in Figure 9.6, where the magnetic field is varied between 2.5mT and 20mT. The raw data shown in these graphs is used to derive the field dependence of the critical current.

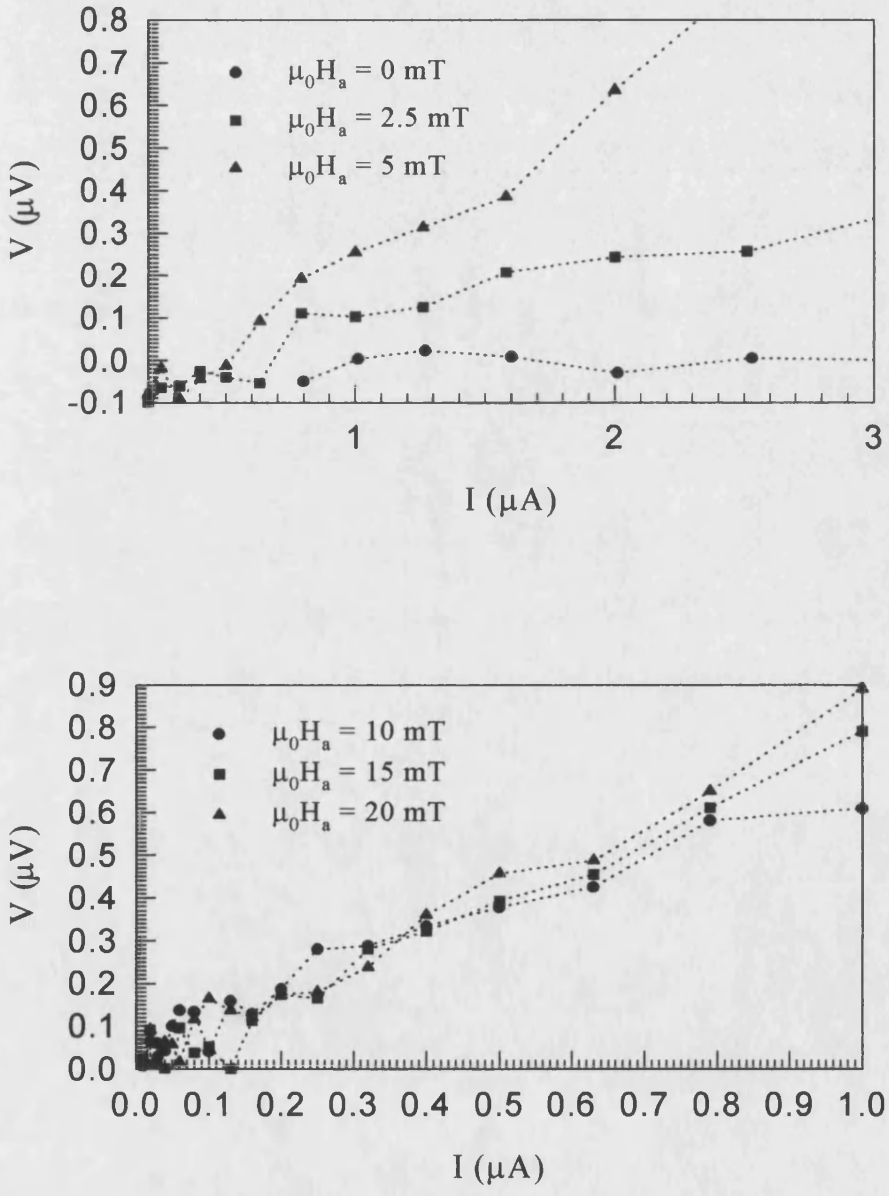

Figure 9.6. Effect of applied magnetic field on current-voltage curves for a BSCCO whisker, measured at T=80K.

The flux-flow resistance can be calculated from the slope of the I-V traces above the critical current, and this is shown in Figure 9.7.

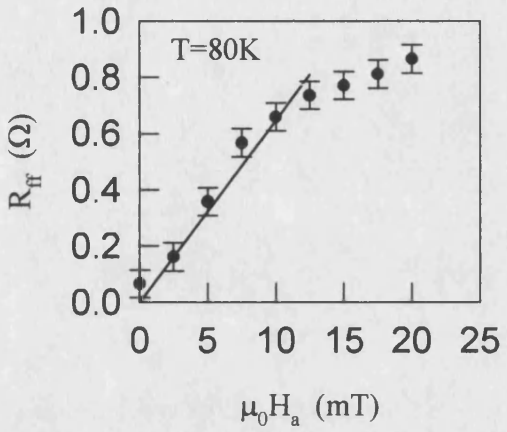

Figure 9.7. Variation in the resistance of a whisker with applied field.

For fields below $\mu_0 H_a$=12mT, the flux-flow resistance R_{ff} is proportional to the applied field, showing that the whisker is in the flux-flow regime. Above this value, there is a pronounced saturation of the resistance, indicating a different regime. The variation of critical current with magnetic field is shown in Figure 9.8.

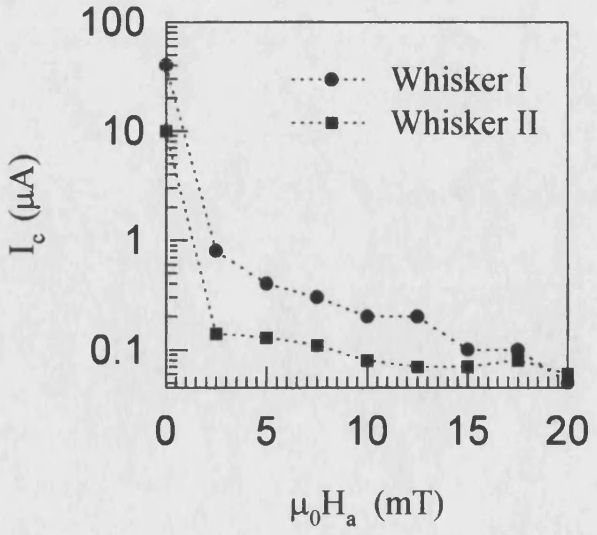

Figure 9.8. Variation of critical current with field for two whiskers, measured at 80K.

It is clear that magnetic fields have a very large effect on the transport properties of the whisker, reducing the critical current by nearly two orders of magnitude from the zero-field value.

To fit the high field data ($\mu_0 H_a$>0.25mT) to the model, the data are re-plotted in Figure 9.9, with the regression lines indicating the fit.

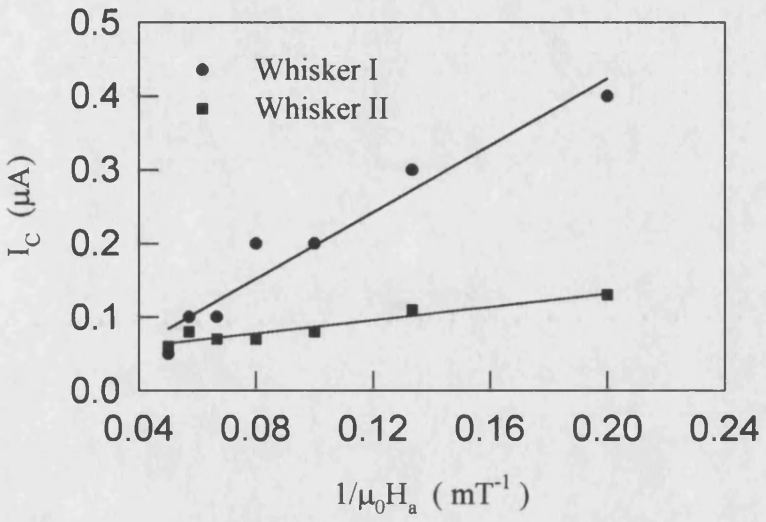

Figure 9.9. Fit of the data in Figure 9.8 to the surface pinning model.

The slopes of the regression lines, determined from a least-squares fit, give the fitted value of H_S, the barrier field corrected for demagnetising effects. Using this value of H_S, and using reasonable estimates of R=6 and W=12μm, values of the critical parameters for the dome-profile, I_{cd} and H_{cd}, are obtained, and these results are shown in Table 9.1.

Whisker	Slope (μA mT)	Intercept (μA)	$\mu_0 H_S$ (mT)	I_{cd} (μA)	$\mu_0 H_{cd}$ (mT)
I	1.8×10^{-3}	-0.029	0.10	240	0.10
II	3.6×10^{-4}	-0.041	0.04	104	0.24

Table 9.1. Values of the fitted parameters for two whiskers, measured at 80K.

All the fitted values are in good agreement with the estimated values, showing that the model of surface pinning describes the transport properties of these whiskers very well. Also, since the model excludes bulk pinning, the whiskers must be dominated by surface pinning, although this data does not allow one to distinguish between B-L barriers and geometrical barriers.

Chapter 10

Preliminary Irradiation Results

10.1 Irradiation of Superconductors

Many groups have attempted to obtain a microscopic understanding of pinning in superconductors by the deliberate introduction of artificial pinning centres. This is often achieved with heavy ion irradiation, which leaves damage tracks as the ions pass through the superconductor, creating pinning sites. This technique has been used to increase the vortex pinning (signified by increased hysteresis width in magnetisation measurements) of bulk single crystals by many workers [See, for example, Civale, 1991]. However, Konczykowski [1991] observed a decrease in the hysteresis width of very clean, irradiated BSCCO crystals, and this was interpreted as evidence of pinning by surface barriers, which are strongly affected by relatively small imperfections in the crystal surface.

To test this observation in very clean, single crystals, some of our whiskers were irradiated with 10 MeV electrons (with a density of 10^{18} e cm^{-2}) and the hysteresis loops of the same samples before and after treatment compared.

10.2 Hysteresis Loops

Figure 10.1 shows the effect of irradiation on local magnetisation loops at low temperatures. The most striking effect is that the degree of hysteresis actually reduces after irradiation, which corresponds to a decrease in pinning.

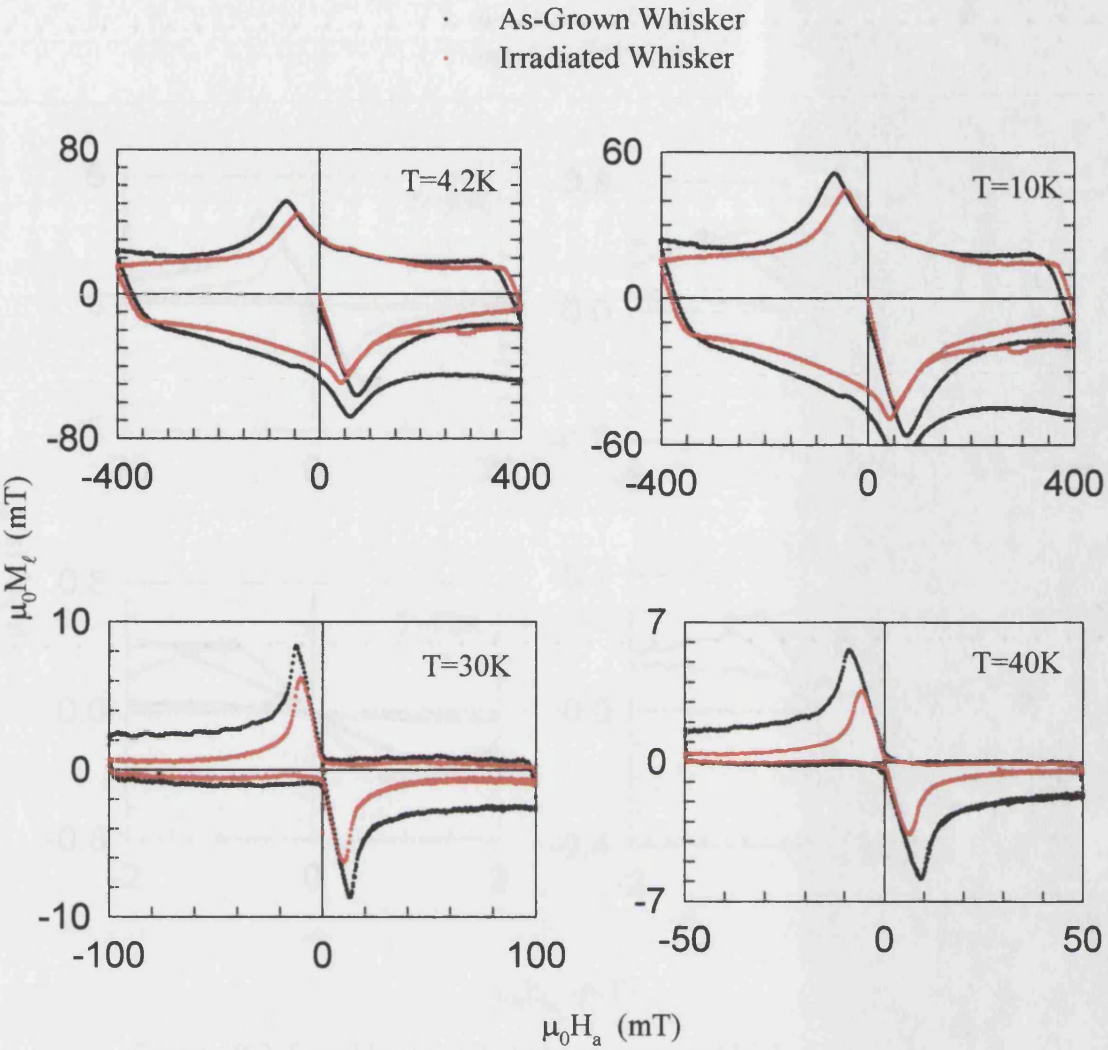

Figure 10.1. Local hysteresis loops before and after electron irradiation, for low temperatures.

This is in contrast to at least one study carried out on bulk crystals, which shows a strong increase in pinning due to defects caused by irradiation [Civale, 1991]. The high temperature data in Figure 10.2 shows that the hysteresis actually disappears in irradiated whiskers above 70K, as thermal activation enables the vortices to overcome the suppressed surface pinning effects of the surface barrier.

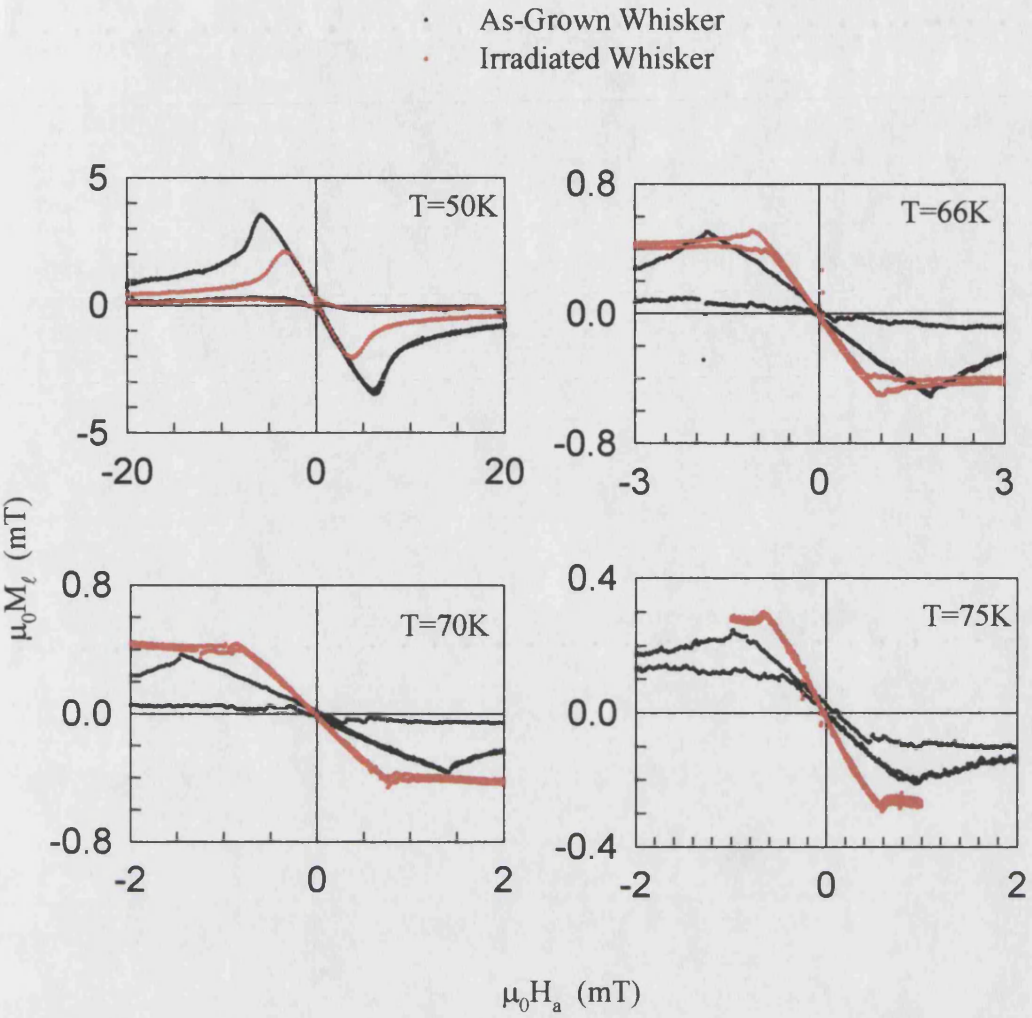

Figure 10.2. Local hysteresis loops measured at high temperatures.

The temperature dependence of the penetration field, which falls sharply after irradiation, is shown in Figure 10.3. The fact that $H_P(T)$ extrapolates to approximately the same value of T_C (about 80K) suggests that the effects described above are not simply the result of a reduction in T_C as a result of the irradiation (although it is a difficult extrapolation).

The penetration field data still exhibit the exponential dependence on temperature at low temperatures predicted by the model of thermal activation of pancake vortices over a surface barrier, which suggests that the barrier has been reduced, but not destroyed, as may be expected from the relatively low energy of electron radiation. These experiments provide strong evidence that pinning in whiskers is caused by surface barriers, which are strongly reduced (leading to almost

reversible magnetisation at high temperatures) by electron irradiation, in contrast to some experiments on bulk crystals which show an increase in pinning.

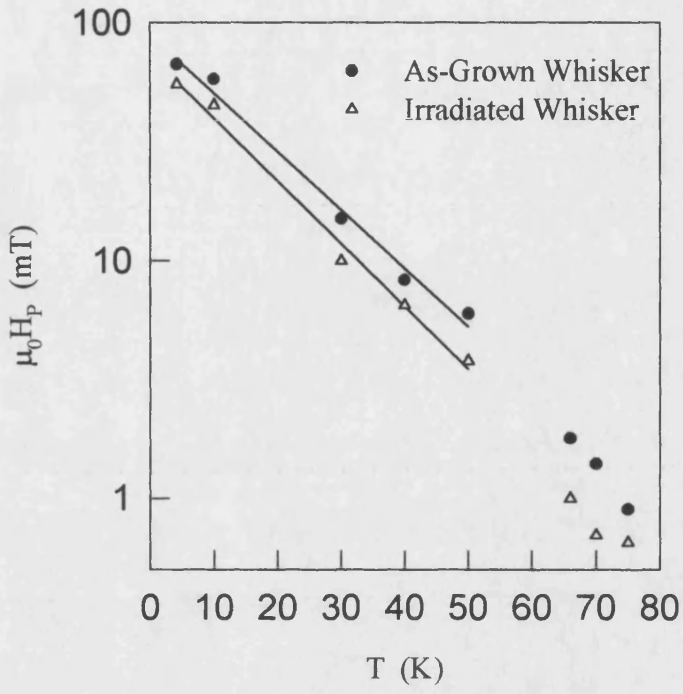

Figure 10.3. Temperature dependence of the penetration field before and after irradiation.

Chapter 11

Conclusions and Further Work

11.1 Whiskers as Model Systems

A range of micron sized Hall probe arrays have been used to carry out a detailed study of the effects of surface barriers in superconducting BSCCO whiskers. The absence of any significant remanent magnetisation at temperatures above 10K demonstrates the lack of bulk pinning, and shows that the hysteresis must be a result of surface pinning. Also, the shape of the hysteresis loops (above 10K) is consistent with a system dominated by surface barriers, with very small magnetisation on the return leg of the hysteresis cycle.

Magnetic relaxation measurements show significant vortex creep over the surface barrier, with the time dependence of the magnetic relaxation in agreement with a model suggested by Burlachkov [1993]. These measurements show that the surface barrier is of the Bean-Livingston type, rather than the geometrical barrier, which is not predicted to exhibit any significant relaxation effects.

Electron irradiation of the whiskers appears to reduce both the hysteresis width and the field of first flux penetration, in contrast to many other irradiation experiments, which show the opposite effect. This is further evidence of a surface barrier dominated system, since the relatively low-energy electrons damage the surfaces and suppress the surface barrier, but otherwise introduce only relatively weak pinning point defects. All these experiments, together with the large surface-volume ratio of the whiskers, are strong evidence for whiskers being dominated by surface effects.

11.2 Effects of Surface Barriers

Using the evidence described above, whiskers have been used as model systems to investigate the effects of the Bean-Livingston surface barrier (B-L s b) on vortex penetration and subsequent dynamics.

Measurement of the temperature dependence of the penetration field and comparison with Burlachkov's model of flux creep over the B-L s b [Burlachkov, 1998] has shown that there are two regimes for vortex penetration. At low fields ($\mu_0 H_a$<5 mT), penetration occurs via thermal activation of three-dimensional vortex lines over the surface barrier. At higher fields, the vortex lines decouple into weakly correlated two-dimensional pancake vortices, which are thermally activated over the surface barrier. Careful analysis of the penetration field data allows measurement of the thermodynamic lower critical field and the vortex line energy.

The sweep rate dependence of the penetration field shows that, for slow sweep rates ($dH_a/dt < 5 \times 10^{-3}$ mT s^{-1} at 68K), the surface barrier collapses to the lower critical field, and this allows a measurement of the penetration depth, which was found to be 182nm at 68K and 209nm at 72K.

When a whisker is aligned with it's small lateral dimension parallel to the length of the Hall sensor array, the vortex profile across the whisker may be measured. The results have shown that as the field is increased from zero, the vortices collect at the centre of the whisker (under the influence of the Lorentz force from the Meissner current) and create a dome-like flux profile, which becomes larger as the field is increased. On the return leg of the hysteresis cycle, the dome begins to flatten out and becomes wider, extending towards the edges of the whisker. At this point, the vortices leave the whisker unhindered, leading to the zero magnetisation observed in hysteresis loops. This agrees well with the model of surface pinning proposed by Clem [1974], and described in chapter 2.

When the whiskers were cooled from above T_C in the presence of a weak magnetic field, abrupt jumps are observed in the local magnetic induction. When plotted in the H-T plane, these jumps map out a transition line which is interpreted as a boundary between a regime dominated by surface barriers and one dominated by the inter-vortex repulsion.

Close inspection of the initial leg of the hysteresis loop often showed fine structure structures, which are interpreted in analogy to a model proposed by Mawatari [1994] for a field applied parallel to a superconducting film. This model proposes a hierarchy of stable states, as the field is increased, with a transition from one stable state to the next indicated by a jump in the local magnetic induction. These jumps are observed in both 2μm and 4μm Hall probes, which shows that the jumps are not simply the result of local vortex motion.

Finally, Ag-epoxy contacts have been made directly onto the whiskers to facilitate transport measurements. Results of experiments to determine the field dependence of the critical current are in agreement with a model by Benkraouda [1998], which assumes no bulk pinning and only surface barrier pinning.

11.3 Further Work

The present work has shown that whiskers are ideal model systems for investigating surface barriers, which are usually dominated by bulk pinning effects. The next step is to combine the transport measurements with magnetic measurements by making electrical contacts to whiskers *in situ* on a Hall bar array. Initial experiments have shown that, apart from the obvious problem of correctly aligning such small specimens, there are problems with the epoxy depleting the 2DEG during annealing. This may be overcome, however, by introducing a thin "buffer layer" between the whisker and the Hall bar, but at the expense of vortex resolution. If this could be done, then many interesting experiments would be possible, since both the sawtooth structure and the dome-profile are strongly current dependent.

Another useful experiment would be to use an imaging technique, such as scanning SQUID microscopy or scanning Hall probe microscopy to try and observe the different vortex states described above directly.

Finally, further irradiation work could prove interesting, since the whiskers do not appear to exhibit the second magnetisation peak effect, commonly associated with vortex line decoupling.

Appendix 1

Iron Clusters

A1.1 Introduction

The small spatial dimensions and excellent field resolution of the Hall probe arrays described in this thesis make them ideal tools for investigating many other types of magnetism, as well as vortices in type II superconductors. In particular, clusters of iron nanoparticles have been deposited onto some arrays in order to see how well magnetism on such a small scale can be quantified with the use of Hall probes.

The magnetic properties of nanoscale ferromagnetic particles have been the subject of much recent research [See for example Chen, 1995, or Cox, 1994] and the interest in these systems is two-fold. Firstly, the typical size of the clusters (1-5nm) places them in an intermediate regime between atomic systems and bulk systems, which means they have distinct, physical properties. For example, the reduced symmetry at the surface leads to a less effective screening of the orbital magnetic moments by the crystal, which increases the surface orbital magnetic moment to up to four times the bulk value [Pastor, 1995].

Secondly, ferromagnetic clusters have great technological potential in the field of storage media, since the nanometre size of the clusters could greatly increase storage capacity. A first step towards this has been made by Melinon [1995], who has achieved a new method of depositing clusters within a matrix.

A1.2 Magnetism in Nanoparticles

In a normal, bulk ferromagnetic material the magnetic free energy of the system is reduced by the formation of magnetic domains, within which all the moments are aligned, making them spontaneously magnetised in one direction (Figure A1.1 (a) and (b) show two examples of possible domain structures).

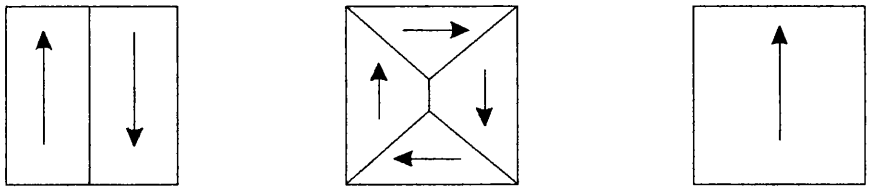

(a) (b) (c)

Figure A1.1. Examples of magnetic domain formation ((a) and (b)) and a single domain particle (c).

The two energy contributions involved in domain formation are the magnetostatic energy and the domain wall energy (the energy associated with the exchange interaction and the anisotropy of the system), and as these compete with one-another, it is clear that at some particle size the energy will be minimised by having just one magnetic domain (Figure A1.1(c)), known as a single domain particle (s.d.p). Consider an Fe sphere of diameter d and saturation magnetisation M_S. Two possible energy configurations are shown in Figure A1.2, with (a) a single domain particle and (b) two domains separated by a domain wall of energy e_w.

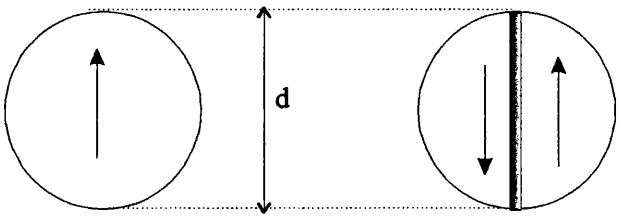

(a) (b)

Figure A1.2. Two possible magnetisation configurations for a sphere.

The free energy of configuration (a) is given by

$$E_a = \frac{1}{2} N_D M_S^2 V = \frac{1}{2} N_D M_S^2 \frac{\pi d^3}{6}, \qquad \text{(A1.1)}$$

where N_D is the demagnetising factor (N_D=1/3 for a sphere) and V is the volume. In case (b), the free energy is given by

$$E_b \approx \frac{E_a}{2} + e_w A = \frac{E_a}{2} + e_w \frac{\pi d^2}{4}, \qquad \text{(A1.2)}$$

where A is the domain wall area. Equating (1.1) and (1.2) gives the critical diameter for single-domain-particle formation, d_c, as

$$d_C = \frac{18 e_w}{\mu_0 M_S^2}. \qquad \text{(A1.3)}$$

Using data for Fe ($\mu_0 M_S^2$=1.75×10^6 J m^{-3} and $e_w \approx 2.0\times10^{-3}$ J m^{-3}), d_c=20nm. Hence particles with sizes smaller than 20nm will be single domain particles, while larger particles will divide into magnetic domains.

The direction of magnetisation within a single domain particle depends on several factors, including the direction of any applied external field (which will tend to align the moments parallel to the field), and the anisotropy of the sample (for example shape anisotropy, where the moments tend to align along a long or "easy" direction, or magnetocrystalline anisotropy, in which the moments align parallel to an "easy" direction in the crystal, which in the case of Fe is the [100] and similar directions). Another factor influencing the direction of the moments in single domain particles is the temperature, since thermal activation may cause M_S to "flip" from one direction to another. In the case of thermal activation, one may expect a minimum temperature below which there is insufficient energy to flip the moments, and this is known as a blocking temperature T_B [Popusoi, 1997].

A1.3 Experimental Details

In order to investigate the magnetic properties of nanoscale particles, clusters (20-200 atoms that coalesce to form a particle typically 5nm in diameter) of Fe have been deposited onto a 1μm Hall bar array. Since this size is less than the critical diameter for domain formation in Fe, the clusters will be single domain particles, and as the clusters are slightly flattened during deposition [Binns, 1999] there will be a small shape anisotropy parallel to the plane of the Hall bar. Previous work on Fe clusters of this size has shown an increase in the orbital magnetic moment to about twice that in bulk Fe, and has determined the saturation magnetisation to be 1T, with the coercive field less than 200mT when a field is applied normal to the surface containing the clusters, and similar results were obtained in a parallel field [Edmonds, 1999]. Also, the blocking temperature in these clusters is thought to be around 10K [Binns, 1999].

A schematic diagram of the Hall bar/Fe cluster heterostructure is shown in Figure A1.3 (a). The clusters were deposited with an average density of 1 cluster / μm^2, which means there will be, on average, one cluster in the active area of a 1μm Hall bar.

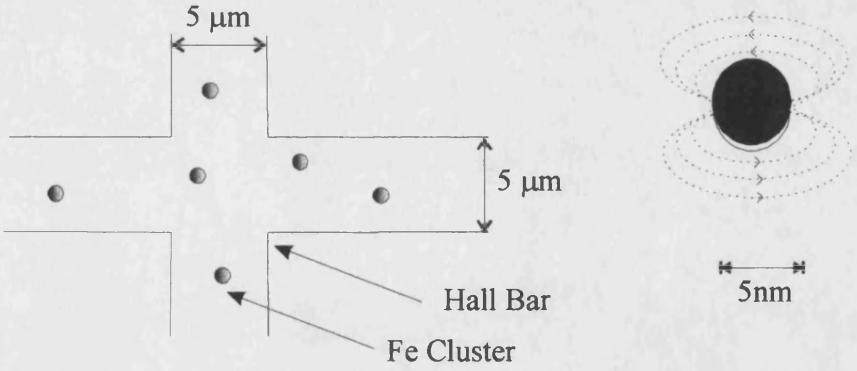

Figure A1.3. The Hall bar/Fe cluster heterostructure (a) and the magnetic field from the cluster (b).

Since the Hall bar only detects the normal component of magnetisation at the edges of the cluster (Figure A1.3(b)), it is important that the cluster is not exactly in

the centre of the Hall bar active area. If it was, there would be no net signal detected, since the contributions from each side of the cluster would cancel (this problem is clearly much worse for larger probes, which is why only 1μm probes were used).

The Hall bar/Fe cluster heterostructure was mounted in the glass cryostat parallel to the axis of the solenoid, so that a magnetic field could be applied parallel to the Hall bar. The system was then cooled, and time-resolved measurements of the magnetic state of the cluster were carried out to look for jumps in the local induction, which are signatures of moment flipping.

A1.4 Time-Resolved Measurements

The results in Figure A1.5 show the time evolution of the local magnetic induction, which is proportional to the mean magnetic moment, in zero applied field for various temperatures ranging from 5.0K to 20.0K. The most striking feature of the data is that they demonstrate the two-level nature of the system, in which the "down" state appears to be more favourable than the "up" state.

Figure A1.4 shows the variation of average jump size with temperature, and the size of the jumps increases with decreasing temperature.

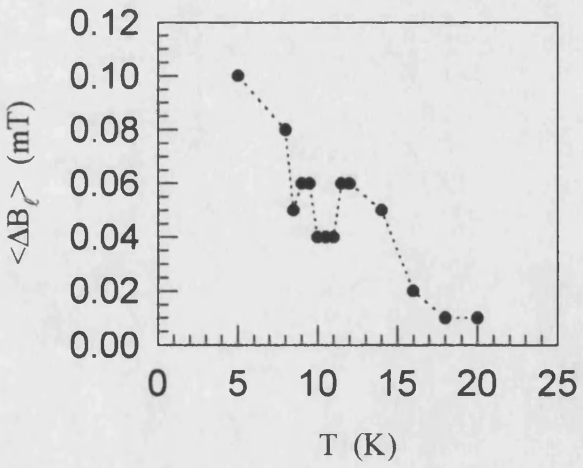

Figure A1.4.Temperature dependence of the average jump size in Fe clusters.

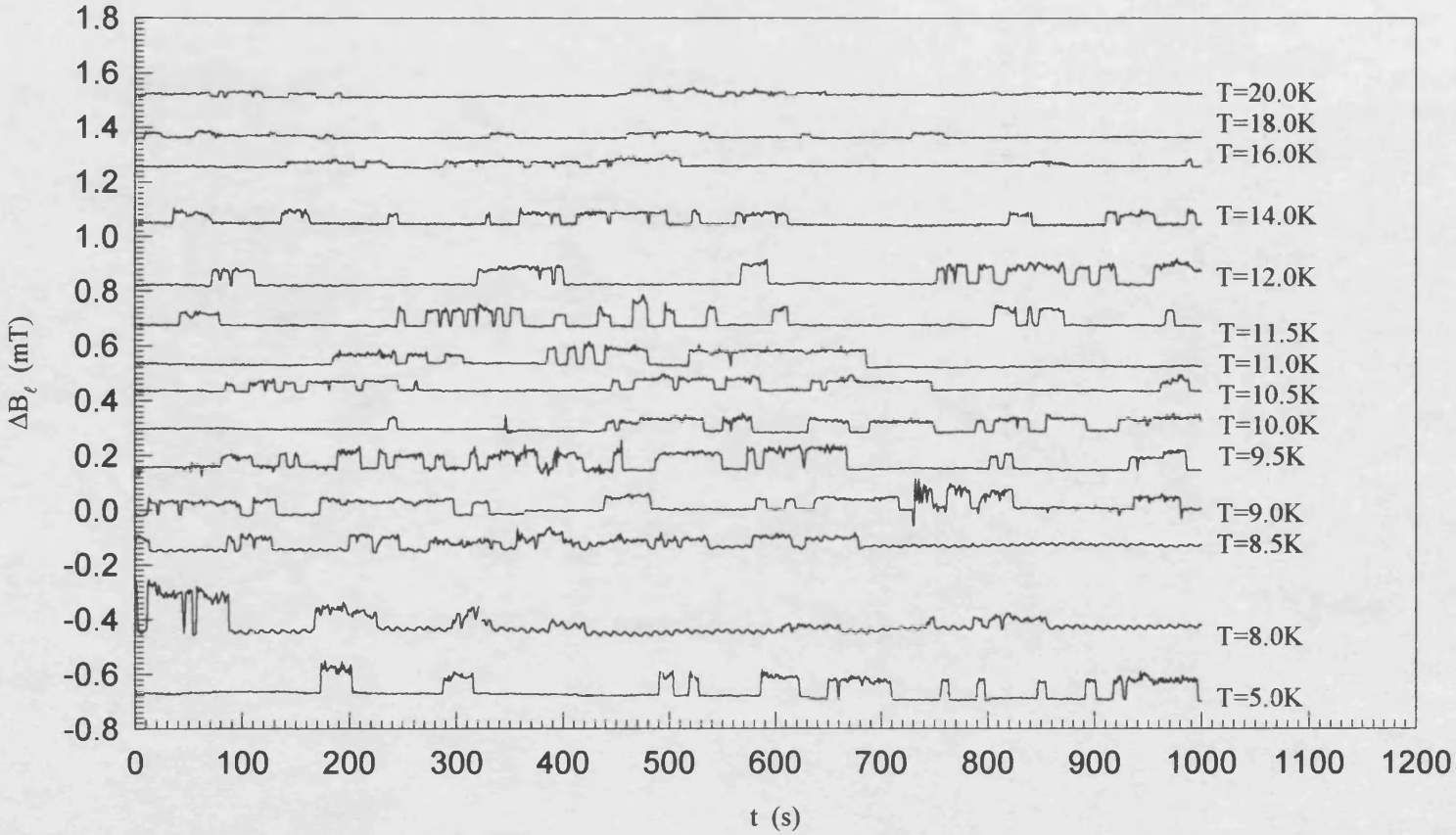

Figure A1.5. Time evolution of the average magnetic moment of Fe clusters (offset), measured for various temperatures in zero applied field.

The lifetimes of the two states are shown in Figure A1.6, and suprisingly there appears to be no correlation between the lifetimes and temperature.

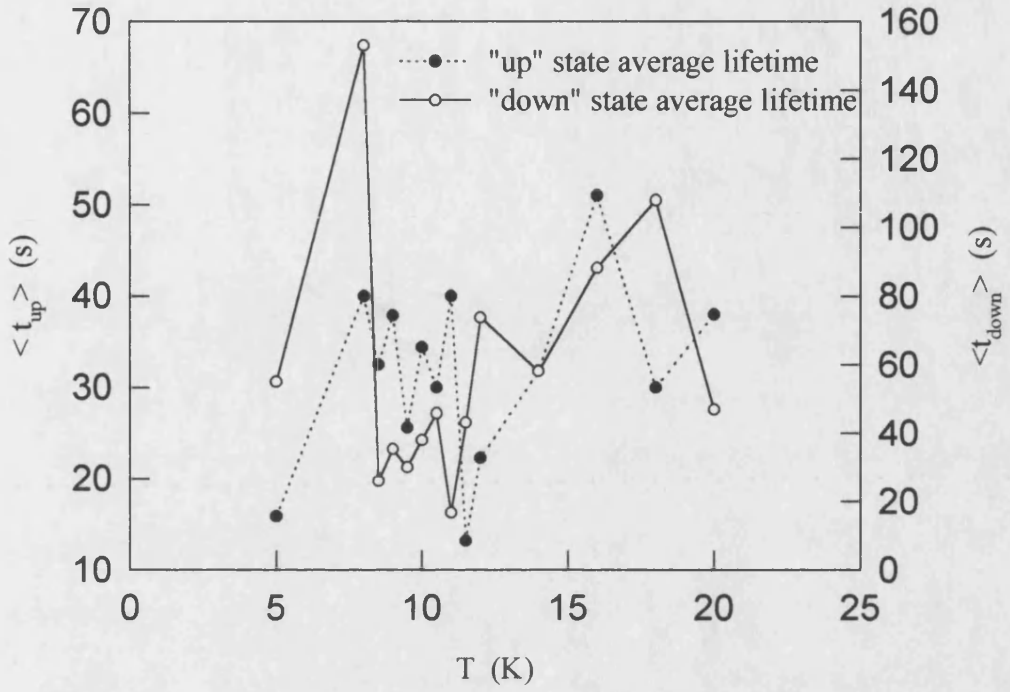

Figure A1.6. Variation in average lifetimes of the up and down states with temperature.

Closer inspection of some of the data from Figure A1.5 shows smaller structure within the jumps, as shown in Figure A1.7, suggesting the Hall bar may be detecting the signals from several clusters.

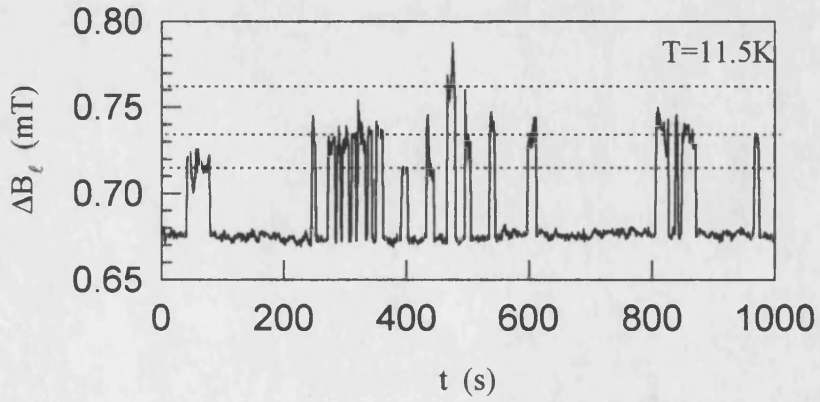

Figure A1.7. The four different states observed in the 11.5K time sweep.

Time sweeps were also carried out with an "in-plane" magnetic field applied. This should suppress the jumps, since an external field will provide a preferred direction for the magnetic moment. Figure A1.8 shows time evolutions measured at 5.0K, with applied fields of 200mT, –200mT and zero, and the jumps are clearly not suppressed; in fact the external field appears to enhance both the frequency and magnitude of the jumps.

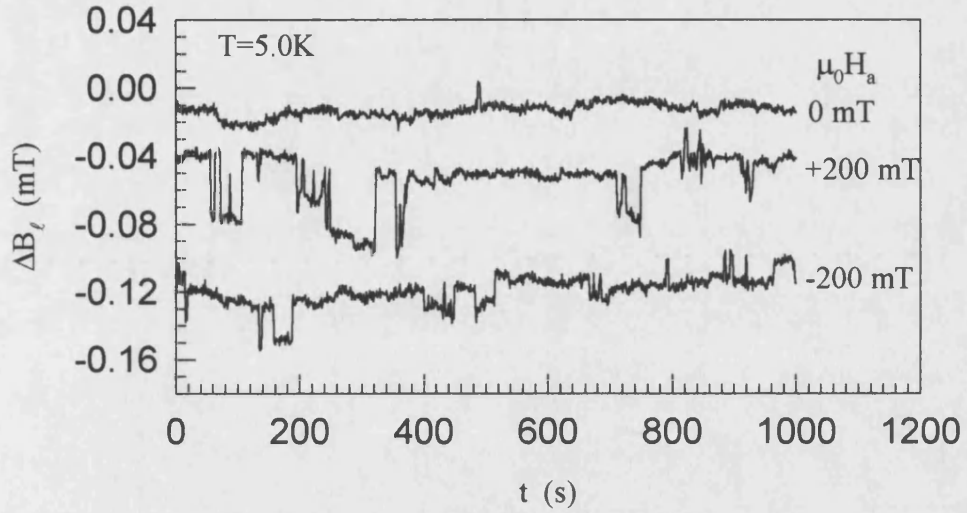

Figure A1.8. Time sweeps measured in the presence of a magnetic field.

One explanation for the apparent lack of suppression of switching may be that the applied field was smaller than the coercive field of the clusters, but this has been reported to be smaller than 100mT [Edmonds, 1999] so this does not appear to be a valid explanation.

These data, combined with the lack of any evidence of a blocking temperature and the complicated temperature dependence of the lifetimes, suggests that the system is more complicated than the simple picture of moment flipping by thermal activation presented above. There are several possible explanations for this, which can be grouped into two categories: (i) magnetic and thermal cycling history, and (ii) cluster interactions with the 2DEG Hall sensor. It has been shown [Papusoi, 1997] that the blocking temperature is dependent on the cooling rate, and since the clusters were taken through many cooling cycles during measurement, it is possible that the blocking temperature has been reduced to much lower temperatures. Another

possibility is that the observed jumps are independent of the clusters, and originate from random telegraph noise produced by electron traps inside the 2DEG Hall Sensor. This seems unlikely, however, since telegraph noise is usually frozen out at the low temperatures used in this work, and they exhibit a strong (exponential) temperature dependence not observed here. The final possibility is that the clusters are charging up as the electrons tunnel between them, effectively gating the Hall bar, but this seems to be a very unlikely process due to the large tunnelling distances involved.

A1.5 Hysteresis Loops

Figure A1.9 shows a full hysteresis loop measured with the external field applied parallel to the Hall bar, so that only the perpendicular component of the magnetisation is measured.

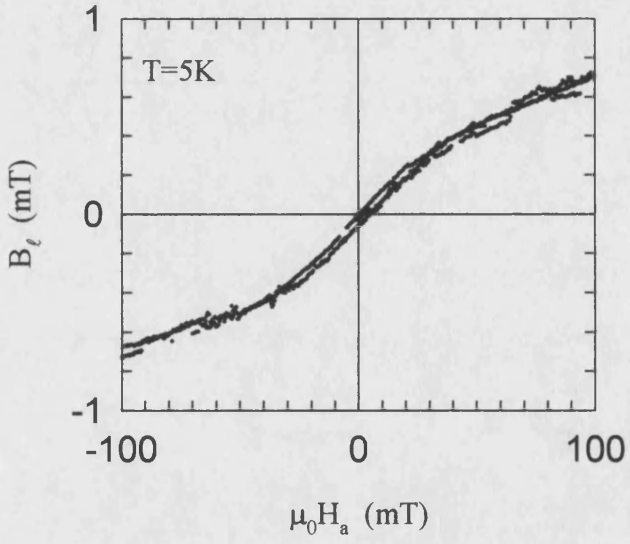

Figure A1.9. Hysteresis loop measured on an Fe cluster at 5K.

The cluster magnetisation is clearly hysteretic and, since the clusters are single domain particles, the source of the hysteresis cannot be domain wall motion. Therefore the hysteresis must be a result of moment rotation, which is the other major source of hysteresis in ferromagnetic materials. The general S-shape of the hysteresis

loop is in general agreement with results from X-Ray Magnetic Circular Dichroism (XMCD) experiments, [Binns, 1999] which were carried out on similar clusters.

Closer inspection of the initial leg of the hysteresis loop, shown in Figure A1.10, reveals jumps in the local induction, which are the same jumps as those observed in the time sweeps described in the previous section.

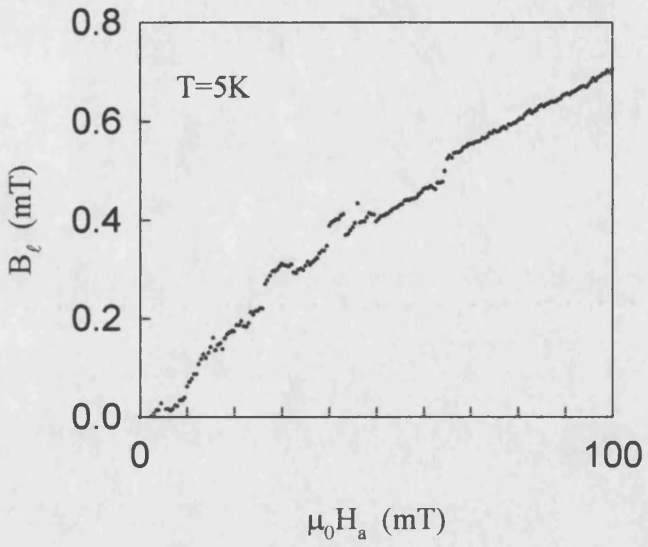

Figure A1.10. Jumps in the initial leg of the hysteresis loop.

The jumps do not appear to change in either magnitude or frequency as the field is increased, even at high fields, which would be expected to provide a preferred direction to suppress the jumps.

This is only a preliminary study of this system and much more work needs to be done to clarify what is going on.

Appendix 2

Publications

A2.1 Published Work

The work presented in this thesis has led to the following publications.

Field Penetration and Surface Barriers in Superconducting $Bi_2Sr_2CaCu_2O_{8+\delta}$ Whiskers, M. S. James, S. T. Stoddart, S. J. Bending, S. Aukkaravittayapun, P. J. King and M. Henini, Phys. Rev. B **56**, R5771 (1997).

Influence of Surface Barriers on Vortex Dynamics in $Bi_2Sr_2CaCu_2O_{8+\delta}$ Whiskers, M. S. James, S. J. Bending, S. T. Stoddart, S. Aukkaravittayapun, P. J. King and M. Henini, IEEE Trans. App. Supercond. **9**, 2671 (1999)

References

A. A. Abrikosov, JETP **5**, 1174 (1957)

C. M. Aergeter *et al.*, Phys. Rev. B **54,** R15661 (1996)

P. W. Anderson, Phys. Rev. Lett. **9,** 309 (1962)

S. Aukkaravittayapun *et al.*, Physica C **270,** 231 (1996)

J. Bardeen *et al.*, Phys. Rev. A **140,** 1197 (1965)

C. P. Bean, Phys. Rev. Lett. **8,** 250 (1962)

C. P. Bean and J. D. Livingston, Phys. Rev. Lett. **12,** 14 (1964)

J. G. Bednorz and K. A. Müller, Z Phys **64,** 189 (1986)

S. J. Bending *et al.*, Phys. Rev. Lett **80,** 3610 (1998)

M. Benkraouda and J. R. Clem Phys. Rev. B **58,** 15103 (1998)

C. Binns, Private Communication, (1999)

D. J. Bishop *et al.*, Science **255**, 165 (1992)

T. Blasius *et al.*, Phys. Rev. Lett. **82,** 4926 (1999)

G. Blatter *et al.*, Rev. Mod. Phys. **66,** 1125 (1994)

G. Blatter *et al.*, Phys. Rev. B **54,** 72 (`996)

L. Börnstein, *Numerical Data and Functional Relationships in Science and Technology New Series*, Vol III/179 *Physics of Group IV elements and III-V Compounds*, O. Madelung (ed), (Berlin, Springer-Verlag) (1982)

E. H. Brandt *et al.*, Europhys. Lett. **22,** 735(1993)

E. H. Brandt, Rep. Prog. Phys. **58,** 1465 (1995)

L. Burlachkov, Phys. Rev. B **47,** 8056 (1993)

L. Burlachkov *et al.*, Phys. Rev. B **50,** 16770 (1994)

C. C. Chang and A. C. Rose-Innes, Proc. 10th Int. Conf. on Low Temp. Phys. **LT12,** 381 (1971)

J. P. Chen *et al.*, Phys. Rev. B **51,** 11527 (1995)

X-F Chen *et al.*, Phys. Rev. B **48,** 1254 (1993)

L. Civale *et al.*, Phys. Rev. Lett. **67,** 648 (1991)

J. Clark, *Superconducting Devices*, ed S. T. Ruggerio and D. A. Rudman, (San Diego, Academic) (1990)

J. R. Clem, Proc. 13th Conf. on Low Temp. Phys. **3,** 102 (1974)

L. F. Cohen *et al.*, Supercond. Sci. and Tech. **10,** 195 (1997)

A. J. Cox *et al.*, Phys. Rev. B **49,** 12295 (1994)

R. Cubitt *et al.*, Nature **365,** 407 (1993)

K. W. Edmonds *et al.*, Phys. Rev. B **60,** 472 (1999)

J. D. Eshelby, Phys. Rev. **91,** 755 (1953)

D. T. Fuchs *et al.*, Phys. Rev. Lett. **80,** 4971 (1998)

J. Gallop, *SQUIDS, Josephson Effects and Superconducting Electronics*, (Bristol, Hilger) 1991

P. L. Gammel *et al.*, Phys. Rev. Lett. **61,** 1666 (1988)

J. R. Gavalar, App. Phys. Lett. **23,** 480 (1973)

V. L. Ginzburg and L. D. Landau, JETP **20**, 1064 (1950)

R. C. Harsen, IEEE Trans. Aero. Elec. Sys. **26**, 345 (1990)

R. Hazen *et al.*, Phys. Rev. Lett. **60,** 1174 (1988)

R. P. Huebener, *Magnetic Flux Structures in Superconductors*, (Berlin, Springer-Verlag), 1979

T. Jacobs *et al.*, Phys. Rev. Lett. **75,** 4516 (1995)

H. Jin and Q. M. Liu, Jn. Cryst. Growth **181,** 446 (1997)

C. D. Keener *et al.*, Phys. Rev. Lett. **78,** 1118 (1997)

B. Khaykovich *et al.*, Phys. Rev. Lett. **76,** 2555 (1996)

B. Khaykovich *et al.*, Phys. Rev. B **56,** R517 (1997)

Y. P. Kim *et al.*, Phys. Rev. **131,** 2486 (1963)

M. Konczykowski *et al.*, Phys. Rev. B **43,** 13707 (1991)

W. Kraak *et al.*, Phys. Stat. Sol. A **158,** 183 (1996)

A. V. Kuznetsov *et al.*, Phys. Rev. B **56,** 9064 (1997)

Y. Latyshev *et al.*, Physica C **16,** 47 (1993)

S. L. Lee *et al.*, Phys. Rev. Lett. **75,** 922 (1995)

T. W. Li *et al.*, Jn. Crystal Growth, **135,** 481 (1994)

T. W. Li *et al.*, Physica C, **224,** 110 (1994b)

W. T. Lin *et al.*, Solid State Elec. **33,** 1455 (1990)

F. London and H. London, Proc. Roy. Soc. (London) **A149**, 71 (1935)

G. C. Long *et al.*, IEEE Trans. on App. Sup. **3**, 3037 (1993)

H. Maeda *et al.*, Jpn. J. App. Phys. **27,** L209 (1988)

D. Majer *et al.*, Phys. Lett. **75,** 1166 (1995)

N. Matahira *et al.*, Jn. Ceramic Soc. Jpn. **97,** 1009 (1989)

I. Matsubara *et al.*, Jn. Cryst. Growth **167,** 570 (1996)

Y. Mawatari and K. Yamafuji, Physc. C **228,** 336 (1994)

W. Meissner and R. Ochsenfeld, Naturwissenschaften **21,** 787 (1933)

P. Melinon *et al.*, Int. Jn. Mod. Phys. B **9,** 339 (1995)

M Nideröst *et al.*, Phys. Rev. Lett. **81,** 3231 (1998)

H. K. Onnes, Leiden Comm., **120b,** (1911)

J. A. Osborn, Phys. Rev. **67,** 351 (1945)

C. Papusoi *et al.*, Jn. Mag. and Mag. Mat. **174,** 236 (1997)

G. M. Pastor *et al.*, Phys. Rev. Lett. **75,** 326 (1995)

H. Pastoriza *et al.*, Phys. Rev. Lett. **72,** 2951 (1994)

D. D. Rashon, Rev. Sci. Instrum. **33,** 201 (1962)

P. L. Richards and Q. Hu, Proc. IEEE **77,** 1233 (1989)

S. Ryu *et al.*, Phys. Rev. Lett. **77,** 2300 (1996)

E. W. Saker *et al.*, Brit. Jn. of App. Phys. **6,** 217 (1955)

Z. Z. Scheng and A. M. Hermann, Nature **232,** 55 (1988)

A Schilling *et al.*, Nature **382,** 791 (1996)

S. T. Stoddart, Ph.D Thesis, University of Bath (1994)

S. T.Stoddart *et al.*, Supercond. Sci. and Tech. **8,** 459 (1995)

M. Tinkham, *Introduction to Superconductivity,* (New York, McGRaw Hill) (1975)

R. S. Wagner and W. C. Ellis, App. Phys. Lett. **4,** 89 (1964)

J. R. Waldram, *Superconductivity of Metals and Cuprates,* (Bristol, Institute of Physics) (1996)

M. K. Wu *et al.*, Phys. Rev. Lett. **58,** 908 (1987)

G. Yang *et al.*, Phys. Rev. B **48,** 4054 (1993)

M. Zeise *et al.*, Phys. Rev. B **53,** 8658 (1996)

E. Zeldov *et al.*, Phys. Rev. B **49,** 9802 (1994)

E. Zeldov *et al.*, Phys. Rev. Lett. **73,** 1428 (1994b)

E. Zeldov *et al.*, Nature **375**, 373 (1995)